Enhancement of Seismic Performance of Reinforced Concrete Beams with Non-structural Walls

(壁付鉄筋コンクリート部材の耐震性能の高度化に関する研究)

2020.09

Walid Ahmad Safi

Acknowledgment

This research was possible through the financial support provided by the Ministry of Education, Culture, Sports, Science and Technology (MEXT) of Japan. The opinions expressed in this dissertation are those of the writer and do not necessarily reflect the views of the sponsors.

The writer greatly appreciates to have been advised both academically and personally by Associate Professors Yo Hibino and Hiroyuki Miura. Their invaluable and continuous support fulfilled the writer's Ph.D. learning process and was instrumental in the completion of this dissertation.

The writer is also grateful for having the opportunity to be advised and taught by Professors Taiki Saito and Yasushi Sanda. Their research enthusiasm and deep knowledge will definitely inspire and benefit the writer in his professional career.

The author wishes to thank his fellow students at the Hiroshima University, in particular, Yusaku Ono, Yugo Mori, Keisuke Murata, Shunsuke Inoue, Hiroki Tanaka, Naoya Komoto, Ryuta Fujiwara, Yuka Hirakawa, An Jihyeon for their kind help during experimental tests.

Many special thanks to Shamsul Hadi Shams and his wife Nozomi Yamamoto Shams for their tremendous help in the English revision of part of this desertion and being very supportive friends along the way in completing my doctoral degree program. Sincere thanks are also due to the Hiroshima University Structures Laboratory staff, Engineer Shotaro Hiramatsu and other Engineers for their invaluable help during the experimental phase of this research. Finally, the writer wishes to thank his beloved family, especially his parents and his wife Ms. Homaira Safi whose endless love, support and encouragement were always with him.

Table of Contents

List of figures

List of Tables

List of Equation

Summary of dissertation

The researches in this dissertation are aimed to experimentally observe methods utilizing potential capability of the non-structural walls for enhancement of the seismic capability of buildings. Particularly, for capability enhancement of the post-disaster management buildings which are expected to remain functional after large possible earthquake.

In order to achieve the research objectives, the following tasks were performed:

Chapter I: Japanese building design review

The review of Japanese building design covered three basic topics. The first topic focused on the seismic design criteria of reinforced concrete building provided by Architecture Institute of japan (AIJ). Particularly, capacity design method for mid to high-rise building was reviewed and approaches for simply implementation of the method were suggested. The second topic focused on review of the possible future earthquakes which is predicted to be happened in the future with high intensity. The third topic focused on the review of design criteria of post-disaster management building provided by National Institute for Land and Infrastructure Management (NILIM). The review was followed by design method and literature review of typical non-structural reinforced concrete walls.

Chapter II: First experimental studies

The first experimental program included static and dynamic tests. The specimens which were comprised from a beam with spandrels (hanging and standing wall) were tested under static cyclic loading test. The dynamic experimental test was a proceeding of the cyclic loading test which was aimed to ascertain the effectiveness of the proposed method of detailing of the non-structural wall used in the static cyclic loading test. In the dynamic test, a full scale three story building was to be tested on the world's largest shaking table of E-defense under artificial earthquakes.

Chapter III: Shear strength prediction of beam members using experimental data

The data obtained from first experimental test and a data from a former experimental test was evaluated in order to observe methods of prediction of shear strength capacity of beam member with spandrels. The analytical evaluation of the experimental data resulted in an accurate equation for prediction of shear strength of a member with spandrel (with hanging and standing walls) and also addressed correlation between shear and normal strength of beams, considering Mohr-coulomb criteria for prediction of shear strength of concrete.

Chapter IV: Second experimental study

The second experimental program which was continuity of the first experimental test, had six specimens and tested under cyclic loading method. Each specimen comprised from a beam and hanging wall without seismic slit. The experimental test observed the impact of transverse reinforcement, the anchored and non-anchored detailing of longitudinal reinforcement; impact of boundary confinement on the longitudinal bars considering different detailing; and slenderness impact on the performance of hanging wall.

Chapter V: Evaluation of analytical model with experimental data

The data of second experimental test was analytically evaluated to verify the impact of confinements on the concrete considering better workability of non-anchored reinforcement and confinement along with concrete. The evaluation results ascertained accuracy of the existed analytical models for evaluation of the beam members. For evaluation of the experimental data the (Hognested, et al.,1951; and Mander, et al., 1984) models was used.

Chapter VI: Conclusions and summary

The final task consisted of a summary of the main aspects of the research program and conclusions drawn from the experimental and analytical studies.

Major findings

From the experiments and analysis conducted in this research, the following conclusions can be drawn:

1) Seismic capability of the beam members can be improved utilizing potential capability of the non-structural walls. A method of non-structural wall connection with moment resisting frame was suggested that provides a mechanism helping appropriate involvement of the non-structural wall in load carrying scenario and keeping functionality of building after disaster.
2) The analytical evaluation of the experimental data provided to propose a simple equation for shear strength prediction of a beam having monolithic spandrels. The proposed Equation can predict shear strength capacity of the component with significant accuracy.
3) A method of reinforcement detailing of the typical non-structure wall that confers higher capability to the wall and increase the possibility of continuous use of buildings, was suggested. The method suggests construction of the beam members without seismic slit and non-anchorage of the longitudinal bars along with placement of boundary confinement.

Glossary

Anchored reinforcement Anchored reinforcement: The anchored reinforcement refers to those reinforcement detailing in which the longitudinal reinforcements of a wall segment are extended to adjacent member.

Design drift limit The design drift limit considers uncertainty of earthquake loads and variation of building characteristics such as material strengths. The design drift limit is the structural drift at which total energy dissipation of the building under static lateral load is more than twice of that at the response drift limit.

Global yielding mechanism Global yielding mechanism: The global yielding mechanism refers to the stat of the building in which deformation occurs in all over the structure rather than concentration in a particular story such as weak-beam strong-column mechanism.

Hinge member Hinge member: The member designed to have yield hinges.

Non-anchored reinforcement Non-anchored reinforcement: The non-anchored reinforcement refers to those reinforcement detailing in which the longitudinal reinforcements of a wall segment are not extended to adjacent member.

Non-hinge member Non-hinge member: The member designed to have no yield hinges.

Non-structure wall Non-structure wall: The non-structure wall refers to a reinforced concrete wall, attached to the moment resisting frame by one side; and isolated from moment resisting frame by adding seismic slit in three sides of the wall.

Partial yielding mechanism Partial yielding mechanism: The partial yielding mechanism refers to the stat of building in which deformation is

	concentrated in a particular story such as strong-beam weak-column mechanism.
Reliable strength	The reliable strength is the lower bound of the member strength, considering the uncertainty of material strengths and accuracy of design formula. Reliable flexure strength for beam and column are 0.97 and 1.01 times of the nominal flexure strength respectively.
Response drift limit	The response drift limit is defined in terms of structural drift, and is intended to control the deformation under the possible strongest intensity earthquake motions. The response drift limit should not exceed 1/120 under earthquake level 2.
Seismic slit	The seismic slit is a gap between non-structure wall and moment resisting frame which isolates the non-structure wall.
Serviceability drift limit	The serviceability drift limit is defined in terms of story drift, and is used to control structural and nonstructural damage. The serviceability drift limit should not exceed 1/200 under earthquake level 1, without any destruction to the structural and nonstructural elements.
Upper strength	It refers to the upper bound strength of a member in which the uncertainty of material strength and design formula is not considered. The upper flexure strength for beam and column are 1.11 and 1.49 times of the nominal flexure strength respectively.
Yield mechanism	Yield mechanism: The yield mechanism refers to the stat of members in which yield hinges are formulated and the lateral load capacity of the member does not increase with the increase of seismic load.

Chapter I

Background and Seismic Design Criteria for Building

1.1 Introduction

Damage observation of the reinforced concrete building after Great Hanshin earthquake of Japan in 1995 declared that the typical damage to buildings was due to collapse of soft first stories; column failure due to torsional response; inadequate spacing and anchorage of transverse reinforcement; and damage to non-structural members (Watanabe, 1997). However, overall damage observation of the buildings which were built after amendment of Japanese building standard in the 1981, shows that their structural members experienced minor damage but non-structural walls were reportedly significantly damaged (AIJ, 1995).

Conversely it was observed that although columns and walls of large-scale buildings failed in shear during the Great Tohoku earthquake in 2011 but majority of the reinforced concrete buildings remained uncollapsed. The safety of structural members was designed to be higher during the Great Tohoku earthquake which triggered buildings not to collapse as it happened during Great Hanshin Earthquake. However, severe damage was found in the non-structural walls which tends adversely affect the structural performance of frame and decreased the possibility of continues use of buildings after seismic event (Maeda, et al. 2012). Several new buildings designed by a current Japanese building code also suffered shear failure of non-structural panels surrounding entrance or window openings (BRI and NILIM, 2011).

The idea of containing damage of non-structural walls through avoiding stress transmission, has been encouraged after Great Hanshin earthquake in Japan. Accordingly, the stress transmission and relatively damage to the non-structural wall, is avoided with installation of seismic slit between the wall and moment resisting frame. However, in practice, the seismic slit is often appeared as result of monolithic casting of the non-structural wall with a frame, and does not completely isolate non-structural wall.

In addition, the seismic slit not only complicates designing of a building with an earthquake-resistant wall but also results in a reduction of the strength in a frame and rigidity in a building. Considering the significance of the strength and rigidity of a building, the existence of seismic slit might be inefficient in many cases of low-rise buildings, which could have been oriented to strength-based design (Kabeyasawa, et al., 2014).

Under the current design practices in Japan, reinforced concrete non-structural walls are often isolated from the moment-resisting frames by a seismic slit installed between the wall segment and primary frame. In certain cases, presence of the seismic slit induces the beam to fail against shear rather than formation of plastic. Therefore, the observation of shear failure of beam and beam member requires more detail investigation.

The researches in this dissertation are aimed to experimentally observe methods utilizing potential capability of the non-structural walls for enhancement of the seismic capability of building. Particularly, for capability enhancement of the post-disaster management buildings which are expected to remain functional after large possible large earthquakes like Tokai (Shizuoka Prefecture, 2010) and Nankai (Mochizuki, et al., 2003). The outcome of these research provides effective non-structural wall connection method, reinforcement detailing, and influential placement of the transverse reinforcements. In addition, to propose an accurate Equation for prediction of shear strength of a member with spandrel (with hanging and standing walls) and address correlation between shear and normal strength of beam and column, considering recently developed methods of shear strength prediction like Mohr-coulomb. The observed indications of the researches can be further developed for the structural shear walls focusing on the proposed method of wall connection and effective placement of the transverse reinforcement.

1.2 Seismic Design Considerations

1.2.1 Seismic Resistance System

Seismic design of reinforced concrete building against earthquake has priority over other structural design considerations. Seismic design was first included in building standards in Japan in 1924, after the Great Kanto Earthquake of 1923. Since then, building standards have been revised after every major earthquake. The latest major revision of building standards took place in 1981 and incorporated a new seismic design method. Accordingly, buildings that are built after 1981 are deemed earthquake-resistant, but those built before 1981 need to be evaluated for their seismic capacity based on the 1981 standards. Even with the new seismic design standards, however, it is not possible to completely prevent damaging buildings from severe earthquakes (Otani, 2004).

It is necessary to absorb earthquake energy through the inelastic deformation, or in other works, through the ductility, of the structure. The damaged elements in a seismic resisting system dissipate large amount of energy and sometime may cause the total collapse of building if cannot afford sufficient energy dissipation ability (Chang, et al., 2008). Given this point, beam-hinge mechanism, or strong column-weak beam mechanism, shown Figure 1.2.1, is always assumed. Column hinges are also allowed at the bottom of the first story and the top of the uppermost story,

and at the exterior column in the tension side of the lower stories. The hinges in beams dissipate larger amount of energy and strong columns proved the building not to collapse.

It has to be noticed that the rigidity distribution in every story of an irregular building varies therefore, sometimes the hinges does not appear to be at same location as stated by the strong-column mechanism. In such cases, the locations of plastic hinge formation are influenced by the eccentricity rate. The column hinges at rigid side decreases as eccentric ratio increases, however; different eccentricity ratio does not produce significant pattern change for column hinges in flexible side (Han, et al., 2008).

The beam hinge mechanism is assumed in order to provide large energy dissipating capacity distributed all around the structure. However, it is not desirable if the above mention collapse mechanism is altered by the presence of non-structural elements (Aoyama, 2010, pp. 22-25). Particularly for the building aiming to be used as a post-disaster management facility with the expectation of utilizing non-structural wall potential capacity for continues functionality.

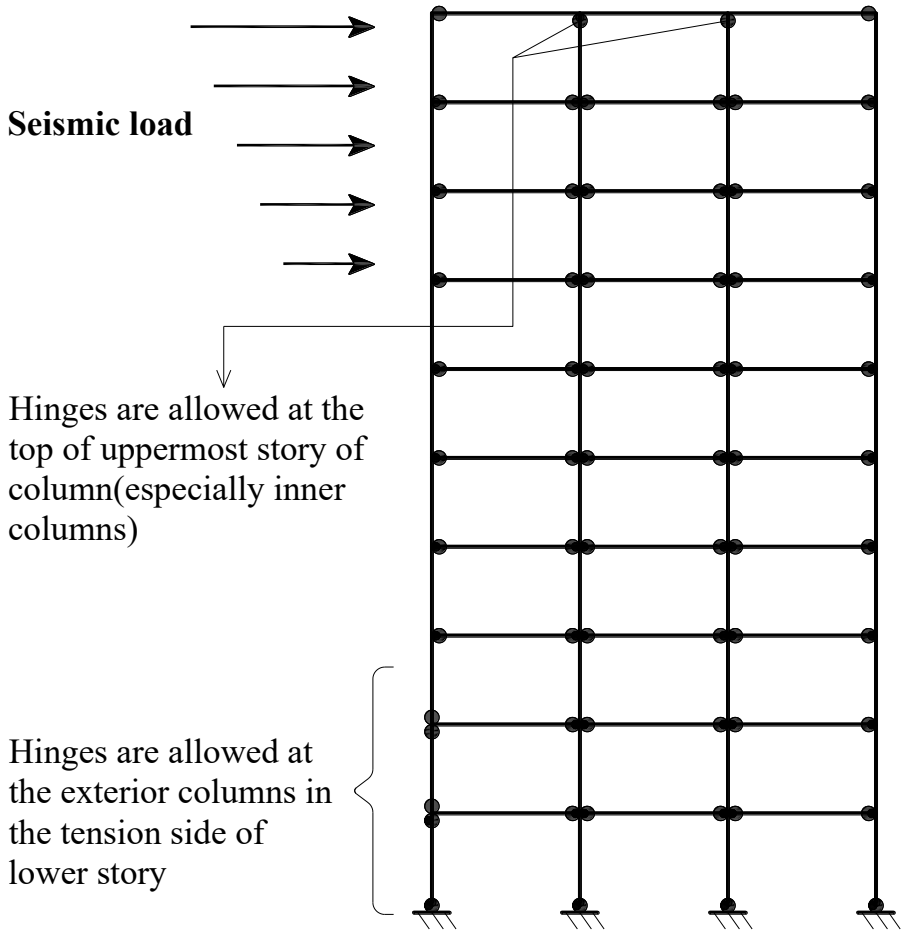

Figure 1.2.1 Strong column-weak beam mechanism

A method of non-structural wall placement that maintain the desired collapse mechanism is not specified in the standard. However, for the sake of simplification of the design, it is suggested not to consider the contribution of these non-structural components during seismic design. For this reason, all non-structural elements are insulated from the structural members using seismic slit. For example, concrete walls cast monolithically with frames are completely avoided except for those in the basement and designated shear walls in the superstructure.

Consequently, according to the mechanism almost all girders are assumed to have yield hinges at both ends. therefore, shear strength of the girders must be sufficient to prevent premature shear failure. One of the methods to evaluate the shear strength is the empirical Equation (1.2.1) which was proposed by Ohno and Arakawa (Ohno, et al., 1960).

$$Q_A = b\, j\, \{\alpha\, f_s + 0.5\ {}_w f_t\, (p_w - 0.002)\} \tag{1.2.1}$$

$$\alpha = f_c \frac{4}{\frac{M}{Qd} + 1} \quad 1 \le \alpha \le 2 \tag{1.2.2}$$

Where

b: is the widths of beam or web width for a T-shaped beam.

j: is the distance between compressive and tensile resultants, and may be assumed to be (7/8)d.

d: is the effective depth of beam.

p_w: is the transverse shear reinforcement ratio $= \frac{a_w}{b\, x}$

a_w: is the sectional area of a set of transverse shear reinforcement.

x: is the spacing of transverse shear reinforcement.

f_s : is the allowable tensile stress of transverse shear reinforcement.

${}_w f_t$: is the allowable tensile stress of transverse shear reinforcement.

α: is the coefficient as function of shear span ratio $\frac{M}{Qd}$

M: is the maximum design bending moment in the beam.

Q: is the maximum design shear force in the beam.

If value of p_w in the Equation (1.2.1) is greater than 1.2 percent, allowable shear force shall be calculated with p_w equal to 1.2 percent.

1.2.2 Design criteria for Earthquake Load

A guideline of Japan Concrete institute (JCI, 2005) proposes seismic safety investigation by means of dynamic and static analyses in three stages, namely, levels 1 and 2, and post-level 2. For level 1 earthquake motion which would happen once in the lifetime of the building, serviceability should be maintained. For level 2 earthquake motion which may be the possible maximum motion

to the structure, safety against collapse should be maintained as explained in Table 1.2.1. For the post-level 2 stage, the structure should still maintain suitable collapse mechanism and lateral load-carrying capacity as explained in Table 1.2.2.

Table 1.2.1 Lateral displacement and building status criteria.

Level of design earthquake	[1]Lateral deformation	Maximum ground velocity (cm/sec2)	Story ductility factor	Member ductility factor (μ)	Status of building	Status of element
Level 1	δ1 < 1/200	25	<1	<1	-	Before yielding
Level 2	δ2 <1/120, and <1.5δ1	50	<2	<2	No degradation of lateral resistance	Yielding is allowed

[1]δ1 is story drift and δ2 is structure drift at the center of lateral load

Table 1.2.2 Design criteria at frame design drift limit.

Performance of element		Lateral resistance of frame
Hinge member	Designed such to be ductile	Base shear coefficient >0.25R_tZ
Non-hinge member	Designed to have enough strength to avoid yielding	

Z is the seismic zone factor
R_t is the vibration characteristic factor

Generally, earthquake design criteria for a structure is expressed as the combination of design earthquake intensity and design drift limitation. Accordingly, the building structure should remain elastic and satisfy the serviceability criteria under level 1 earthquake. The serviceability criteria are: (1) story drift in any story should be less than the serviceability drift limit, (2) no structural members should, in principle, develop yielding, and (3) non-structural elements should not be damaged.

A structure must also satisfy safety performance criteria for level 2 earthquake motions. Safety criteria are examined by the nonlinear earthquake response analysis. The structure is assumed to experience nonlinear behavior associated with yielding of re-bars under the action of level 2

earthquake motion, but to remain in the range of stable deformation without load-carrying capacity drop.

To achieve this end, the safety criteria for the response analysis are set forth as follows: (1) maximum structural drift should be less than the response drift limit, (2) maximum story drift in any story should be less than 1.5 times the above limit. As to the state of the members (3) yielding is permitted but no resistance reduction is allowed. But in reality, the force and deformation of each member at this stage is not examined, because it is inferred that the check for the post level 2 stage would automatically cover the safety criteria for the members. For the level 2 and post-level 2 stages, safety performance is examined also by static (pushover) analysis.

The design drift limit is defined as a structure drift at which the work (energy dissipation) done by static loads becomes two times of that at the response drift limit. On the other hand, the area dominated under the capacity curve as shown in Figure 1.2.2 until response drift limit along *x* axis should be equal to the area from response drift limit until design drift limit. In short, the design drift limit is obtained using the area dominated under the capacity curve of the building.

The area until response drift limit A_1 is simply obtained by integrating the divided trapezoidal fibers Δa_i from zero to δ_i under the capacity curve. The area from response drift limit until design drift limit A_2 is obtained using the A_1. For this purpose, integrating of the divided fibers under the curve is continued until from zero until the resulted area reaches two times of A_1. The fiber makes the total area twice of the A_1 is intended to be the design drift limit. Energy dissipation of a building until response drift limit is simply obtained using following equations:

$$A_1 = \sum_{i=1}^{n} \Delta A_i \tag{1.2.1}$$

$$\Delta A_i = \frac{1}{2}\left(Q_{j+1} + Q_j\right)\Delta a_i \tag{1.2.2}$$

$$\Delta a_i = \delta_{i+1} - \delta_i \tag{1.2.3}$$

Where

A_1 : is the energy dissipation until response drift limit.

ΔA_i : is the area or energy dissipation of the building corresponding to a small Δa_i increments.

Q_j : is the shear force *j* complying to the drift δ_i .

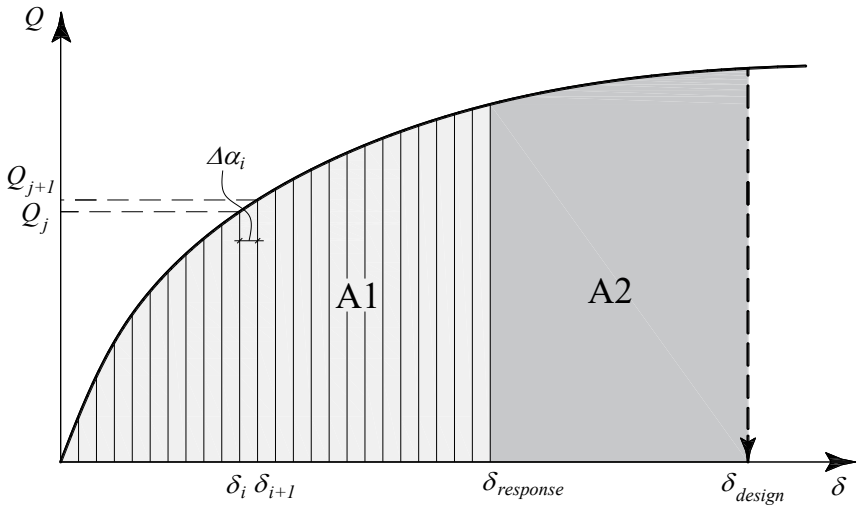

Figure 1.2.2 Analytical model for energy dissipation and design drift limit

An easy way to explain procedure of signifying the design drift limit of a building is a flow chart as shown in Figure 1.2.3. The following input data is required to proceed the analysis of signifying the design drift limit using the flow chart.

n : is the total number of divisor of dominated area under the capacity to identify the length of drift increments ΔA_i.

δ_i: is the drift corresponding to the lateral load Q_j

$Q = f(\delta)$: is the load-deflection curve of the structure.

By push-over analysis until frame design drift, local yielding mechanism should be avoided and hinge members should not be destroyed by shear, bonding and compression of concrete. Likewise, if the design drift is over than 1/80 and natural period of building is more than 4 second, P-Δ effect should be considered.

P-Delta effect typically involves large external forces upon relatively small displacements. If deformations become sufficiently large as to break from linear compatibility relationships, then Large-Displacement and or Large-Deformation analyses may become necessary.

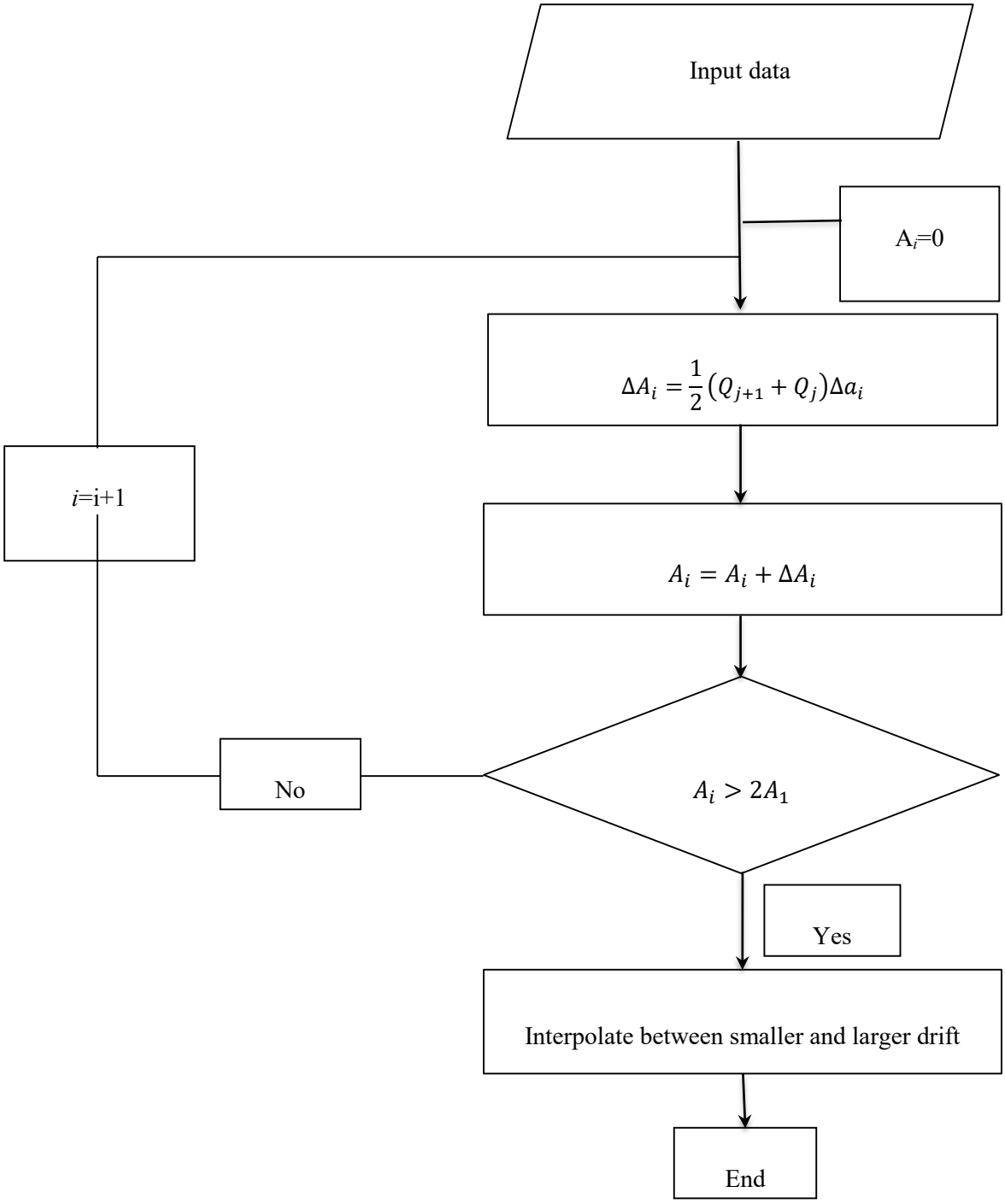

Figure 1.2.3 A Flow chart that explaining analysis of the energy dissipation of a building using capacity curve.

Table 1.2.3 Typical design procedure's summery

Design criteria	**Considerations**
Criteria for dynamic design.	4 input earthquake ground motions (3 historical earthquake records and one artificial record) Lumped mass model or frame model
Level 1 earthquake -Story drift must be less than serviceability drift limit. -No yielding in members.	For frame model the maximum member response must be below the yield point of member capacity curve. For lumped mass model the maximum story shear must be within elastic stage of story capacity curve
Level 2 earthquake Drift at the load center must be less than response drift limit -The maximum story drift must be less than 1.5 times response drift limit -Yielding is allowed in members but no degradation of lateral resistance of structure	
Criteria for static design -At the level of design drift limit, base shear coefficient C_B must be more than $0.25RtZ$ - Enough ductility in hinge members - Enough strength in non-hinge members	 Using reliable strength. Using upper strength.

1.2.3 Possible Mega Earthquake

In order to consider possible mega earthquake in the future, the design criteria of buildings under post-level 2 earthquake is suggested. The largest anticipated earthquake which is supposed to be occurred in the future in japan called Nankai Trough earthquake (Okawa, et al., 2013). The Nankai mega earthquake is a great earthquake that occur along the fault that forms the plate interface between the subjugating Philippian sea plate and the overriding Amurain plate (part of the Eurasian plate) which dips beneath southwestern Honshu, Japan as shown in Figure 1.2.4.

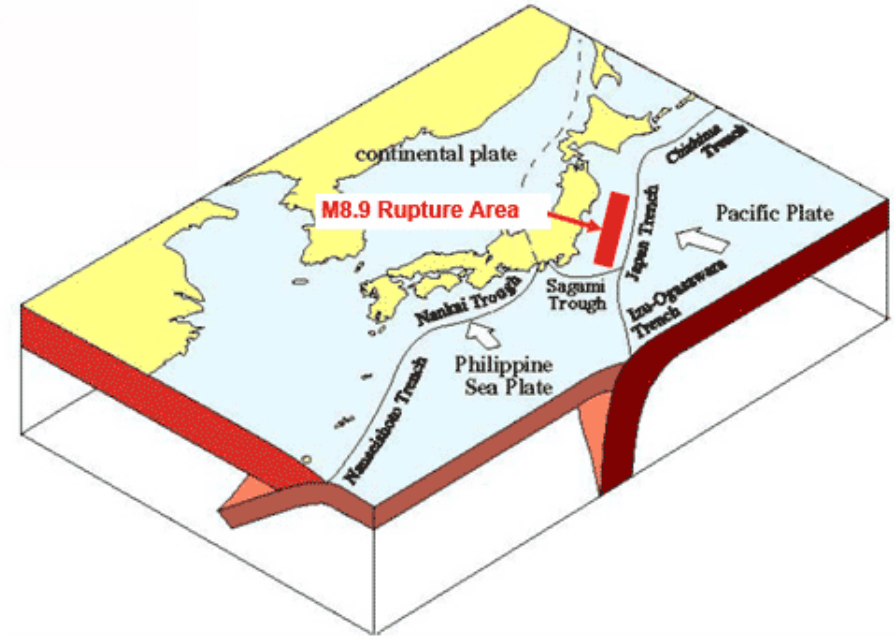

Figure 1.2.4 Nankai Trough location

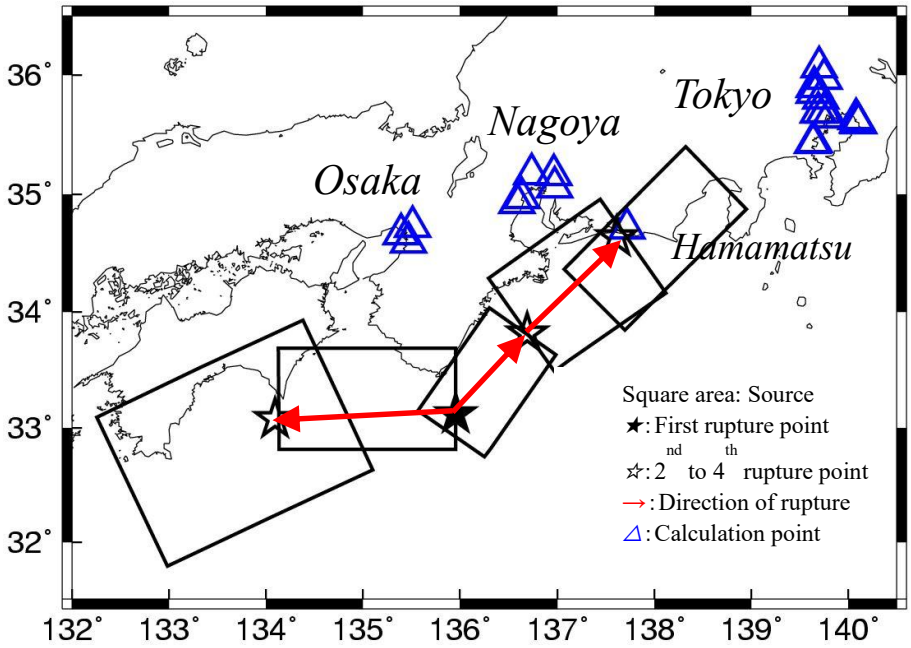

Figure 1.2.5 Source model for Nankai Trough Earthquake (Okawa, et al., 2013

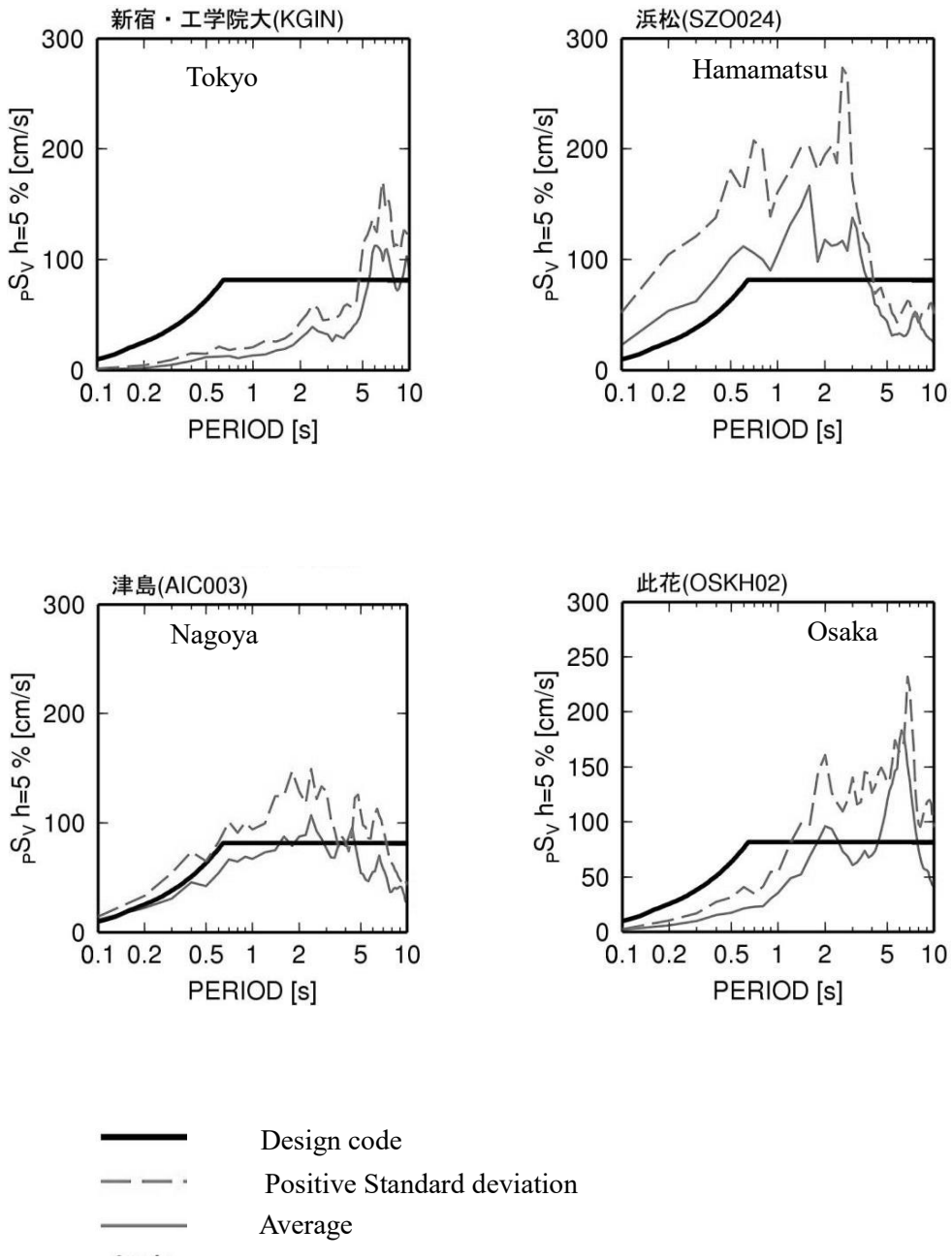

Figure 1.2.6 Response Velocity Spectrum (Okawa, et al., 2013)

1.2.4 Design criteria for post-disaster management facility

A disaster base facility or post-disaster management facility refers to the headquarter of disaster response building of a local government which serves as a base for emergency response such as information collection and countermeasure instructions.

A design guideline for disaster base facilities provided by the National Institute for Land and Infrastructure Management (NILIM) recommends the utilization of non-structural wall components made of reinforced concrete, such as wing walls and spandrel walls, to increase ductility of members and provide capability for continuous use of buildings. In order to gently involve the spandrels and wing walls in the load carrying scenario of the frame member, the seismic slit needs to be removed and wall segments are to be casted monolithically with structural members (NILIM, 2018). The either removal or reduction of the seismic slit is expected to increase the strength of member and helps establishing NILIM required criteria for disaster management facility.

In addition to the explained seismic design criteria for building, (NILIM, 2018) provided a special guideline for post-disaster management building declaring design method of damage controlling of the reinforced concrete building utilizing non-structural walls. Accordingly, the guideline regards non-structural walls like wing walls, spandrels (hanging/standing walls), mullions as structural member unlike (AIJ, 2010a). This is to ensure that the building have strong enough capability to withstand during large earthquake and remains functional for post-disaster scenario.

Post-disaster management buildings are designed to response elastically during large earthquake and being able of functioning without any repairing. The building shall not undergo to an extensive damage under major earthquake and should have the capability of functioning without large reaping. The response of building has to be in the elastic range and cracking width shall not be more than 0.3mm. Detail of proposed guidelines for disaster base facilities is expressed in Table 1.2.4 and Figure 1.2.7.

In order to ensure the serviceability of the building during and after earthquakes, the impact of non-structural wall should be considered. The lateral drift of moment resisting frame stands at 1/300 in case the impact of both spandrels and wing walls are considered. In this case the base shear coefficient equals to 0.55 and the seismic slit is completely removed. Likewise, the frame drift stands at 1/200 in case only the impact of wing wall is considered and there is seismic slit between wing wall and hanging wall. In this method the base shear coefficient equals to 0.4 and damage occurs around the seismic slit.

Table 1.2.4 earthquake design criteria for post-disaster buildings

Guideline provisions	Inter-Story drift	Member ductility factor (μ)	Base shear coefficient	Status of building
Method I	δ1 < 1/300	<1	0.5	Functioning and damage is appeared
Method II	δ2 <1/200	<2	0.4	Functioning and needs repairing

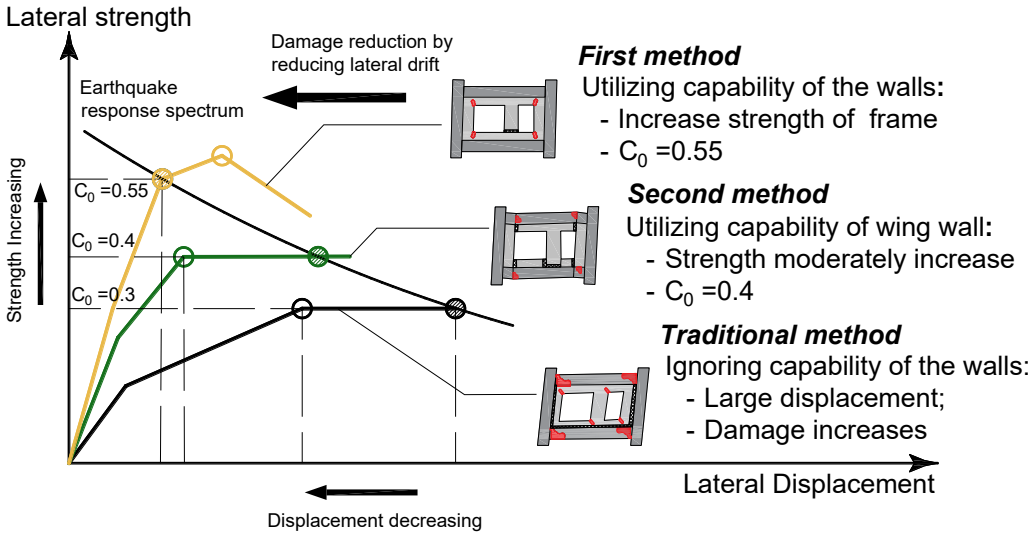

Figure 1.2.7 NILIM proposal for disaster management buildings

1.3 Design method of member with non-structural walls

1.3.1 Typical reinforced concrete non-structural walls

The reinforced concrete wall members which are supposed to be non-load bearing component in the reinforced concrete building, is referred to non-structural element. The reinforced concrete non-structural walls include a wide range of elements such as wing walls, spandrels (hanging/standing walls), mullion walls and so on. The shape of non-structural wall is determined by the shape of opening which may causes vulnerability and complication of damage mechanism during earthquakes as shown in Figure 1.3.1.

The openings in the wall effect the flexural strength, shear strengths and change the load path around the openings. If the opening is near the middle of the wall, it will decrease the moment capacity of the wall only slightly; however, the shear strength may be significantly reduced. In

contrast, an opening near a wall boundary may impact both shear and flexural strengths, depending on the size of the opening (Taylor et al. 1998).

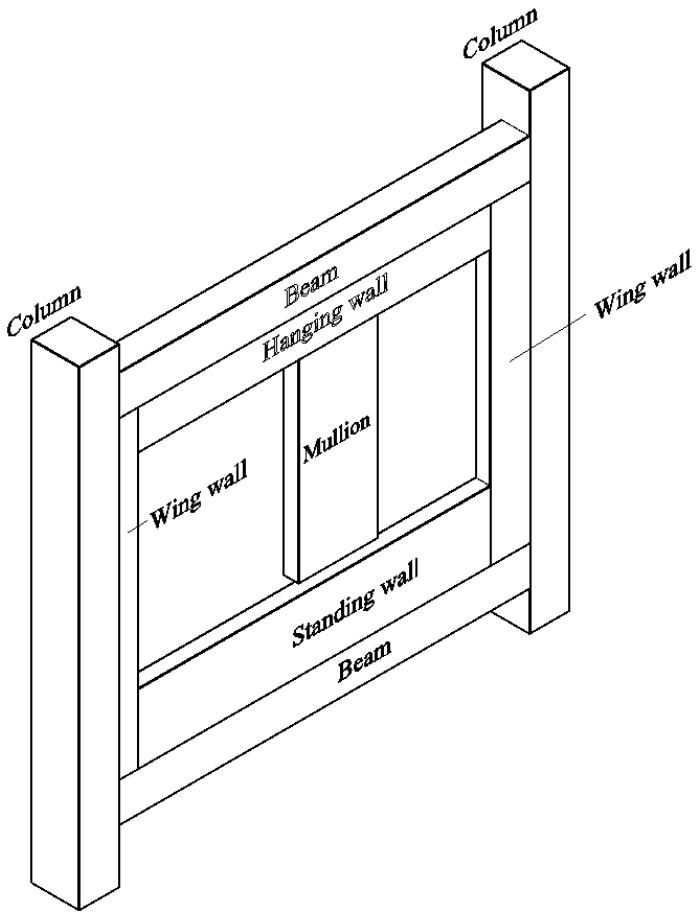

Figure 1.3.1 Non-structural formed as a result of window opening

The Architecture Institute of Japan (AIJ) regards walls with minimum thickness of (≥ 120 mm) and quantity of reinforcement (reinforcement ratio ≥ 0.25%) as structural component in case the walls are designed to bare loads (AIJ, 2010a). The other walls incompatible with the definition of structural component is considered to be non-structural elements. The usage and design philosophy of reinforced concrete non-structural walls are changed following each significant earthquake. The Japanese building standards after amendment of 1981, allowed the premature failure of non-structural walls, in case it does not adversely affect the structural member.

1.3.2 Researches on Reinforced concrete members with non-structural walls

Japanese design standards treat spandrel walls (hanging and standing walls) as a non-structural element in the primary concept of design and suffices to calculate the stiffness and weight of the spandrels. Generally, provided seismic slit at both end of the walls are tended to isolate the spandrels and counteract their further impact on the performance of buildings.

At present, the researches about typical non-structural spandrel wall, is insufficient and limited to overall impact of the walls on performance of structural members. The results from an experimental test with reinforced concrete moment resisting frames with non-structural wing walls casted to be monolithic with frame elements showed higher initial stiffness and lateral strength in the member with the monolithic non-structural wall (Yoon, et al., 2017). However, significant strength degradation was observed after the lateral strength peak was reached. This degradation was assumed to be caused by the damage in non-structural walls, where the longitudinal reinforcement was anchored into the structural system.

To minimize damage to the wing walls due to wall reinforcement, it was suggested that the reinforcement within these non-structural walls be terminated before at the end of the walls rather than being anchored into other elements (Tsubaki, et al., 2019). In the proposed modification, the influence of confinement transverse reinforcement (the volume of which can be determined based on (AIJ, 2016) and American Concrete Institute (ACI) standards (ACI, 2014) on the ductility capacity of non-structural wall members was investigated.

In a similar experimental study conducted by (Nayuko, et al., 2015), it was observed that a beam member having spandrel wall at one side either as hanging or standing walls, may fail in the shear. The shear failure occurs at the boundary of beam due to action of higher flexural strength resulting from the wall. It was further verified that increase of transverse reinforcement prevents the shear failure of the beam.

1.3.3 design method of beam member with spandrel wall

The beam member having spandrels (hanging and standing walls) requires to be designed so that to can carry applied load without altering the global collapse mechanism of building. To consider this principle (AIJ, 2010) suggests to consider following characteristic during analyze and design of the member;

- Rigidity of the beam with spandrel (hanging/standing walls), connected to the moment frame resisting frame without seismic, shall be calculated in accordance to the bending deformation and shear deformation. The bending deformation of the beam member is obtained using the moment of inertia of the member's section which includes section of beam and spandrels, and the shear deformation is calculated with Equation (1.3.2). The moment of inertia and shear stress distribution along the member section shall be carried out in accordance to the center of geometry of the beam member. The elastic rigidity of the beam member shall be calculated using an appropriate evaluation of the stress state of the spandrels that is connected to the frame with seismic slit.

In the absence of the seismic slit, the elastic rigidity of beam member having spandrels, is calculate with the Equation (1.3.1).

$$\frac{1}{K_0} = \frac{1}{K_s} + \frac{1}{K_{be}} \tag{1.3.1}$$

$$K_s = \frac{G_c\, A_0}{K_e l} \tag{1.3.2}$$

$$K_{be} = \frac{12 E_c I_e}{l^3} \tag{1.3.3}$$

Where

K_0: is the elastic rigidity (N/mm)

K_s: is the shear stiffness (N/mm)

G_c: is the shear modulus of concrete (N/mm^2)

E_c: is the modulus of elasticity of concrete.

l: is the length of beam span.

I_e: is the equivalent moment of inertia of the member including the concrete displaced by the reinforcing bars.

K_e: is the shear shape factor obtained using Equation (1.3.4).

$$K_e = \frac{6\,(2\alpha\beta + 1)\{(30\alpha^2\beta^2(\beta+1)^2 + 2\alpha\beta\,(16\beta^4 + 25\beta^3 + 10\beta^2 + 5\beta + 5) + 1\}}{5(8\alpha\beta^3 + 12\alpha\beta^2 + 6\alpha\beta + 1)^2} \tag{1.3.4}$$

Where;

α: is the ratio of wall thickness to beam widths.

β: is the ratio of wall depth to beam depth.

- When calculating the bending moment of a beam with spandrels, the influence of the spandrels should be taken into account, particularly, in the calculation of the section modulus of the member. However, when a seismic slit is presented, the strength of beam at the end requires to be calculated only by the beam cross section, ignoring the influence of hanging and standing walls. the ultimate bending moment of the beam member having spandrels are obtained using Equations (1.3.5) to (1.3.8).

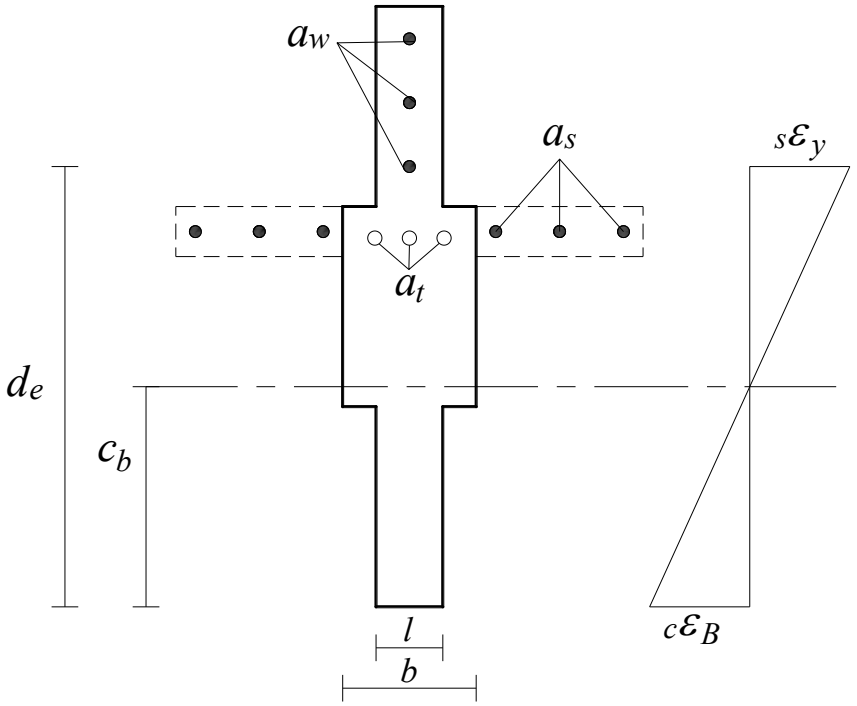

Figure 1.3.2 Beam member having standing and hanging walls

$$M_u = a_{te} f_y \, (d_e - \frac{1}{2} \, c_b) \tag{1.3.5}$$

$$a_{te} = a_t + \sum a_{tw} \left(\frac{f_{wy}}{f_y} \right) + \sum a_s \left(\frac{f_{sy}}{f_y} \right) \tag{1.3.6}$$

$$a_{te} \leq \frac{0.85 f'_c t \, c_b}{f_y} \tag{1.3.7}$$

$$c_b = \frac{{}_c\varepsilon_B}{{}_c\varepsilon_B + {}_s\varepsilon_y} \, d_e \tag{1.3.8}$$

Where;

a_t, a_w, a_s: are the cross-sectional area of beam, wall and slab tensile reinforcements (mm^2).

a_{te}: is the total equivalent area of reinforcements in beam, wall and slab that carrying tensile forces.

f_y, f_{wy}, f_{sy}: are the yielding strength of beam, wall and slab tensile reinforcements (N/mm^2).

f'_c: is the concrete compressive strength (N/mm^2)

c_b: is the depth of neutral axis (mm).

d_e: is the distance between an equivalent tensile reinforcement of the spandrel wall from extreme compression fiber (mm).

${}_c\varepsilon_B$: is the concrete compressive strain at the extreme compression fiber.

$_s\varepsilon_y$: is the tensile strain of tensile reinforcements.

- The ultimate shear strength of a beam member having spandrel wall is also calculated using Arakawa and Ohno equation as following;

$$Q_{su} = \left[\frac{0.083\, p_{te}^{0.23} (f_c' + 18)}{M/Qd_e + 0.12} + 0.85 \sqrt{p_{we}\, f_{wy}} \right] bj \qquad (1.3.9)$$

Where;

p_{te}: is the ratio of the area of the tensile reinforcing bars to the cross-sectional area

f_c': is the concrete compressive strength (N/mm^2)

M/Q: is the shear span-to-depth ratio.

d_e: is the depth from the tensile reinforcing bars to the compressive extreme fiber

p_{we}: is the ratio of the area of the transverse reinforcements to the perpendicular cross-sectional area.

f_{wy}: is the yield strength of the transverse reinforcement (in N/mm^2).

b: is the width (thickness).

j: is the distance between a compressive/tensile force couple on the critical section (commonly replaced by (7/8)d).

In case the axial force N is existed following equation is used to predict shear strength of either beam or column having non-structure wall:

$$Q_{su} = \left[\frac{0.083\, p_{te}^{0.23} (f_c' + 18)}{M/Qd_e + 0.12} + 0.85 \sqrt{p_{we}\, f_{wy}} \right] bj + 0.1N \qquad (1.3.10)$$

Chapter II

Impact of the Reinforcement Detailing on Seismic Performance of Isolated Non-structural Walls

2.1 Introduction

Following the observation of severe damage to structurally isolated non-structural reinforced concrete (RC) walls after major earthquakes in Japan, such as the great Tohoku earthquake in 2011, researchers began to reassess the effectiveness of connection details of a non-structural wall segment to a moment-resisting frame.

The Architectural Institute of Japan suggests that wall segments functioning as hanging or wing walls should be considered as non-structural elements during the structural design (Izumi, et al., 2016). Under the current design practices in Japan, RC wall segments are often structurally isolated from the RC moment-resisting frames by a seismic slit (a gap) installed between the wall segment and primary frame, as shown in Figure 2.1.1a.

Several studies have reported that non-structural walls affect the seismic performance of RC buildings in case the wall is isolated with presence of seismic slit (Ju, et al., 212; Kabeyasawa, et al., 2014; Orakcal, et al., 2009). The presence of seismic slit (the height of slit was selected to be 1.5% of the wall height) prevents interaction of the infill wall and moment resisting frame up to the 1.5% drift (Ju, et al., 2012). Similarly, Lee, et al., (2008) confirmed through an experimental test that the presence of seismic slit which is designed to be 1.5% of height of wall, prevent interaction of the wall and moment resisting frame. Yanagisawa, (2008) tested 1/6 scale specimens and expressed that isolating of the monolithically casted infill wall from moment resisting system using seismic slit (the height of slit was selected to be 1.8% of the wall height) does not change the behavior of the moment resisting system and the response is similar to the frame having infill wall without seismic slit.

On the contrary, AIJ (2010b) suggest to connect non-structural concrete walls with moment resisting frame without seismic slit and anchors its longitudinal reinforcement to the adjacent member in order to avoid out-of-plane deformation. however, it is believed that the anchorage of

the wall to the main frame might result in stress transformation to the non-structural wall and may cause premature damage to the wall.

According to the Japanese building standards, structural design of non-structural spandrel walls, casted monolithically with the frame, generally follows the design criteria of the structural walls. The response of the spandrel walls under lateral load is similar to that of the shear walls working in the compression, hence the observed indications of the shear walls can be considered for the spandrels. However, the axial load is not subjected to the hanging wall unlike shear walls, which may give different design requirement to the walls.

Structural test results of a multi-story frame with non-structural wall showed that the thickness of the non-structural wall greatly affects the collapse mechanism as explained in section 1.2.1. As the beam-to-column strength ratio approaches 1, the damage to the wall around the beam-to-column joint increases, and there is a risk of column damage due to the large damage to the wing wall, in particular, resulting in layer collapse.

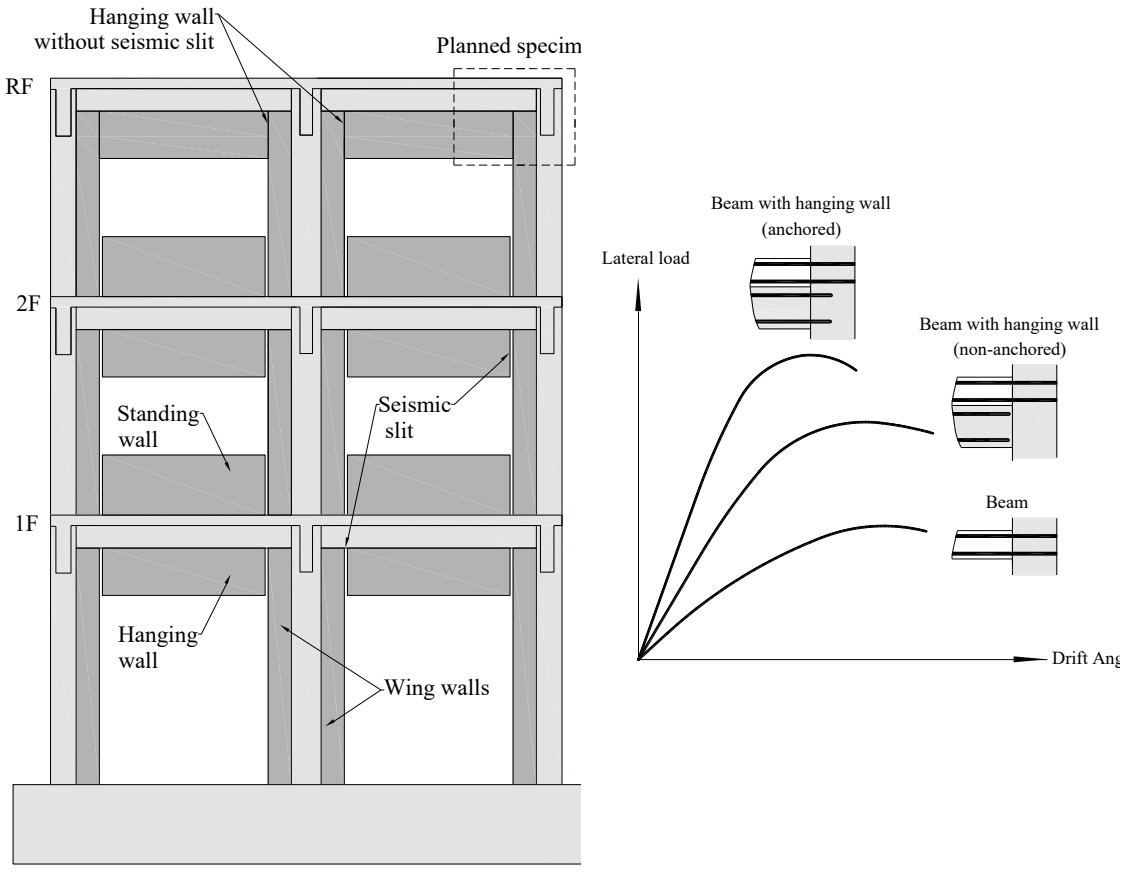

(a) (b)

Figure 2.1.1. (a) Proposed detailing of a frame with a hanging wall with and without a seismic slit; and (b) their expected performance

The required transverse reinforcement at the shear wall boundary and the configuration of anchorage of longitudinal reinforcement, has been tested to address the issues associated with wall thickness, slenderness, axial load, and configuration; as well as the expected displacement demands and load history. As a result of damage investigation of concrete buildings after number of earthquakes, it was observed that the structural wall damages included boundary crushing, reinforcement fracture, and lateral wall buckling (Wallace et al., 2012). Following the earthquake in Chili (2010) and Japan (2011), observed damages in RC wall raised concerns about the seismic performance of rectangular RC walls in numerous walled building leading to partial or total collapse (Kato et al., 2010; Moehle et al., 2010).

(Johnson, 2010) tested isolated cantilever shear walls to investigate the behavior of anchorage details of flexural reinforcement. The results indicated an adequate performance in the case of the coupler and showed that the presence of a splice significantly reduced the lateral deformation capacity of the wall. Likewise, researchers experimentally evaluated the effect of the wall cross-section shape on the seismic behavior of a shear wall has been investigated by several researchers and it has been shown that the wall strength, stiffness, and ductility depend greatly on the shape of the wall (Paulay, 1986a; and Moehle, 1989).

It has been found that thin, rectangular sections confined by the outer hoop and intermediate legs of crossties at the wall boundaries, as allowed by American Concrete Institute (2014), were less stable than sections using overlapping hoops for confinement of shear walls (Welt, 2015). Segura et al. (2018) studied the relationship between wall thickness and lateral drift capacity and found that thin walls possess lower lateral drift capacities than thicker walls.

An alternative method of connecting hanging wall segments to the frame or another wall was suggested without a seismic slit (Walid, et al. 2020), as shown at the roof level in Figure 2.1.1a. However, AIJ (2010b) provides anchoring of the hanging wall longitudinal reinforcement to the adjacent member. Under these circumstances, the longitudinal reinforcement of the hanging wall could either be anchored to the adjacent member (wing wall or column) or not. Hereinafter, the anchored reinforcement is referred to as the anchored detailing and the non-anchored reinforcement is referred to as the non-anchored detailing. It is generally assumed that the anchored detailing of the longitudinal bar increases the wall strength, whereas the non-anchored detailing establishes better deformability, as shown in Figure 2.1.1b.

This study ascertains the impact of transverse reinforcement, different connection methods of hanging walls with the moment-resisting frame using the anchored and non-anchored detailing of longitudinal reinforcement; impact of boundary confinement on the longitudinal bars considering different detailing; and slenderness on the performance of hanging wall against flexural load. It also evaluates workability of the transvers reinforcements and reinforcement detailing with concrete. For this reason, six different hanging wall specimens were tested under cyclic loading.

The specimen parameters are the amount of sectional confinement (a complete stirrup hooked to the beam), existence of a boundary confinement, anchorage and non-anchorage of longitudinal reinforcement, amount of longitudinal reinforcement, and slenderness. The data analysis is then used to suggest a reinforcement detailing and confinement arrangement that fabricate a wall with high lateral drift capacity and strength.

2.2 Experimental Study

Several test specimens comprising of a beam and with a monolithically-casted hanging wall were made, where the hanging wall was connected to the adjacent vertical structural member without a seismic slit. Wall members were half scale and corresponded to the prototype wall shown in Figure 2.2.1, except the beam element which is without a specific scale factor. This was because the specimens are designed in such a manner that extreme compression is applied on the hanging wall boundary during the test; the beam remains elastic and the performance evaluation is focused on the hanging wall rather than the beam.

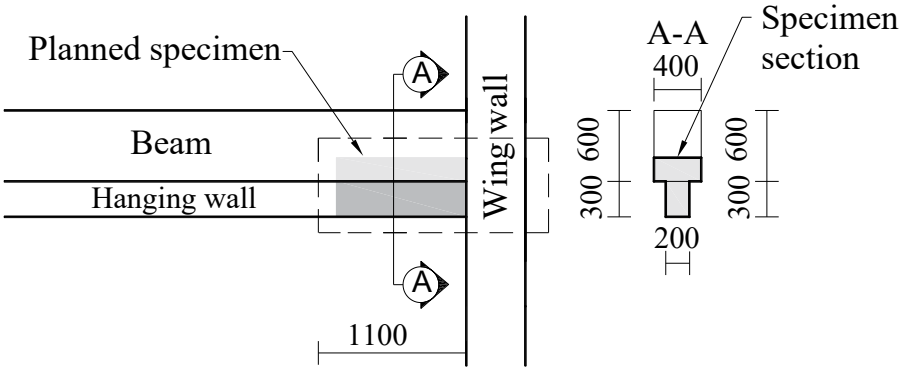

Figure 2.2.1. Prototype specimen

The test specimens were designated as 3NN, 3NA, 6NA, 12NA, 12HN, and 18NNT as shown. The numbers at the beginning of specimens inferred from rounded amount of wall transverse reinforcement multiplied by 10; first letter indicates having (H) or not having (N) boundary confinements; second letter anchorage (A) and non-anchorage (N); and third letter variation of the thickness (T). The cross-sectional dimensions of the hanging walls were 100 mm × 150 mm for all specimens, except for 18NNT which was 75 mm × 150 mm. The shear span length was 550 mm; and the shear span-to-depth ratio was 3.67. The beam which the hanging wall was connected to had a cross section of 100 mm × 200 mm.

The specifications of the reinforcement amount and information regarding detailing are shown in Table 2.2.1and Table 2.2.2. The steel bars, D6 (SD295A) and D4 (SD295A), were used as the longitudinal, transverse, and confinement bars for the shear wall and beam, while bars D16 (SD345) and D13 (SD345) were used as the longitudinal reinforcement of the beam.

Table 2.2.1 Reinforcement amount

Specimens	Cross Section (mm2)	Transverse Reinforcement		Longitudinal Reinforcement	
		Wall	Beam	Wall	Beam
3NN		D4@100 (ρt =0.28%)	D6@50 (ρt = 1.3%)	4-D4 (ρl = 0.37%)	4-D16 4-D13 (ρl = 6.51%)
3NA		D4@100 (ρt =0.28%)	D6@50 (ρt = 1.3%)	4-D4 (ρl = 0.37%)	4-D16 4-D13 (ρl = 6.51%)
6NA	100×150	D6@100 (ρt =0.63%)	D6@50 (ρt = 1.3%)	6-D6 (ρl = 1.26%)	4-D16 4-D13 (ρl = 6.51%)
12NA		D6@50 (ρt =1.27%)	D6@50 (ρt = 1.3%)	6-D6 (ρl = 1.26%)	4-D16 4-D13 (ρl = 6.51%)
12HN		D6@50 (ρt =1.27%)	D6@50 (ρt = 1.3%)	6-D6 (ρl = 1.26%)	4-D16 4-D13 (ρl = 6.51%)
18NNT	75×150	D6@50 (ρl =1.69%)	D6@50 (ρt = 1.3%)	6-D6 (ρl = 1.69%)	4-D16 4-D13 (ρl = 6.51%)

Table 2.2.2 Reinforcement detailing

Specimens	**Cross Section (mm2)**	**Boundary Confinement**		**Anchorage of longitudinal Bar**	**Reinforcement cases**
		Ratio (%)	**Depth (mm)**		
3NN				No	Minimum
3NA				Yes	
6NA	100×150	-	-	Yes	Medium
12NA				Yes	Maximum
12HN		1.27	450	No	Maximum
18NNT	75×150	-	-	No	Slenderness

Mechanical property of the concrete and steel bars were experimentally obtained before specimen test. For this purpose, several cylinder tests were carried out to recognize the concrete compression strength, strain, elasticity modulus as well as tensile strength as shown in Figure 2.2.2a.

The cylinder test data was recorded using three stain gauges for each cylinder. The elasticity modulus of concrete was found in the linear range of stress-strain relation. The upper boundary of linear relation of the stress and strain was assumed to be at point corresponding to 1/3 of the peak observed compression load.

The tensile strength of the concrete was observed by splitting tensile strength of the cylinder as shown in Figure 2.2.2b. The concrete mechanical properties of the specimens are shown in Table 2.2.3.

Table 2.2.3. Concrete mechanical properties

Compressive strength f'_c (MPa)	Strain at peak (%)	Young's modulus (MPa)	Tensile strength (MPa)
36.3	0.212	17374.6	2.7

(a) (b)

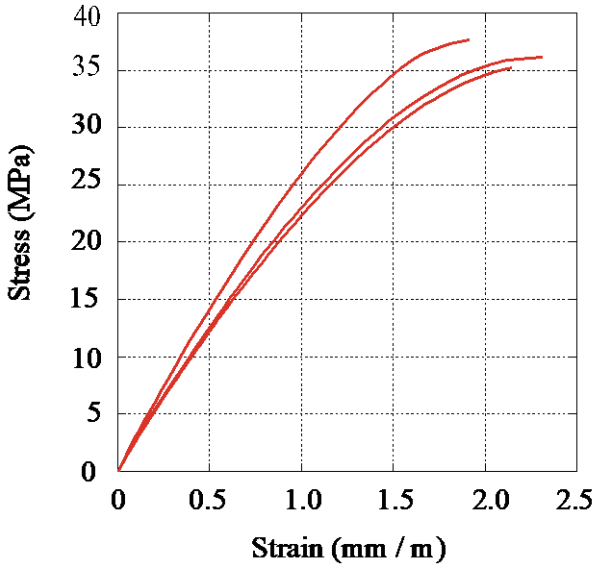

Figure 2.2.2. Concrete cylinder test: (a) compression test; (b) tensile test; (c) stress-strain relation of the concrete

Likewise, the stress-strain relation of the reinforcement bars was obtained from steel bar coupon test. Accordingly, a 200 mm coupon of the steel bars was punched at the middle by the eyelet punch tool to make a measurement spot. This was to measure strain from the eyelets of the steel coupon at the 100 mm length by strain gauges. The coupon was tested under the tensile force and

the strain-stress measurement was transferred to the data logger by strain gauge as shown Figure 2.2.3. The strength-strain relation of the specimen was developed based on the recorded data considering 0.2% offset in the strain of those bars experienced hardening as shown in Figure 2.2.4. The mechanical property of the reinforcement bars which were used in all specimens, are shown in Table 2.2.4 .

Figure 2.2.3. Coupon of a steel bar under the tensile strength test.

Table 2.2.4. Reinforcing bar mechanical properties

Reinforcements	Young's modulus (GPa)	Yield stress (MPa)	Ultimate strength (MPa)
D4	178.8	356.7	503.5
D6	185.6	338.3	501.7
D13	201.3	380.6	506.2
D16	203.4	383.8	568.9

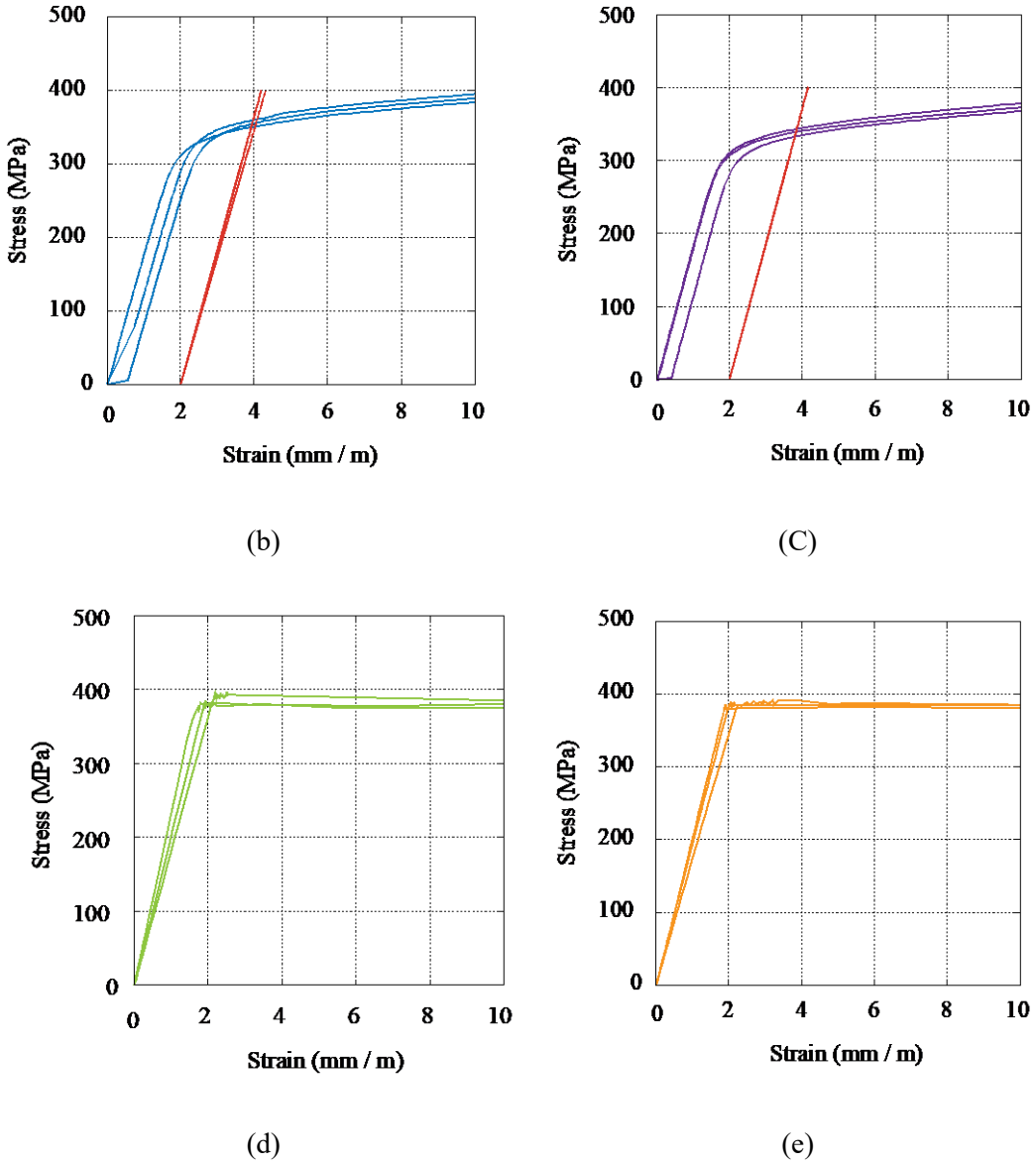

Figure 2.2.4.Tensile test of reinforcement bars: (a) tensile test setting; (b) stress-strain curve of D4; (c) curve of D6; (d) curve of D13 ; and (d) curve of D16

2.2.1 Test specimen 3NN

The specimen 3NN as shown in Figure 2.2.5, has a minimum quantity of transverse and longitudinal reinforcement in this test. The specimen 3NN was designed to test non-anchored detailing impact in case of minimum longitudinal and transverse reinforcements. In addition, this specimen was to ascertain a proper relation between longitudinal and transverse reinforcement that can incur higher strength and drift capacity to the hanging wall.

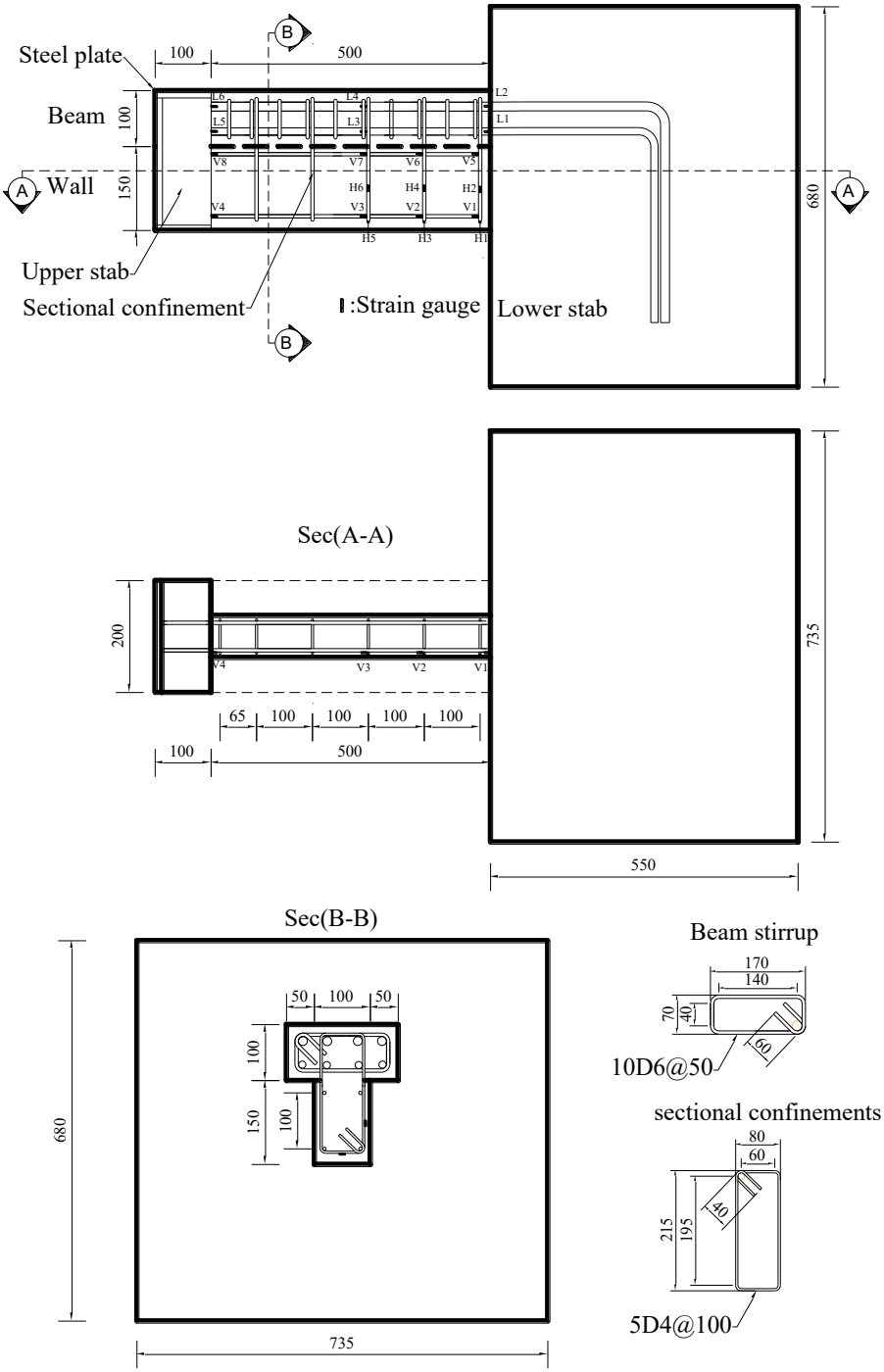

Figure 2.2.5. Detail of specimen 3NN

2.2.2 Test specimen 3NA

The specimen 3NA has also a minimum quantity of transverse and longitudinal reinforcement along with anchored dialing as shown in Figure 2.2.6. The specimen 3NA was designed to test anchored reinforcement impact in case of minimum longitudinal and transverse reinforcements.

It was also aimed to find out a relation between anchored longitudinal and transverse reinforcement that confers higher drift and strength capability to the spandrel wall.

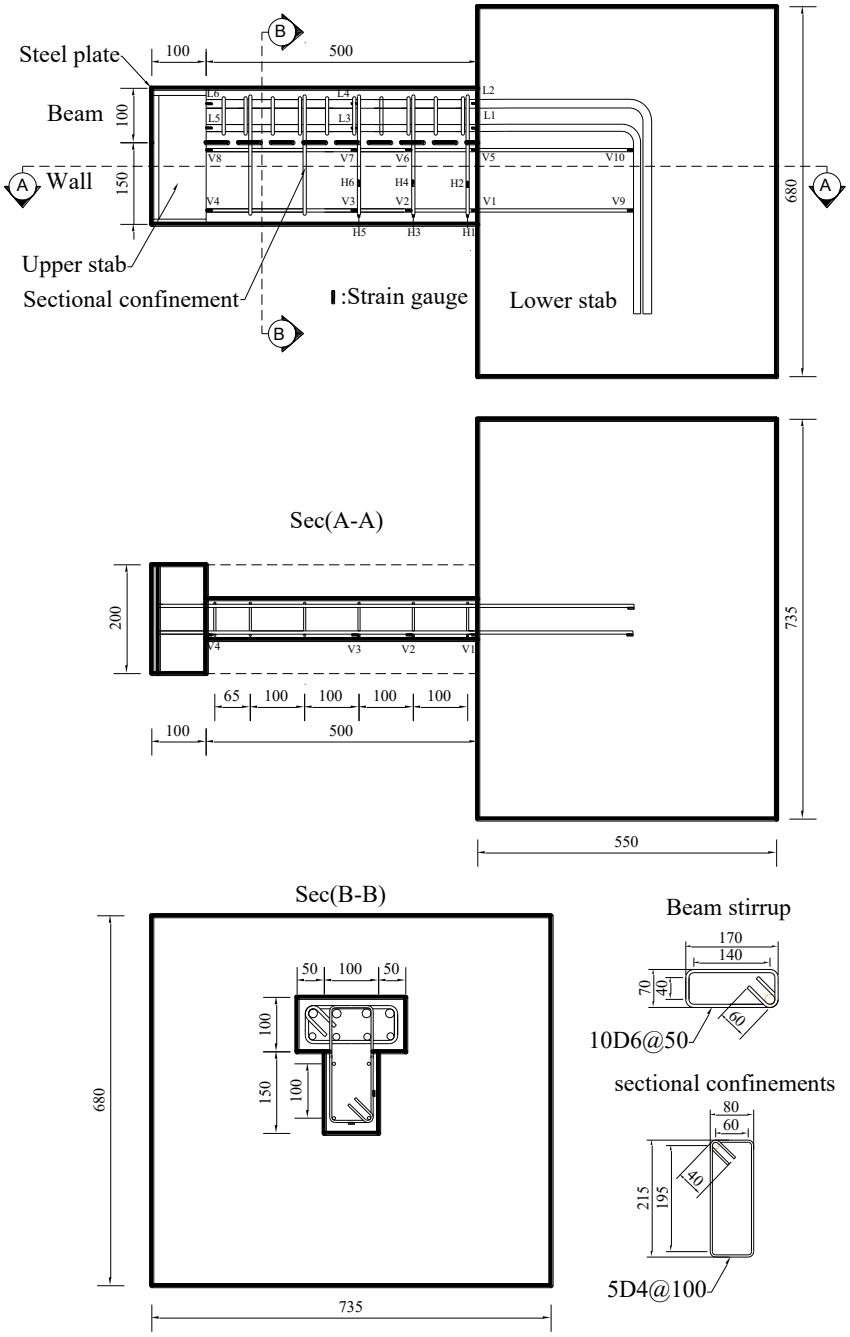

Figure 2.2.6 Detail of specimen 3NA

2.2.3 Test specimen 6NA

The specimen 6NA had half amount of the longitudinal reinforcements as a transverse reinforcement as shown in Figure 2.2.7. This amount of transverse reinforcements was considered as the medium reinforcement amount in this test. This specimen was aimed to observe the impact

of medium amount of transverse reinforcement on the capability of hanging wall considering anchored detailing of the longitudinal reinforcement.

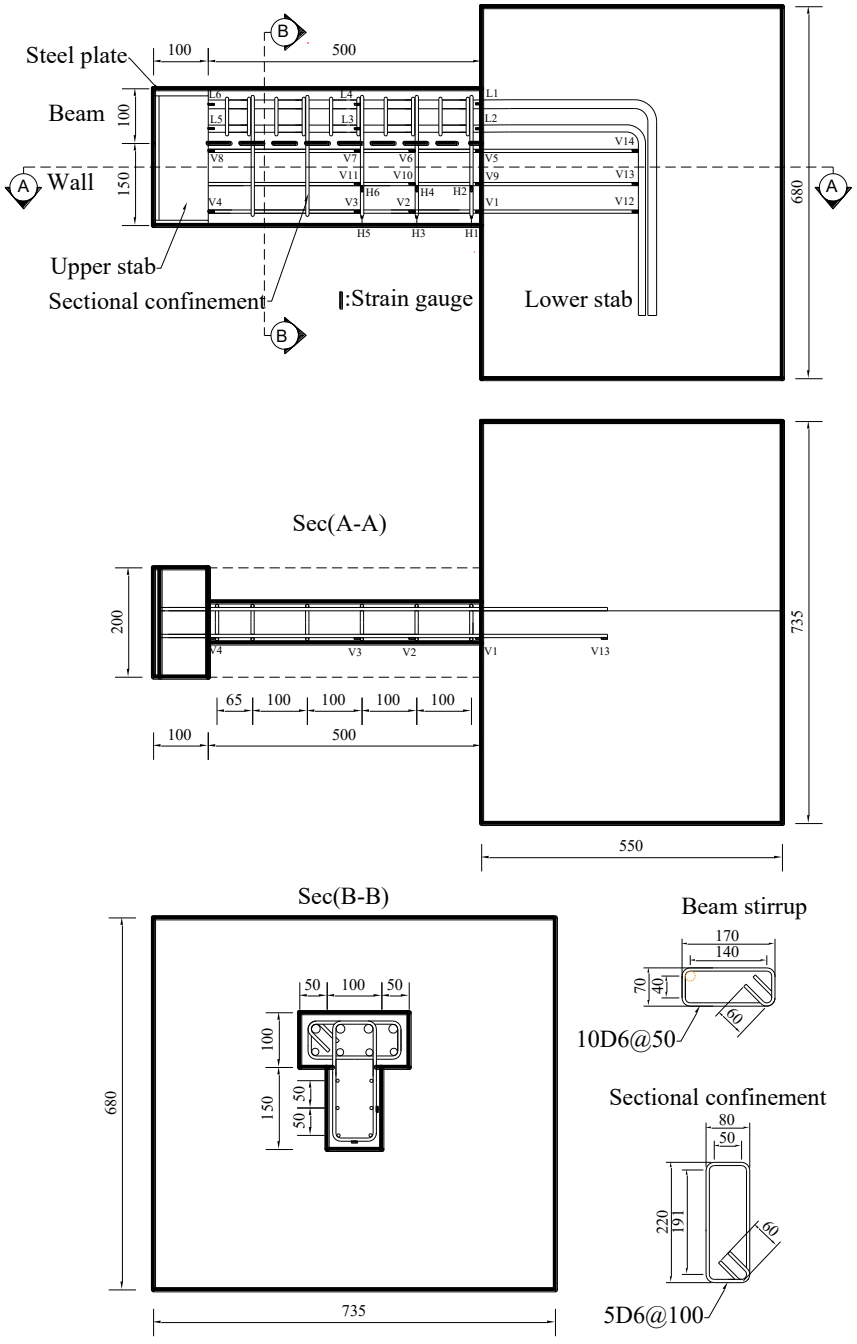

Figure 2.2.7 Detail of specimen 6NA

2.2.4 Test specimen 12NA

Specimen 12NA was designed to have the highest amount of transverse reinforcement among the series of anchored specimens as shown in Figure 2.2.8. Specimens 6NA and 12NA had equal amounts of longitudinal reinforcement but different amounts of transverse reinforcement Its

transverse reinforcement ρ_t amounted to 1.27%, which was twice that of specimen 6NA. It was aimed to quantify a proper amount of transverse reinforcement that confers higher drift and strength capacity to the hanging walls considering the anchored detailing of longitudinal reinforcement.

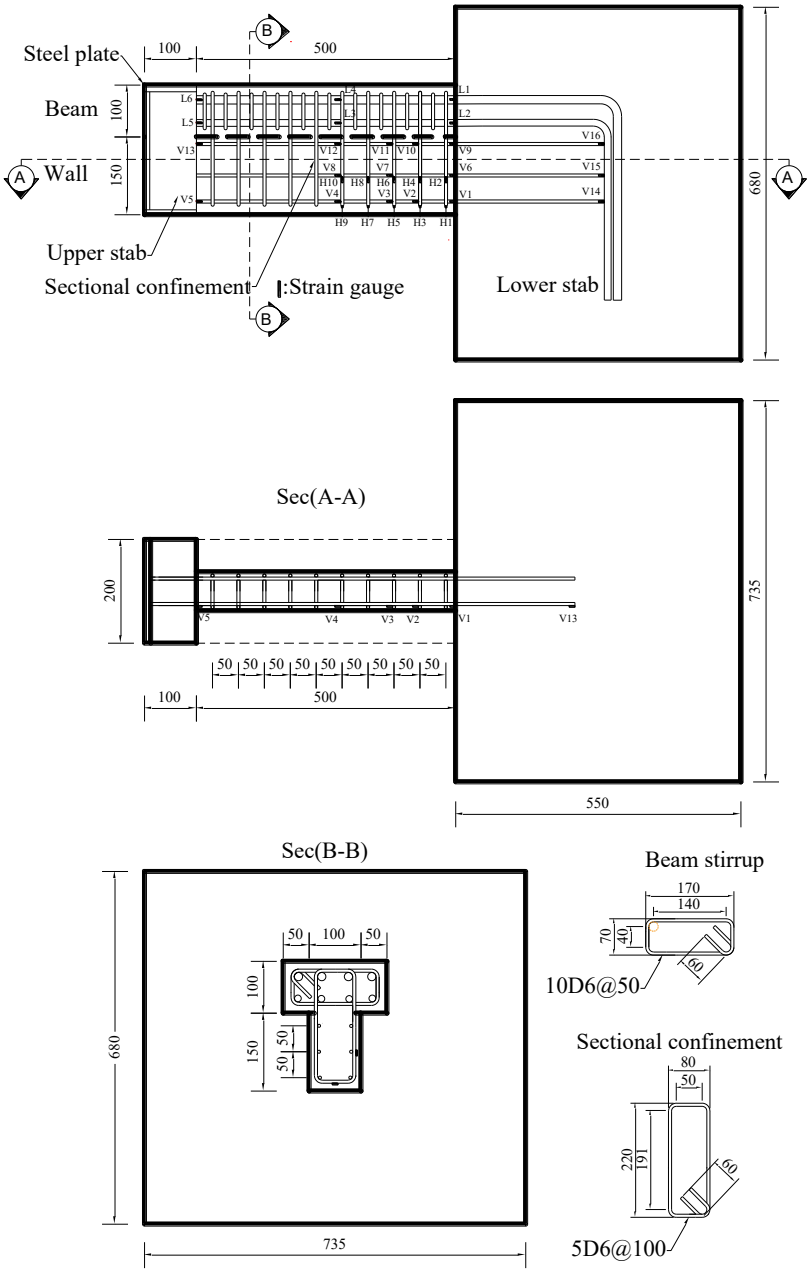

Figure 2.2.8 Detail of specimen 12NA

2.2.5 Test specimen 12HN

Specimen 12HN had the highest amount of the transverse bar in the series of non-anchored specimens with additional confinement stirrups as shown in Figure 2.2.9. Specimen 12HN had an

in-plane confined reinforcement of 1.27% in addition to the shear reinforcement of 1.27%. The specimen 12HN were designed to assess the workability of confinement reinforcing with non-anchored longitudinal reinforcement. It was also designed to test the impact of boundary confinement comparing to the sectional confinements on the concrete compressive strain-strength.

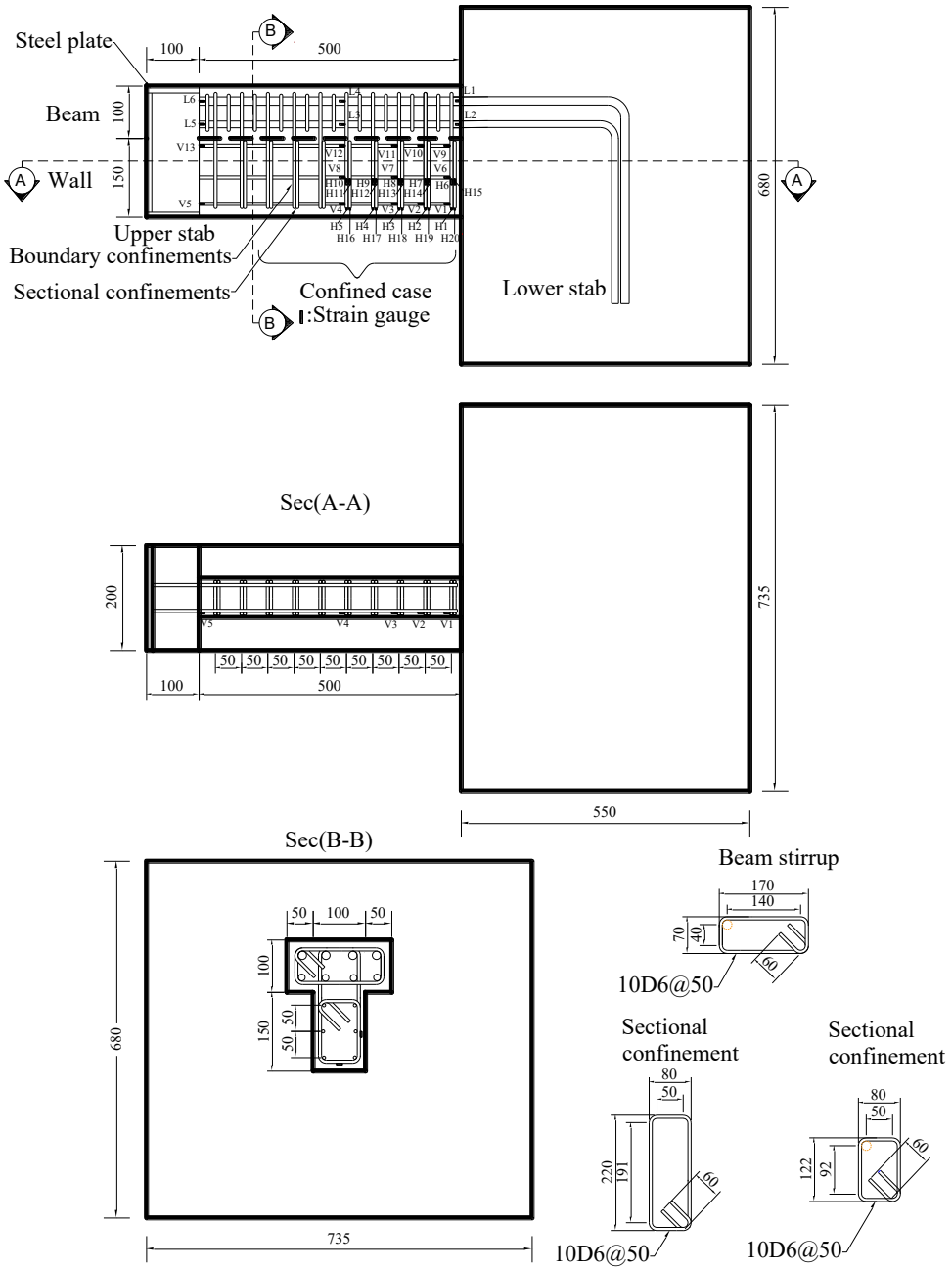

Figure 2.2.9 Detail of specimen 12HN

2.2.6 Test specimen 18NNT

The specimen 18NNT was the only specimen aimed to test the impact of slenderness on the performance of the hanging wall. The amount of transverse and longitudinal reinforcement were

equal with specimen 12NA and 12HN but the thickness was reduced to 75 mm. The AIJ standards suggests that the slender walls render more deformability to the beam member in case of anchored detailing. However; This specimen tested the impact of slenderness in case of non-anchored detailing.

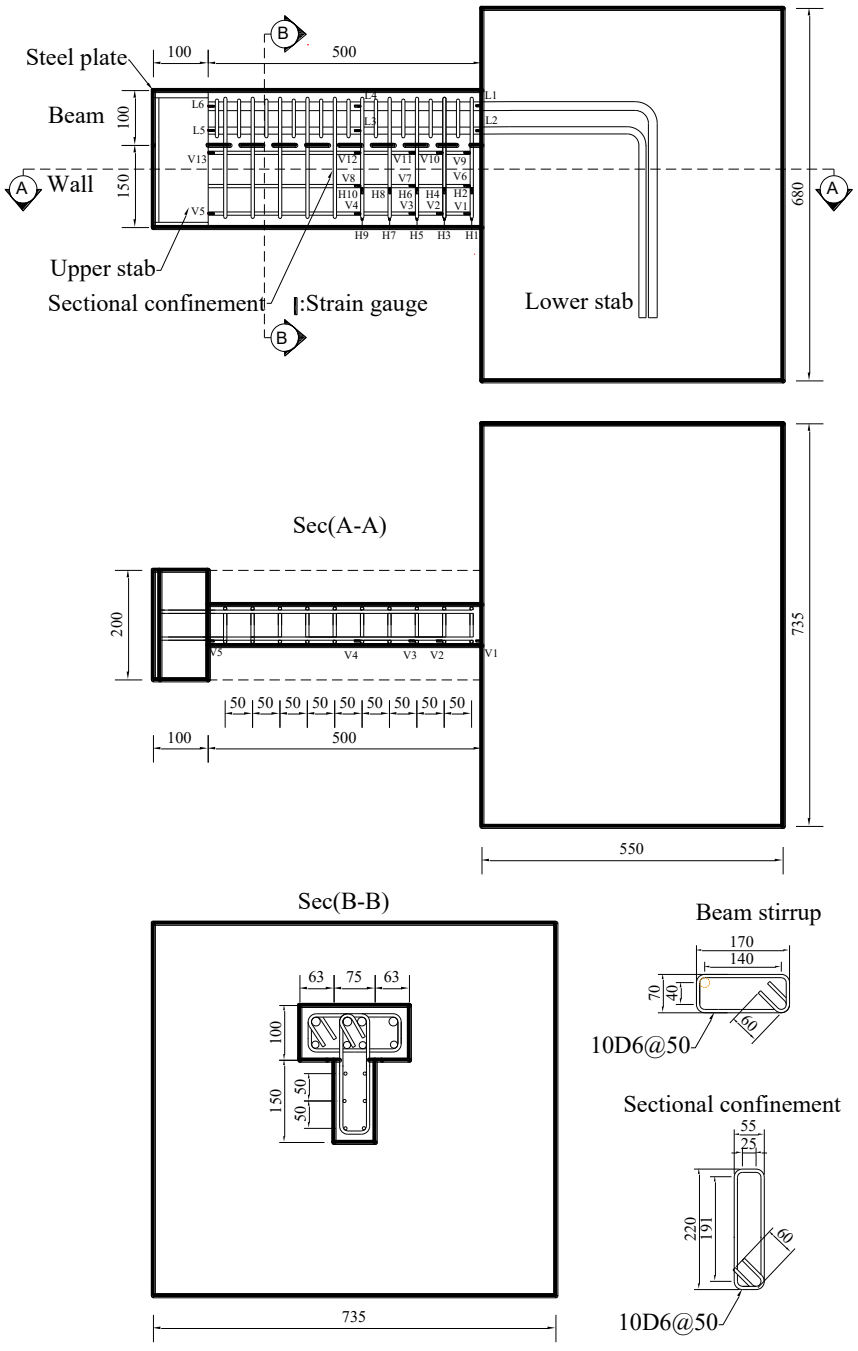

Figure 2.2.10 Detail of specimen 18NNT

2.2.7 Measurement instruments

A set of strain gauges were installed at the critical points and other points of interest on the longitudinal, transverse, and confinement reinforcement to investigate the detailing effect of the longitudinal reinforcement, confinements and insight collaboration of steel and concrete. The strain gauge location and tagged name were shown in detailing drawing of every specimen.

The external displacement of a specimen is controlled using a CDP-25 model of linear variable differential transducer (LVDT). The CDP-25 LVDT has a capacity to record the displacement until 25mm with ($500x10^{-6}$ strain/mm) sensitivity and 0.1% nonlinearity. These LVDT devices were installed at designated distances along the length of the specimen on the plane perpendicular to the thickness of the specimen and along the length of the beam on the plane perpendicular to the width, as shown in Figure 2.2.11. The LVDTs (TU1, TU2, TU3, and TU4) measured the horizontal displacement of the designated strip during negative loading cycle, while the transducers (TB1, TB2, TB3, and TB4) measured the hanging wall movement.

The total displacement (T. DISP) of the specimen was recorded using two CDP-50 (LVDT) as shown in Figure 3. The CDP-50 has 50mm recording capacity regarding displacement with ($200x10^{-6}$ strain/mm) sensitivity and 0.1% nonlinearity. The T. DISP (LVDT) was installed on the extended channel, perpendicular to the upper stab of the specimen to record the total displacement of the specimen as shown in Figure 3.

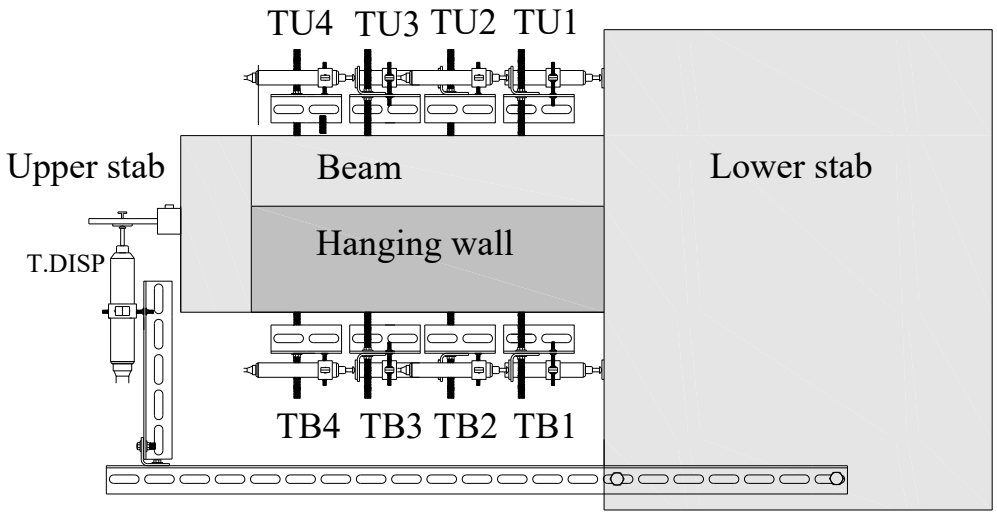

Figure 2.2.11 Measurement LVDTs

3.2. Testing program of the Specimen

Each specimen was installed horizontally on the universal testing machine, as shown in Figure 2.2.12 Figure 2.2.13.The lower stab was the fixed end and load was applied on the upper stab. Each specimen was tested under cyclic loading. The up-down loading represented by the plus sign denotes positive loading where the hanging wall acted in compression; while the down-up

loading indicates negative loading as shown by the minus sign where the wall acted in tension. Each specimen was positioned over the steel table of universal testing machine to be tested under the positive loading, while negative loading was applied by the external jack manually installed on the steel table under the upper stab. The steel plates located under and over the specimen were used to make space for specimen deformation during loading. The lower plates were removed during positive loading cycle and upper plates were removed during negative loading cycles.

The total displacement (T. DISP) of the specimen was recorded using two CDP-50 (LVDT) as shown in Figure 3. The CDP-50 has 50mm recording capacity regarding displacement with ($200x10^{-6}$ strain/mm) sensitivity and 0.1% nonlinearity. The T. DISP (LVDT) was installed on the extended channel, perpendicular to the upper stab of the specimen to record the total displacement of the specimen as shown in Figure 3.

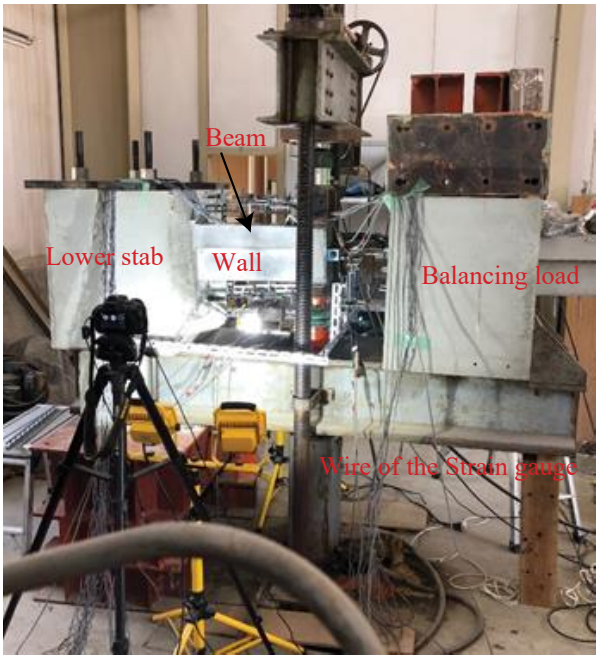

Figure 2.2.12 Set up configuration

All specimens were tested under cyclic loading with ±5kN initial loading and ±1/800, ±1/400, ±1/200, ±1/100, ±1/75, ±1/50 and ±1/25 drift sequences. The assumption for the test specimen was that if the strength capacity of the succeeding step in a loading cycle was found to be higher than 80% of that of the earlier step, the test will continue. Otherwise, loading was stopped as the specimen would be deemed to be significantly damaged.

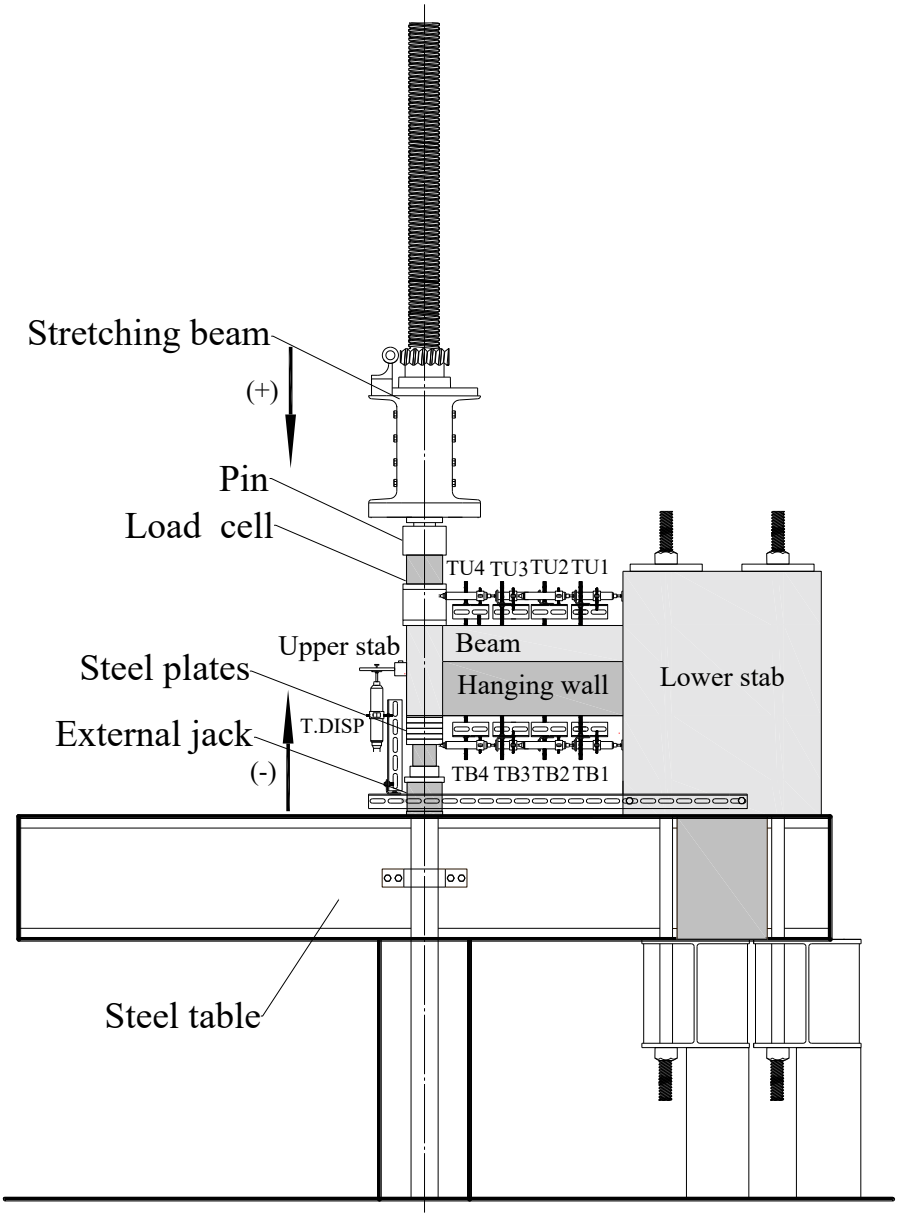

(a) Side view of the test set up

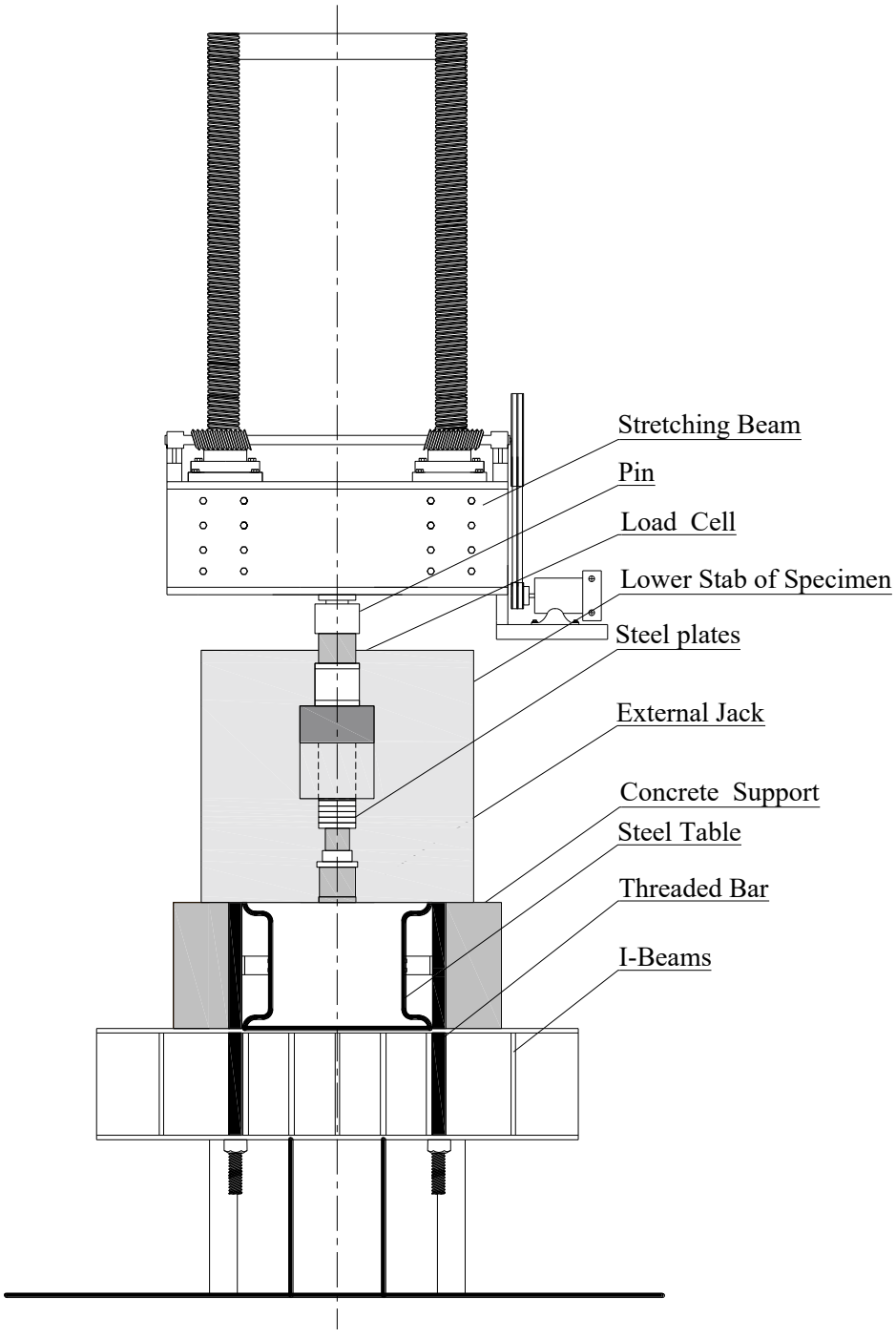

(b) Front view of the test set up

Figure 2.2.13. Configuration of specimen setting on testing machine

.

2.3 Experimental Results

2.3.1 Damage Outline

The observed cracking patterns are depicted in Figure 2.3.1 at the drift of 0.02 rad. The red patterns indicate the appeared cracks under the positive loading and the black pattern show the cracks under the negative loading direction. The horizontal dashed lines represent the location of longitudinal reinforcement closest to the edge of the wall. Different types of cracks occurred in all specimens owing to different amounts of transverse, longitudinal, and reinforcement detailing.

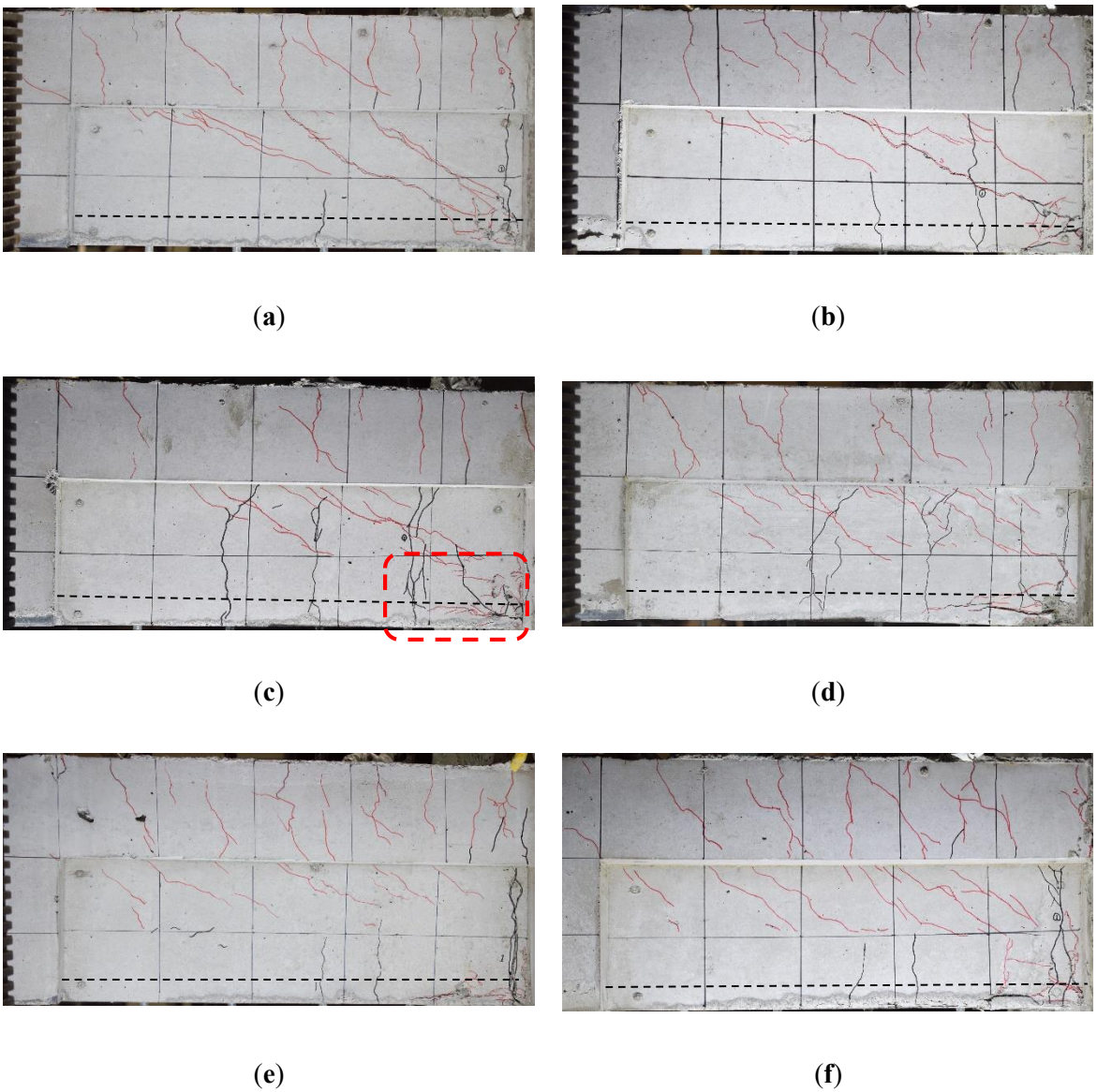

(**a**) (**b**)

(**c**) (**d**)

(**e**) (**f**)

Figure 2.3.1. Damage outline at the drift limit +0.02 rad: (a) 3NN; (b) 3NA; (c) 6NA; (d) 12NA; (e) 12HN; (f) 18NNT

For anchored specimens, crack propagation began with the appearance of the first shear crack at the critical zone of the wall, near the lower stab and spread along the wall length with the increase of the negative loading. Consequently, the flexural cracking on the wall occurred at the beam and spread along the specimen with the increase of positive loading.

As the load gradually increased, the crushing of the concrete compression zone occurred at the root of the compression strut under the positive loading. The anchored longitudinal reinforcement in the specimen 3NA experienced out-of-plane buckling owing to having minimum sectional confinement(see Figure 2.3.2), while the specimen 6NA which has medium sectional confinements, experienced in-plane buckling as shown Figure 2.3.2b The location of buckled reinforcement of the specimen 6NA which was captured by backside camera is indicated with red dashed line on the face of the specimen in Figure 2.3.1c.

For non-anchored specimens, the damage also started after the appearance of the first shear crack at the critical zone but did not further spread along the wall length with the increase of negative loading. The flexural cracks appeared in the beam under the positive loading but was not as dominant as in anchored specimens. In summary, the non-anchored cases resulted in large cracks near the lower stab face under the negative loading cycle due to the absence of anchored reinforcing bars. This resulted in less strains in other parts of the wall during bending, resulting in lesser flexural cracking along the bottom of the wall. However, the anchored cases experienced dominant flexural cracks and concrete crushing under positive loading as a result of cracking along the wall length under the negative loadings.

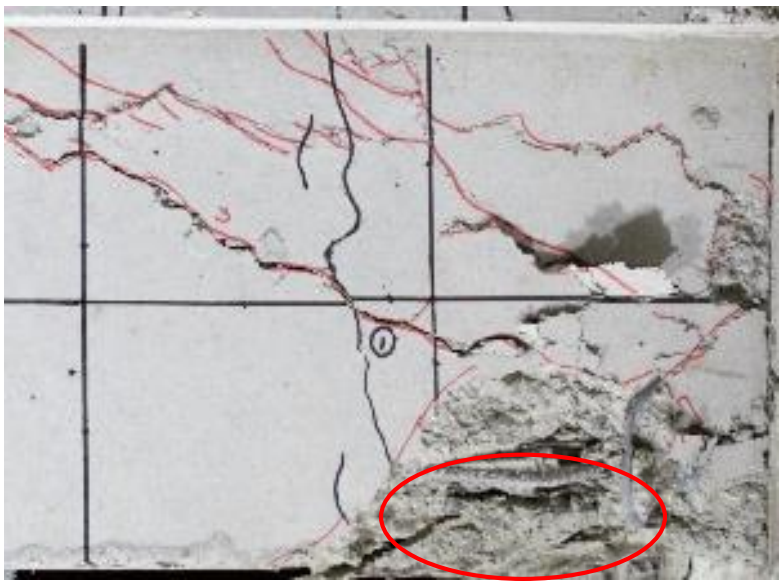

(a) Specimen 3NA

(b) specimen 6NA

Figure 2.3.2. Buckling of the longitudinal reinforcement in the anchored specimens

2.3.2 Load-Deflection Relation

To understand the impact of reinforcement detailing on the performance of a wall, a load-deflection curve for each specimen was plotted. Almost all specimens were tested under cyclic loading of up to +1/25 drift limit except 12HN. The specimen 12HN reached to the peak strength capacity at the drift of +1/10. Although it was designed to test up to −1/25, the last negative loading cycle was not considered owing to concrete crushing during the positive loading cycle before the negative loading cycle.

In the first place, non-anchored specimens showed higher deformability compared to the anchored specimens, while the anchored specimens without boundary confinement showed higher strength capacity in the minimum reinforcement case. The higher strength capacity of the anchored specimen was due to the earlier yielding of the anchored bars under the tensile loads, whereas the non-anchored steel bars only yielded under the compression load near the maximum step. This means that the anchored reinforcements of the wall boundary carried both positive and negative loads unlike the non-anchored reinforcement that carried only compression load. In addition, the anchored bars of the wall boundary which were fixed on both ends, incurred buckling under the positive loading (see Figure 2.3.2) whereas the non-anchored detailing, which was only fixed on one end, did not undergo buckling.

The strength and drift capacity can be seen in load-deflection curves of the specimens 3NN and 3NA which are having minimum reinforcements. It was observed that the anchored reinforcements of the specimen 3NA carried load during positive and negative loading but non-anchored reinforcements of the specimen 3NN only resisted compressive loads. It is therefore the wall boundary longitudinal reinforcement of the specimens 3NN and 3NA yielded in the different loading direction as shown with the diamond and circle marks in Figure 2.3.3 and Figure 2.3.4.

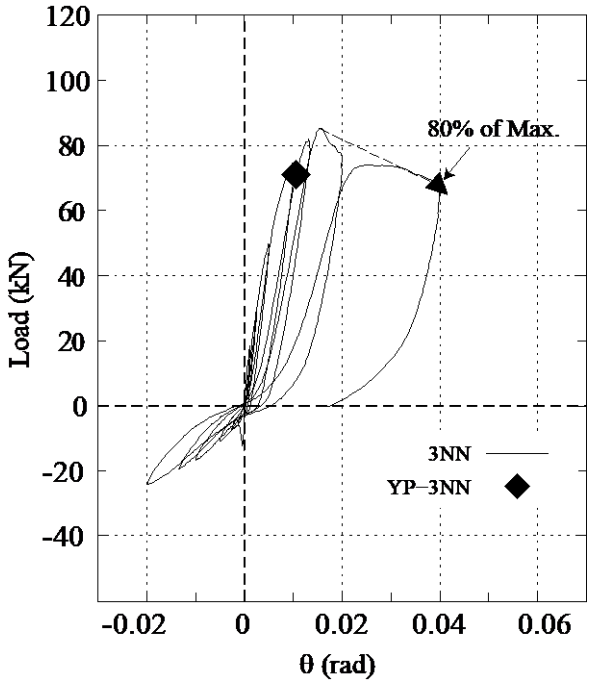

Figure 2.3.3. Load-Deflection curve of specimen3NN

The diamond mark shows the yield point (YP) of the wall boundary reinforcement of non-anchored detailing, and the circle represents the YP of the anchored detailing of the similar reinforcement. The activity of anchored bar under the positive and negative loads avoided concrete damage in the early steps and conferred higher strength to the specimen. However, the result could be different with having more transverse reinforcements which also confine the concrete. The amount of transverse reinforcement in the specimen 3NN and 3NA was found insufficient to confer higher drift and strength capacity to the hanging wall considering both types of reinforcement detailing.

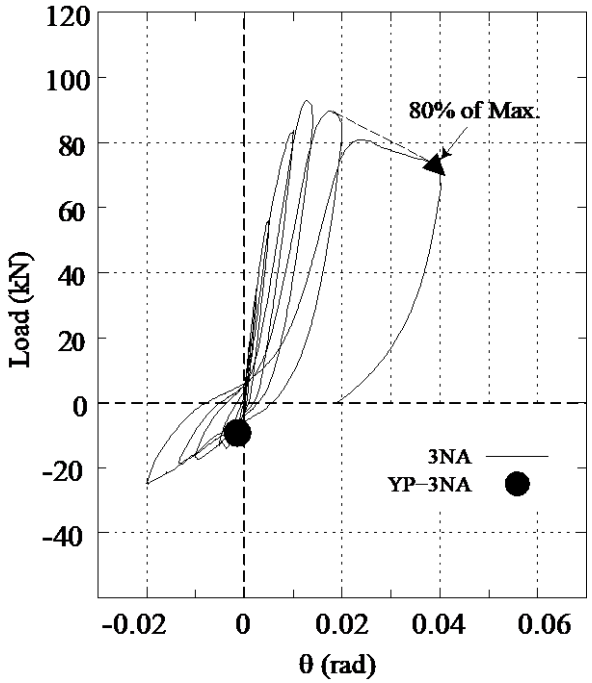

Figure 2.3.4. Load-Deflection curve of specimen 3NA

The influence of transverse and confinement reinforcing along with detailing can be observed by comparing the results from 6NA, 12NA, and 12HN. The anchored reinforcements of hanging wall in the specimens 6NA and 12NA resisted the negative as well as positive loadings and yielded in the negative loading cycle as shown in Figure 2.3.5 and Figure 2.3.6 but the 12HN yielded under positive loading Figure 2.3.7.

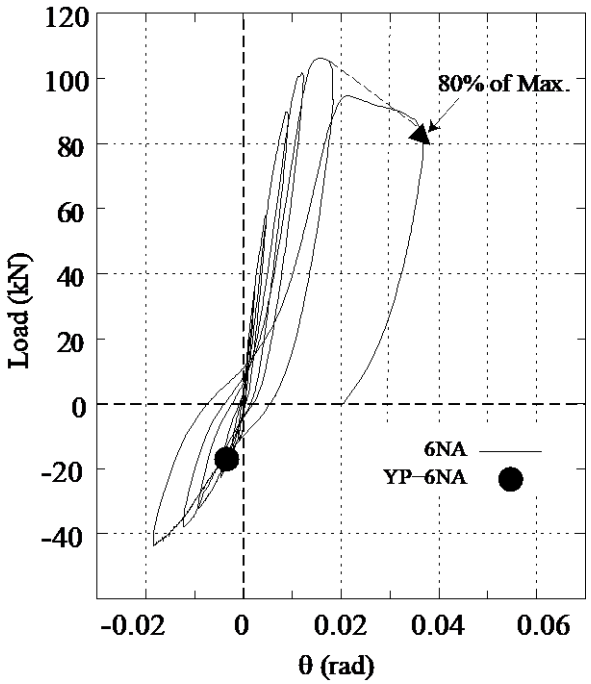

Figure 2.3.5. Load-Deflection curve of specimen 6NA

The specimen 12NA, which had a similar longitudinal reinforcement to 6NA, had a higher strength than the latter because of having a larger quantity of transverse bars.

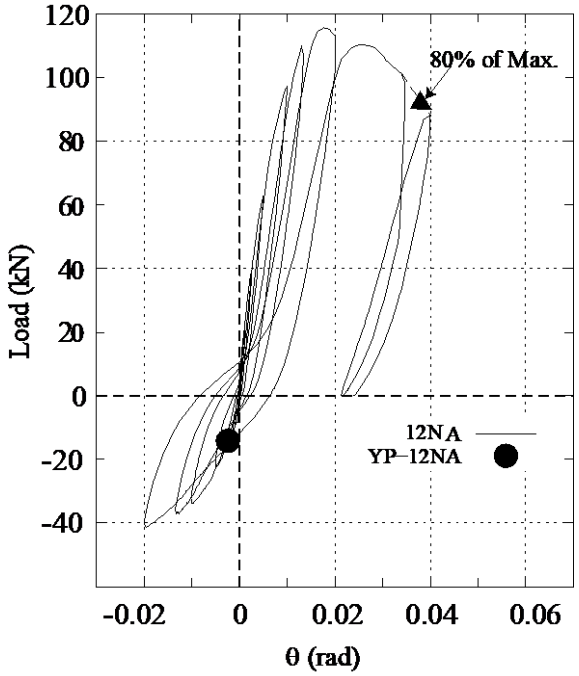

Figure 2.3.6. Load-Deflection curve of specimen 12NA

The presence of boundary confinement and non-anchored detailing conferred the highest strength to the specimen 12HN compared to other specimens shown in Figure 2.3.7.

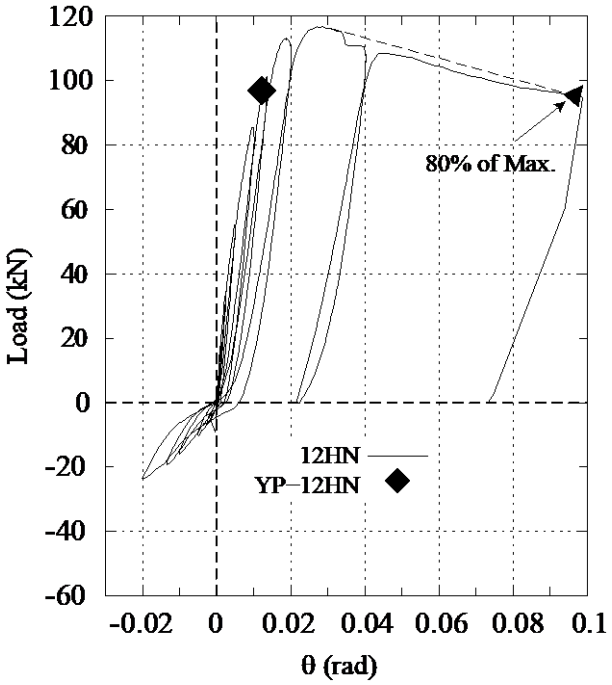

Figure 2.3.7. Load-Deflection curve of specimen 12HN

The boundary confinement reinforcing confined the concrete core of specimen 12HN better than sectional confinement, while the non-anchored detailing decreased the bonding stress resulting from load carrying capability of the non-anchored longitudinal bars. The better workability of the confinement reinforcing, and non-anchorage of the longitudinal bars increased the compressive strength of concrete which results in the higher capability of the wall.

Comparing the performance of 18NNT with 12NA and 12HN indicates that a slender element would result in a lower peak strength capacity, although having higher quantity of transverse reinforcement and non-anchored detailing as shown in Figure 2.3.8.

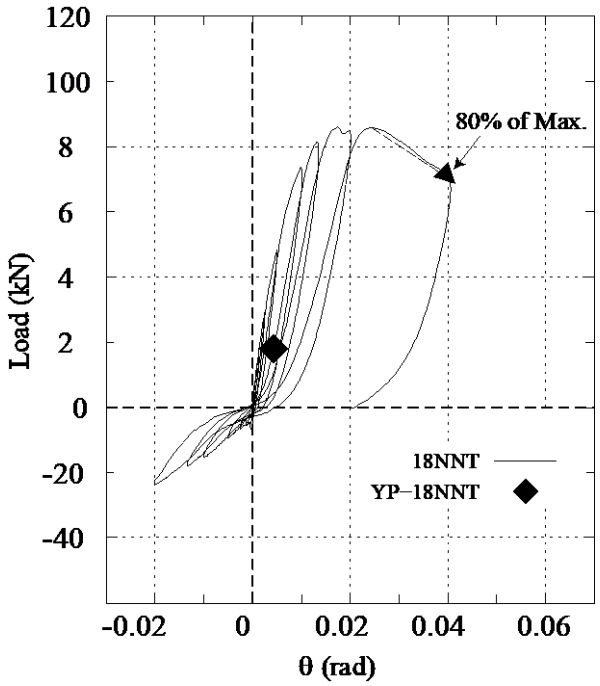

Figure 2.3.8. Load-Deflection curve of specimen 18NNT

The AIJ standard for lateral load-carrying capacity declares the impact of slenderness regarding ratio of the beam thickness to wall thickness as well as beam depth to wall depth (AIJ, 2016). The higher ratio of the beam to wall in terms of thickness and depth confer higher deformability to the beam member while the lower ratio increases the inflexibility. Nevertheless, the specimen 18NNT having higher ratio of the beam to wall thickness, did not experience higher drift than others. Because the decrease of wall thickness decreased the concrete compression area during positive loading and harmed establishing deemed interaction between concrete, transverse reinforcement and non-anchored detailing. Likewise, the neutral axis depth of the specimen 18NNT increased (see Table 2.4.2) resulting in a smaller lever arm between the tension bars and the neutral axis, and thus decreasing strength capacity.

2.3.3 Drift Capacity

As seen in the load-deflection curve of all specimens in sec (2.3.2), strength capacity reaches to the maximum point and then degrades at different rates for each specimen. Thus, it can be inferred that the lateral drift capacity of each specimen was different. In this study, the lateral drift capacity of the specimens is defined based on the trend line of stiffness degradation at the point corresponding to 80% of the maximum strength capacity, as dominated with triangular mark on the load-deflection curve of every specimen in sec (2.3.2).

Accordingly, stiffness degradation was calculated at the descending phase of the skeleton curve of the specimen between the active loading step of the preceding cycle and maximum loading step of the succeeding cycle. The drift capacity was nearly equal in all other specimens except 12HN. The filled marks in Figure 2.3.9 represent the drift capacity of anchored detailing specimens and unfilled marks denote the drift capacity of non-anchored detailing specimens.

The transverse reinforcement did not affect the drift capacity of the anchored specimen as it affected the non-anchored specimens. It was observed that transverse reinforcement was not effective for those anchored specimens that had an equivalent or a larger amount of longitudinal reinforcement compared to the transverse reinforcement (specimens 12NA and 3NA).

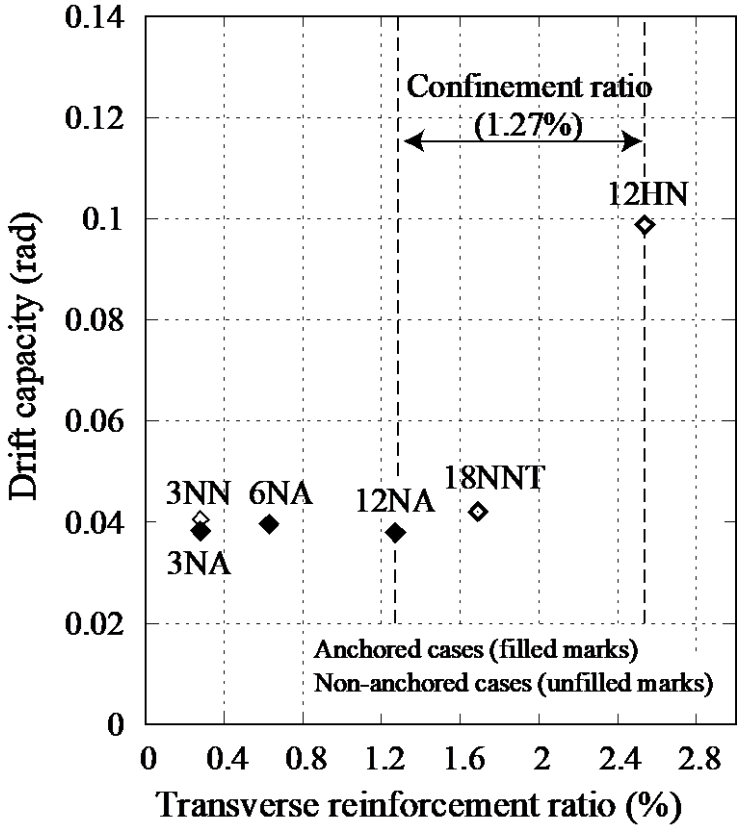

Figure 2.3.9. Drift capacity comparison at 80% of maximum loading

As seen in Figure 2.3.9, between 6NA and 12NA, even if the amount of transverse reinforcement of 12NA was larger than that of 6NA, with equal amount of longitudinal reinforcement, the drift capacity of 12NA was not larger than that of 6NA. This shows that anchored detailing affects drift capacity and it may cause damage to the concrete due to the bonding and flexural cracks. The cracks were appeared as a result of the cyclic tension-and-compression behavior of the anchored longitudinal reinforcement despite having enough quantity of sectional confinements.

As seen in 12HN, the drift capacity was higher than the other specimens due to having boundary confinement and non-anchored detailing. The non-anchored detailing did not cause flexural cracks and large bond stress interactions between the steel and concrete; a better concrete condition is maintained during the cyclic loading owing to a higher efficiency of the boundary confinements than sectional confinements. However, the impact of non-anchored detailing associated with the slenderness was found insignificant to the drift capacity of the specimen. Finally, considering the small difference in drift between 3NA and 3NN, it is concluded that a wall with higher drift capacity can be established where:

- There is a non-anchored detailing of longitudinal reinforcement;
- The amount of longitudinal reinforcement is equal or greater than transverse reinforcement;
- The confinements are placed at the critical zone of the wall.

2.3.4 4.4. Strain–Drift Relationship of Transverse reinforcements

The impact of transverse reinforcement on the behavior of a hanging wall is proportional to the type of stirrups and their location. Transverse reinforcements are more influential when limited to the critical zone of the specimen, according to the displacement-based design approach (Moehle, et al., 2010 and Wallace, et al., 2002). To demonstrate this, the drift-tensile strain curves of specimens for the critical stirrups are plotted in Figure 2.3.10 based on the strain gauge records. The data used for comparison of the strain–drift relation of specimens 12HN, 12NA, 3NN, and 3NA were taken from the record of the strain gauges installed in both in and out of plane loading, as shown in Figure 2.2.6 to Figure 2.2.9.

The first stirrup of specimen 3NN, corresponding to strain gauge H_1 as shown in Figure 2.3.10a, encounters a bigger amount of strain in the negative loading due to the accumulation of cracks near the lower stab rather than spreading along the length of the wall as seen in Figure 2.3.10a. Conversely, specimen 3NA experienced a lower strain in the negative loading, because the cracks spread along the length of the hanging wall, as shown in Figure 2.3.10b. As seen in Figure 2.3.10d, boundary confined bars were more operational for carrying tensile and compressive loads rather than sectional confinements, which address the condition of the displacement design approach. Similarly, the performance of sectional confinement stirrup of

specimen 12NA and boundary confinement of specimen 12HN were almost alike as shown in Figure 2.3.10c and 9d. This is because the anchored bars of specimen 12NA could transfer more stress to the stirrup during the loading, resulting in the stirrup experiencing similar strain as the 12HN confined stirrup.

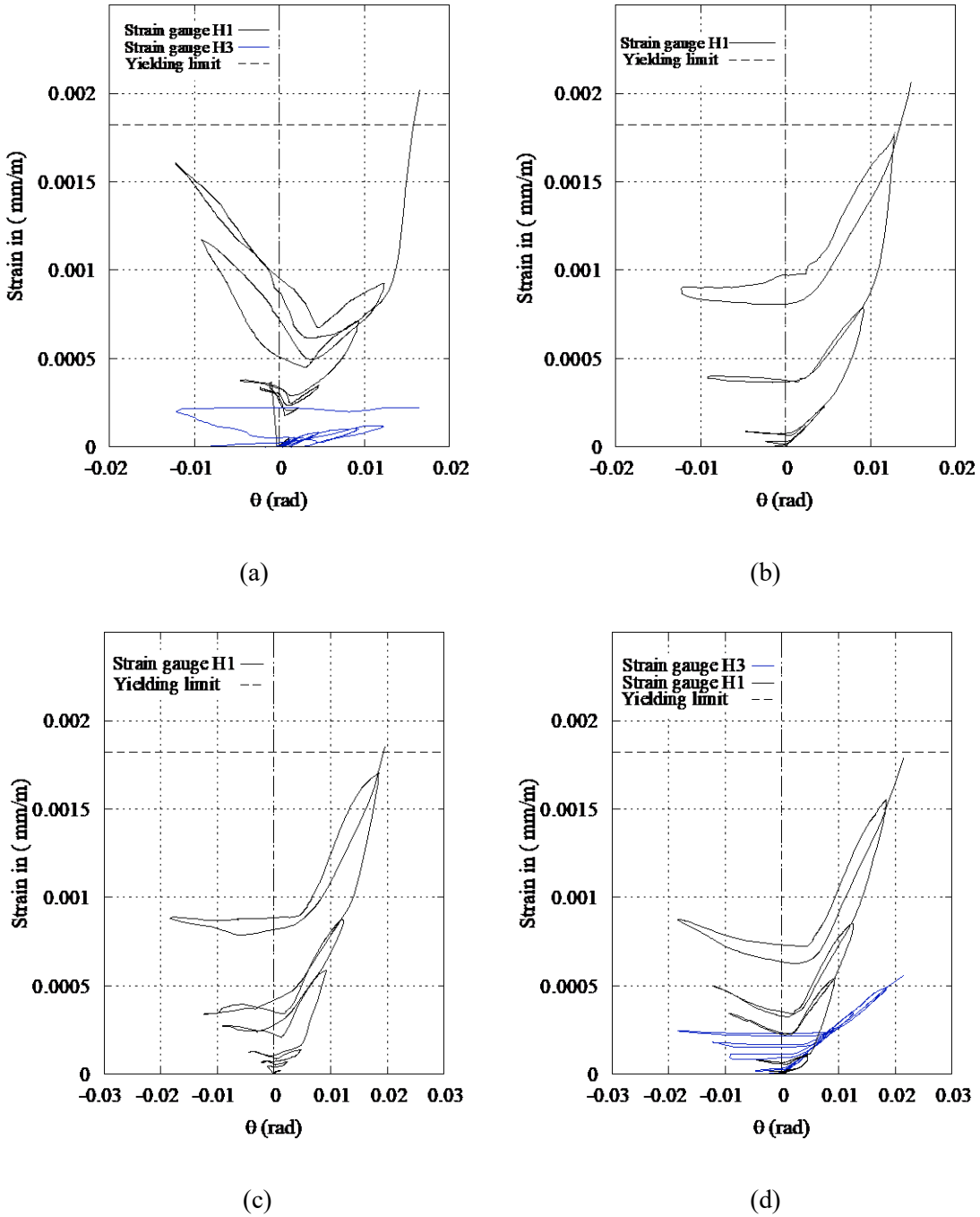

Figure 2.3.10. Strain–drift relation of the critical transverse reinforcement: (a) 3NN; (b) 3NA; (c) 12NA; (d) 12HN

2.4 Evaluation of the Experimental Results

2.4.1 Evaluation of the Strength

Experimental approaches for observation of an unknown effect, need verification by either an analytical or numerical model. For this reason, the result of experimental test was comparatively evaluated with the analytical result.

For anlaysis purpose a numerical software (Response-2000) which is able to accomplish reinforced concrete sectional analysis, was used (Bentz, et al., 2001). Response-2000 is a sectional analysis program that calculate the strength and ductility of a reinforced concrete cross-section subjected to shear, moment, and axial load. All three loads are considered simultaneously to find the full load-deformation response using the latest research based on the modified compression field theory.

All specimen sections were modeled in Response-2000 based on their detailed material property obtained from the experimental testing results. The concrete stress-strain curve was assumed based on the non-linear model of (Popovics,1973) and the steel stress-strain relation was developed according to the modified input data as shown in Figure 2.4.1.

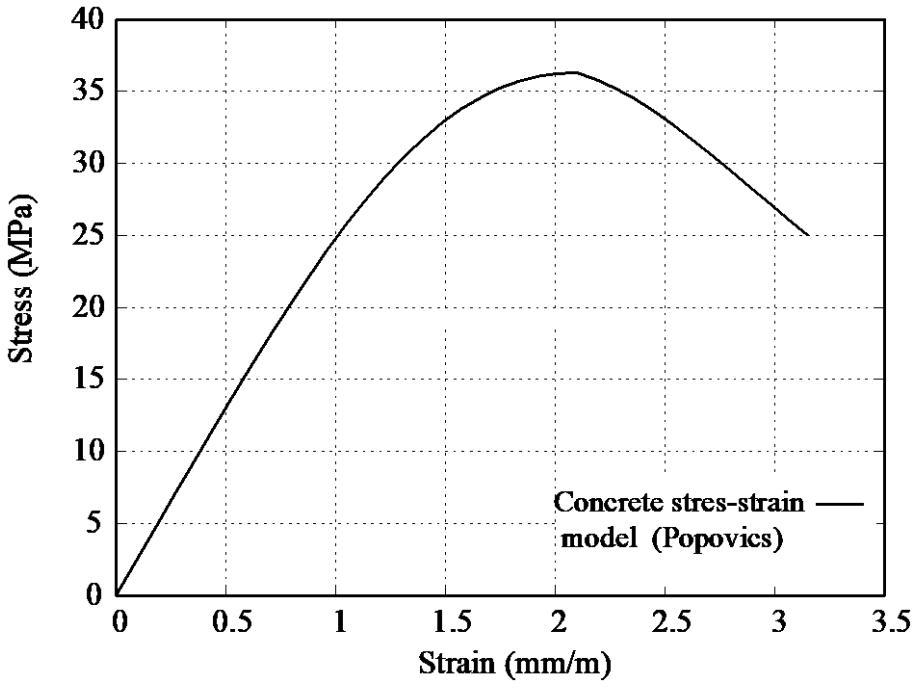

(a) Concrete model

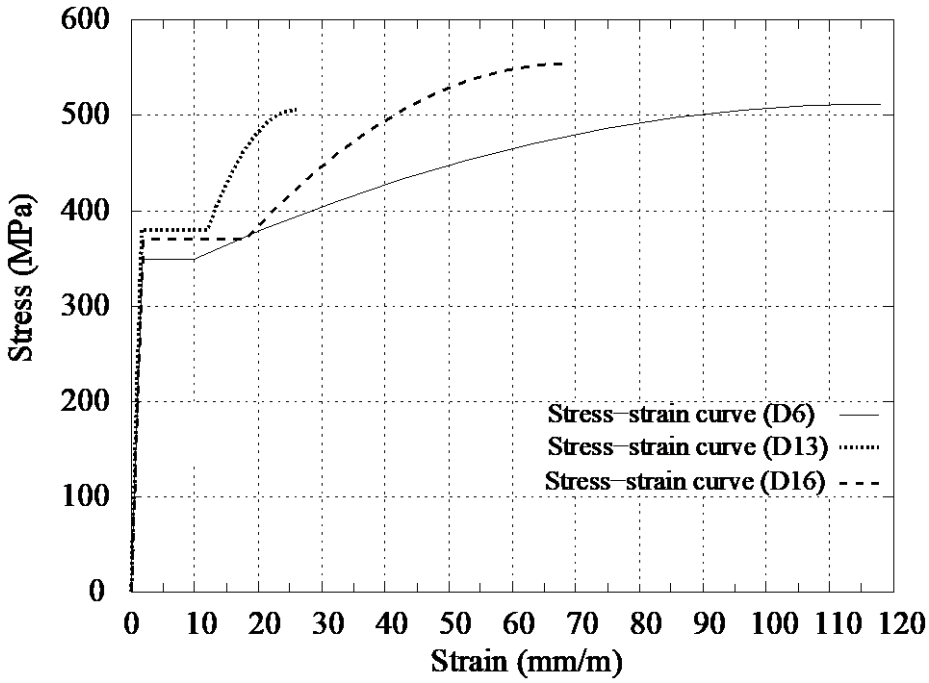

(b) reinforcements model

Figure 2.4.1. Model of stress-strain curve for analysis.

Table 2.4.1. Ultimate strength capacity

Specimen	Ultimate strength capacity Vexp [1] (kN)	Analytical prediction Vana[2] (kN)	Vexp /Vana (%)
3NN	85.2	101.8	84
3NA	92.8	104.9	88
6NA	106.2	110.5	96
12NA	115.8	110.5	105
12HN	116.8	101.8	115
18NNT	86.2	80.4	107

[1] Experimental ultimate lateral load capacity

[2] Analytical ultimate lateral load capacity

The analytical strength capacity of the specimen was identified using the principle of ineffectiveness of transverse and non-anchored reinforcements. Therefore, the analytical strength capacity of specimens 3NN, 12HN; and 6NA, 12NA were found to be alike as seen in Table 2.4.1.

Specifically, analytical prediction tends to overestimate the strength capacity of specimens with minimum reinforcement, whereas it underestimates the strength capacity of the specimens with a higher amount of transverse reinforcement. The analytical strength capacity of the specimens was obtained using Response-2000, which is a monotonic loading software. The experimental strength obtained from a cyclic loading test which can affect the strength capacity, especially in anchored cases. Considering this, the differences of the analytical and experimental strength might be due to differences of the loading type and the abandonment of non-anchored and transverse reinforcements in the analysis. The relation between the total amount of transverse reinforcement ratio *R*, which includes both sectional and confinements reinforcement, versus shear strength ratio for all specimens is shown in Figure 2.4.2. The sectional analysis prediction appears to be satisfactory for specimen 6NA with a medium amount of reinforcement, which showed only 4% of underestimation from the analytical result.

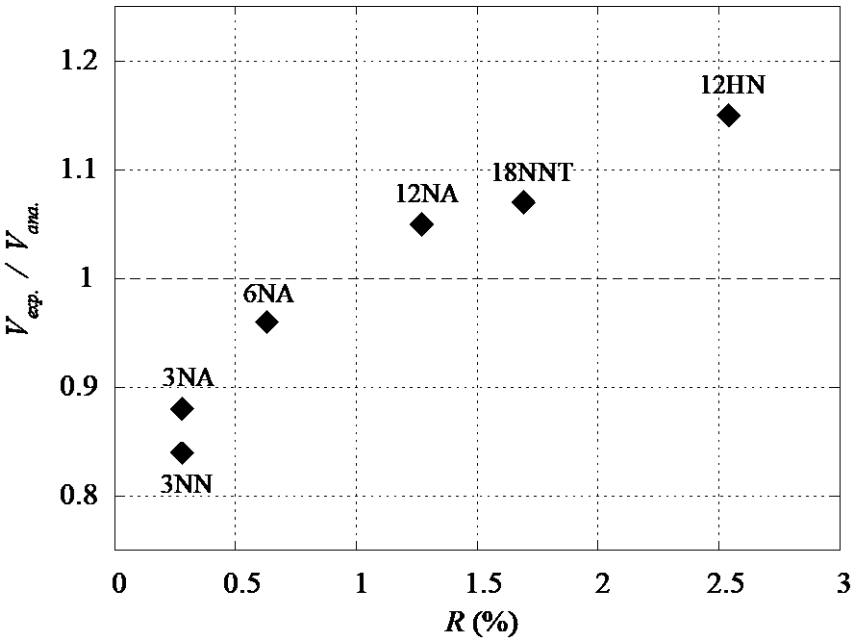

Figure 2.4.2. Analytical and experimental comparison

2.4.2 Evaluation of the confinement and reinforcement detailing impact

The strength variation of specimens, specifically the specimen with similar longitudinal reinforcement was realized owing to the different amount of transverse reinforcement, different detailing, and slenderness. In fact, the reinforcement detailing and confinements established different workability of the reinforcements with the concrete in every specimen and resulted in the specimens to have different capability. The influence of transverse reinforcements along with

detailing of the longitudinal bars, is evaluated in the peak observed strength, to ascertain a method of detailing that confers higher capability to the hanging walls. To evaluate confinement impact on the strength and drift capacity, the non-linear behavior of the concrete compression zone was observed in the maximum positive loading. The concrete compressive stress and strain at the peak strength of the specimens were obtained from the experimental result assuming that the plane section remains plane. The compressive stress and strain were found using following steps:

- To calculate internal forces, stress incurred in every longitudinal reinforcement was calculated based on the strain gauge record pasted on the longitudinal reinforcement. The strain records from gauges V1, V5, L1, and L2 were used for stress analysis of specimens 3NN and 3NA, and the strain records from V1, V6, V9, L1, and L2 were used for the other specimens.
- The concrete compressive force Ncc was extrapolated using the equilibrium Equation 1.

$$N_{CC} = \sum N_T - \sum N_{CS} \tag{2.4.1}$$

Where

N_T: (N_1, N_2) is the tensile forces resulting from bending behavior of the specimen as shown in Figure 2.4.3.

N_{cs}: is the compression forces resulting from bending behavior of the specimen as shown in Figure 2.4.3.

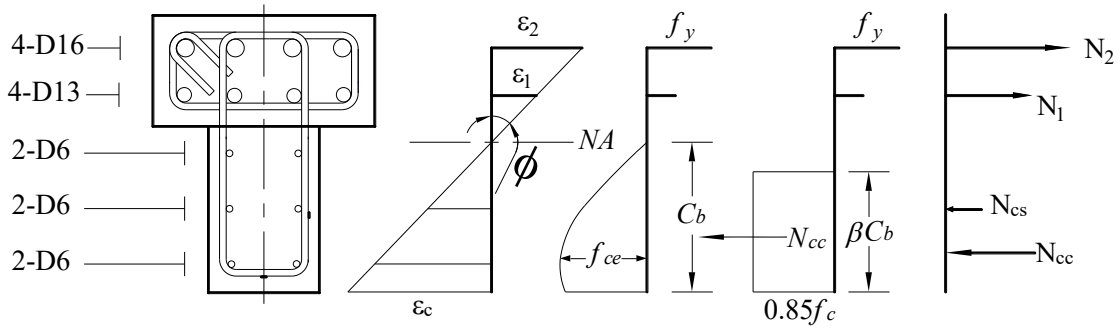

Figure 2.4.3. Stress-strain diagram of the specimen

- Neutral axis C_b was calculated using the curvature ϕ of the specimen. Curvature was calculated according to the strain gauge records L1 and L2 (ε_1, ε_2) installed on the D13 and D16 reinforcement bars (See Experimental Study section). Using neutral axis and curvature, the compressive strain at the extreme compression fiber was calculated.
- Effective concrete compressive stress f_{ce} and compressive strain ε_{cu} was found using equations 2 and 3:

$$f_{ce} = \frac{N_{cc}}{0.85 \times \beta C_b \times d} \tag{2.4.2}$$

$$\varepsilon_{cu} = \phi \times C_b \tag{2.4.3}$$

The value of curvature ϕ seems practical until yielding of the D16; however, its value suddenly increased after yielding of D16 near maximum loading. The sudden increase of curvature was observed due to the occurrence of the larger strain in the D16 following yielding; and the compression failure of concrete compressive fiber (see Figure 2.3.2). Moreover, the stress distribution at the lower moment could be almost linear which establishes a triangular concrete stress block. Post-yielding, the stress distribution within the concrete would change to that shown in Figure 2.4.3. This change in mechanism could have resulted in the sudden change in curvature. The sudden increase of the curvature near the maximum loading steps was observed in specimen 12HN which resulted in a larger compressive strain and neutral axis, and relatively lower effective compressive strength.

In summary, the concrete compressive strength and strain of the specimen 12HN were increased by installation of boundary confinements and non-anchored detailing of wall longitudinal reinforcement. However, a certain effective compressive strength and strain was not modified due to the sudden increase in the curvature. Therefore, the experimental effective strength and ultimate strain for all other specimens are shown with filled marks in Figure 2.4.4, except for 12HN. The stress-strain relationship of 12HN is shown with trend point lines, to express the strength-strain relation at the peak observed loading as well as in five earlier steps. However; for the sake of comparison with the compressive stress-strain of other specimens, nearly the middle value (third point from the top) of trend point line can be described as the ultimate compressive stress-strain of the specimen 12HN.

The effective concrete compressive strength of 12HN, 12NA, and 18NNT were larger than the other examined specimens due to the different stress transition mechanisms and larger amount of transverse reinforcement.

As shown in Table 2.4.2, the medium value of specimen 12HN exhibits higher effective compressive strength and strain than other specimens due to its non-anchored detailing and confinements. This means that a better workability was established between the concrete, the confinements, and the longitudinal bars in case of non-anchored detailing.

The effective strength in specimen 6NA was the same as that of 3NA and 3NN, while the strain is larger than all anchored specimens, because, the longitudinal bar of 6NA underwent out of plane buckling (see Figure 2.3.2b). which might have triggered amplification of the strain.

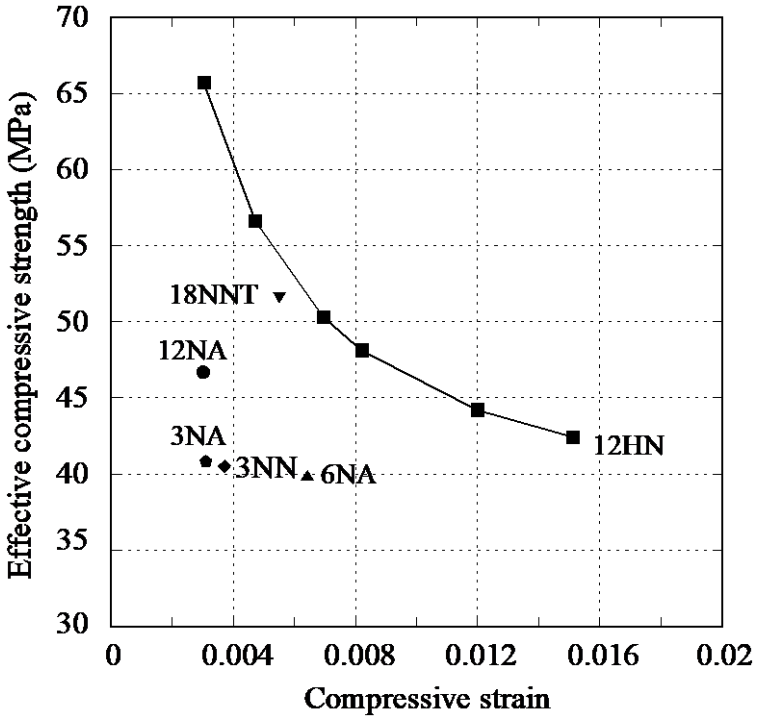

Figure 2.4.4. Comparison of effective compressive strength and maximum compressive strain

Table 2.4.2. Test result parameters

Specimen	Drift capacity (%)	Neutral axis depth (mm)	Effective compressive strength (MPa)	Ultimate compressive strain
3NN	0.040	144	40.8	0.0031
3NA	0.038	150	40.5	0.0037
6NA	0.040	161	39.8	0.0064
12NA	0.037	134	48.3	0.0033
12HN	0.099	148	50.3	0.0069
18NNT	0.040	161	51.7	0.0055

2.4.3 Evaluation of the Stress transition mechanism

It was observed that different stress transition mechanism in the anchored and non-anchored detailing bars results in different capability of the hanging wall. The non-anchored detailing reinforcement only carries compressive axial load, creating a much lower bond stress in the longitudinal reinforcement compared to the anchored one, as shown in Figure 2.4.5. The anchored reinforcement carries tensile and compressive forces during cyclic loading resulting in a higher bonding stress with the concrete. The reduction of bond stress in a non-anchored longitudinal reinforcement renders the confinements to be more effective on confining the core concrete. Conversely, the higher bond stress in the anchored detailing as well as higher interaction of the concrete-steel result in damaging the concrete core and affect the capability of the hanging wall. With all that considered, if higher amount of transverse reinforcement is utilized with the anchored detailing reinforcements, it may confine the concrete core and improves the strength capacity but does not improve the drift capacity.

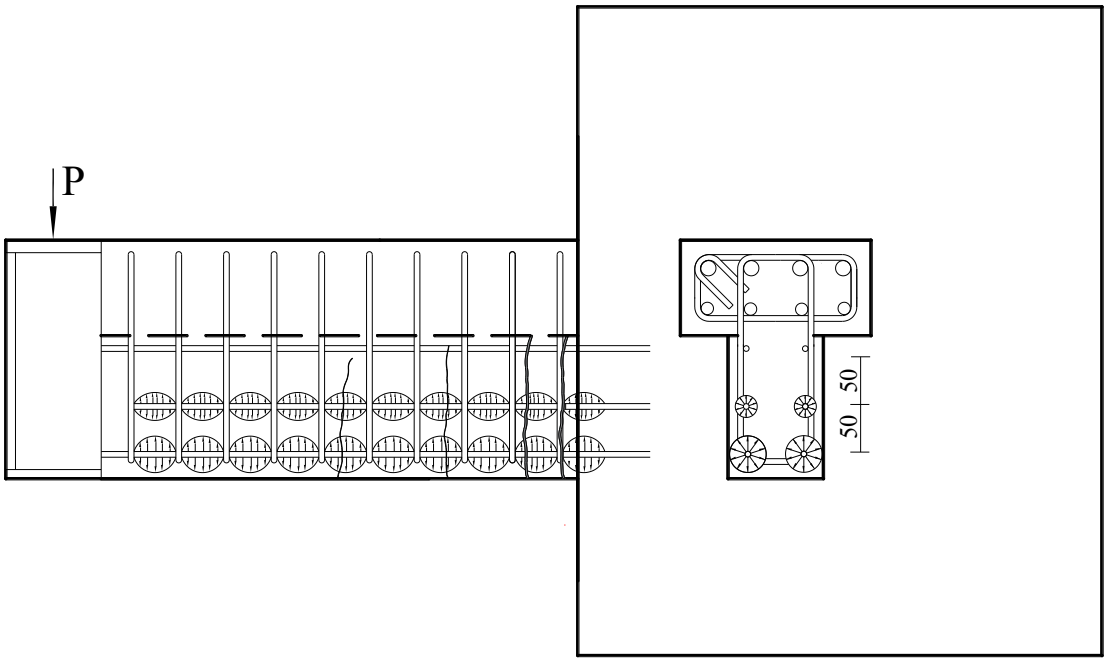

(a) Anchored specimen

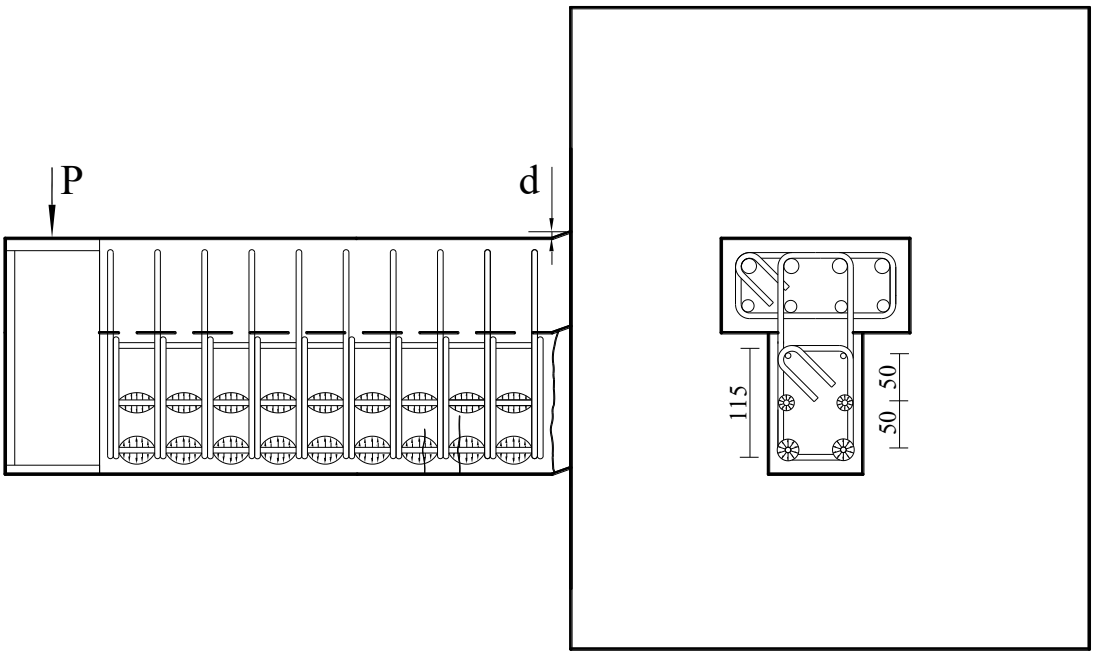

(b) Non-anchored specimen

Figure 2.4.5. Mechanism of confinement and detailing impacts on the concrete core

2.5 Summary

This chapter is aimed to assess the influence of different reinforcement detailing and transverse reinforcement on the strength and drift capacity of the non-structural wall, to develop walls with higher capability. It was observed that non-anchorage of the wall longitudinal bar significantly increases the drift capacity of the wall and limiting damage. The significant increase of drift capacity of the non-structural wall can be established where:

- There is a non-anchored detailing of longitudinal reinforcement;
- The amount of longitudinal reinforcement is equal or greater than transverse reinforcement;
- The confinements are placed at the critical zone of the wall.

Transverse reinforcement in terms of boundary confinements was more influential when limited to the critical zone. It could better confine the core concrete of the wall and led the specimen to have higher effective compressive stress and strain. The workability of the confinements and non-anchored detailing was found effective and resulted in the specimen 12HN to have higher strength and drift capacity. The strength capacity of the anchored detailing specimens with minimum amount of reinforcements was higher than that of the non-anchored specimen.

The slenderness of the non-anchored detailing specimen did not significantly impact the drift capacity despite of having higher quantity of transverse reinforcement it also decreased the

strength of hanging wall. The decrease of wall thickness decreased the concrete compression area and damaged establishing expected interaction between concrete, transverse reinforcement and non-anchored detailing.

The impact of boundary confinement on the longitudinal reinforcement under flexural load was higher in the non-anchored case compared to anchored detailing due to different load carrying capacity of the longitudinal reinforcement.

The observed indications of this research can be developed for the normal shear wall considering workability of the special boundary confinements and detailing of longitudinal reinforcements.

Chapter III

Evaluation of Analytical Models of Confined Concrete using Experimental Data

3.1 Introduction

It is emphasized in Chapter II that the non-anchored detailing establishes a better workability with the boundary confinement and increase capability of the member. Given this point, it is necessary to verify the better workability using different analytical models focusing on the confinement impact on the concrete compressive strength and strain.

As a common practice, strength of RC member's constituents modifies the design strength of the member and they are considered for the design purpose separately. Notably, the strength of RC element equals to the strength of reinforcements and the strength of concrete regardless of their interactive effectiveness. In fact, the strength of RC element synthesizes not only from strength of its constituents but also additional strength resulting from interactive effectiveness.

Reinforcement bars in a concrete element inducing inclination of the concrete strength capacity along with their discretion of carrying tensile forces. Nevertheless, the reinforcements sometime degrade bearing stress of supporting concrete along the bar, which results in the reduced axial effectiveness of reinforcing bar. Considering these interactions of the concrete and reinforcement, it can be inferred that the models demonstrate the strength capacity of a RC element that not only focusing on the strength of constituent but also considering the interactive effect of the reinforcements as well.

Transverse reinforcement resist shear stress, align the longitudinal reinforcement, prevent longitudinal reinforcement from buckling, reducing the spalling of concrete cover and confining the concrete. In principle, at low levels of stress, transverse reinforcement faces a less stress; the confinement hardly affects the concrete and the concrete behaves much like a plain concrete. At the higher level of stresses close complying with the uniaxial crushing strength of concrete, high lateral tensile strains develop as a result of the formation and propagation of longitudinal micro cracks. Transverse reinforcement in conjunction with longitudinal reinforcement acts to restrain

the lateral expansion of the concrete, enabling higher compression stresses and more important, much higher compression strains to be sustained by the compression zone before failure occurs (Pauly, et al., 1992; and Priestley, et al., 2003).

Results of an experimental test showed an increase up to 300 % in concrete strain for beams having confinement on the compression zone than beams without confinement. The increase also occurred in the load capacity and the curvature of beams with confinement, while the moment capacity did not show significant improvement (Yulita, et al., 2014).

A suitable placement of the transverse reinforcement confines concrete which results in a significant increase of the strength and ductility of concrete. The impact of confining transverse reinforcement on the concrete can be investigated using appropriate analytical stress–strain models that represent the real behavior.

There are different models which were developed in the paste and aimed to capture the non-linear behavior of the concrete as well as identify how the transverse reinforcement effects concrete capability. Most design-oriented models follow Equation (3.1.1), which was recommended by Richart et al., (1928) to predict the ultimate strength $f_{cc}^{'}$ of confined concrete based on confining pressure:

$$f_{cc}^{'} = f_{co}^{'} + K_1 f_{le} \tag{3.1.1}$$

This Equation represents the relationship between confinement ratio (fle/fco`) and confinement efficiency ($f_{cc}^{'}/f_{co}^{'}$). Coefficient K_1 represents the gain of strength due to the confinement effect divided by the lateral confining pressure provided by the confinement material, as shown by Equation (3.1.2*)*.

$$K_1 = (f_{cc}^{'} - f_{co}^{'})/f_{le} \tag{3.1.2}$$

The existing models were developed throughout rigorous experimental and analytical researches; however, sometimes the modified models give different result for similar structural elements. The effectively confined concrete area proposed by Sheikh is based on the assumption that confinement pressure generated by the reinforced cage between each node is uniform (Sheikh, et al., 1982). This assumption is based on the premise that the rectangular column subjected to a compressive axial load is deformed to circular shape. However; it is observed in an experimental test that the model proposed by Sheikh consistently underestimated the strength of confined concrete after longitudinal strain of approximately 1% (Sato, et al. 2000).

Concrete confinement is a three-dimensional phenomenon that cannot be reduced to a sectional level. Therefore, it is essential to consider the variation of lateral pressure along the

member length. It should be noted that the pressure developed at a nodal point, where the longitudinal bar is supported by a lateral tie is distributed reasonably uniformly along the length of the longitudinal bar. This is because the longitudinal bar in compression (Richart, et al., 1992)

The aim of this study is to verify the impact of confinements on the concrete considering better workability of non-anchored reinforcement and confinement along with concrete. It is further aimed to ascertain accuracy of the existed analytical models for evaluation of the walls which is built according to the proposed detailing methods. The data of tested specimens as explained in section (2.2) are used for both confirming of the experimental result, and accuracy of the models. The experimental data is evaluated using (Hognested, et al.,1951; and Mander, et al., 1984) models for non-linear behavior of the concrete.

3.2 Concrete Model proposed by Hognestad (1951)

The Hognasted model is one of the modified models for capturing of the inelastic behavior of the concrete. The model is widely being used for modeling of concrete stress-strain distribution as shown in Figure 3.2.1. Accordingly, the stress-strain curve is a second-order parabola until the peak stress. The portion up to the peak of the curve (second degree parabola) is modified with Equation (4). After the maximum stress, the relation between stress and strain is linear. The stress reduces 15% comparing to $f_c^{'}$ when the strain reaches its ultimate value of 0.0038.

$$\sigma_c = f_c^{'}\left[\frac{2\varepsilon_c}{\varepsilon_{co}} - \left(\frac{\varepsilon_c}{\varepsilon_{co}}\right)^2\right] \tag{3.2.1}$$

$$\varepsilon_{co} = \frac{2f_c^{'}}{E_c} \tag{3.2.2}$$

Where

ε_c: is the compression strain of concrete

ε_{co}: is the compression strain of confined concrete at the maximum stress.

$f_c^{'}$: is the maximum stress reached in concrete which may differ from the cylinder strength.

E_c: is the modulus of elasticity.

The recorded data of conducted experimental test for specimens 6NA, 12NA, and 12HN (see Sections 2.2.3 to 2.2.5) , is analytically evaluated using the Hognestad model. These specimens are similar in terms of quantity of longitudinal reinforcement but differs in terms of confinement reinforcement and detailing of the longitudinal reinforcement.

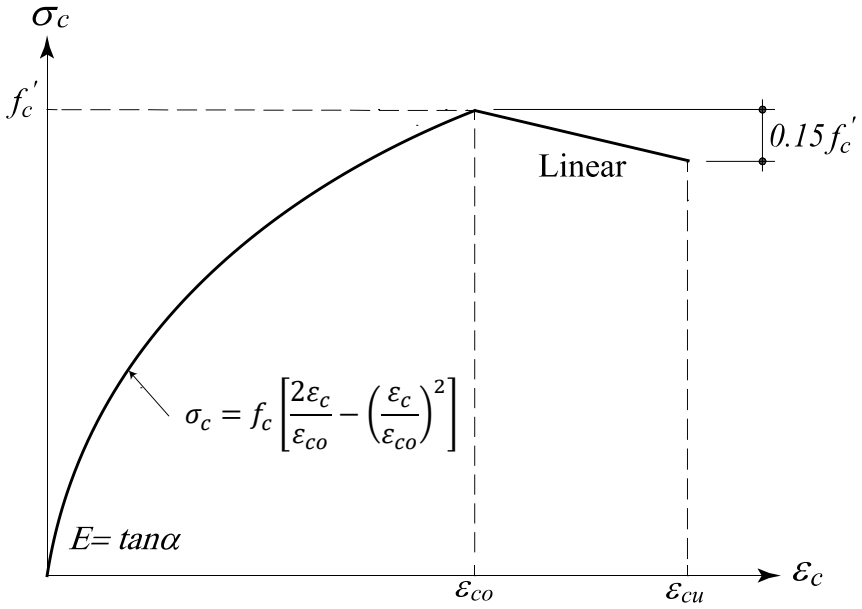

Figure 3.2.1. Hongnested Model (1951)

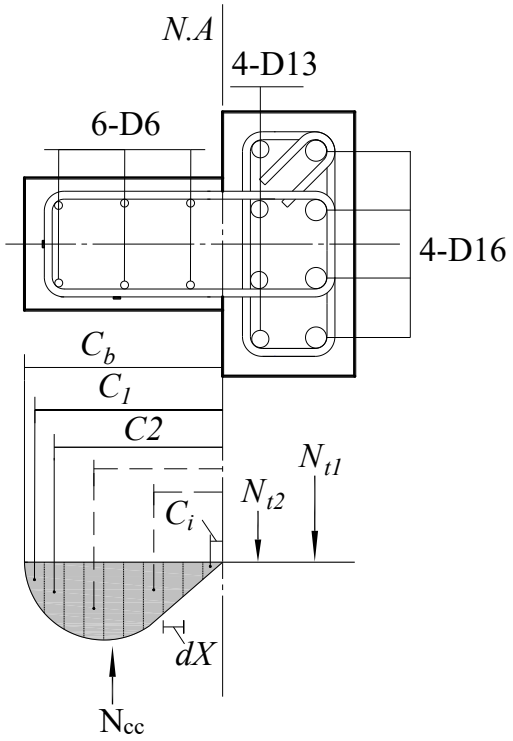

Figure 3.2.2. Stress distribution and geometry of the dividend concrete zone to the small fibers

The fiber analysis is used to evaluate capability of the specimens in terms of moment-curvature curve. Developing of the moment-curvature curve is possible while the compressive strength of confined concrete is known during the cyclic loading. Given that, the intended

compression zone of the specimen is divided to small fibers as shown in Figure 3.2.2 , in order to find compressive strength of the concrete which is confined by stirrups

Carrying stress by every small fiber is obtained by the model of Hognestad using an iterative process to adjust the depth of neutral axis. The neutral axis along with curvature provides obtaining the moment of the specimen according to an arbitrary value of the curvature. To provide details for the moment of the specimen assuming neutral axis depth C_b as an iterative variable and curvature as a given value, following equations are formulated:

$$M_n = M_c + M_{st} \tag{3.2.3}$$

$$M_n = N_{t1} \times d_{t1} + N_{t2} \times d_{t2} + \sum_{i=1}^{n} (N_{cci} \times d_i) \tag{3.2.4}$$

Where

M_n: is the nominal moment capacity of the specimens

M_c: is the moment carried by the concrete compression zone.

M_{st}: is the moment carried by longitudinal reinforcement.

d_{t2}, d_{t2}: is the distance of tensile longitudinal bars from central axis of specimen.

N_{t1}, N_{t2}: is the tensile stress carried by the longitudinal reinforcements(D13, D16)

N_{cci}: is the compressive stress carried by the fiber number *i* of compression zone

d_i is the distance of fiber number *i* from neural axis.

n: is the divisor number of compression zone to small fibers.

All parameters in the Equation (3.2.4) which provides nominal moment capacity in the non-linear stat, can be obtained from specimens geometry and reinforcement specifications; however, the accurate calculation of N_{cci} considering the impact of confinements is carried out using the Hognasted model. Given this, the compression stress carried by the small fiber of the specimen can be formulated as following:

$$N_{cci} = D \times dx \times \sum_{i=1}^{n} \sigma_{cci} \tag{3.2.5}$$

$$\sigma_{cci} = f_c \left[\frac{2\varepsilon_{ci}}{\varepsilon_{co}} - \left(\frac{\varepsilon_{ci}}{\varepsilon_{co}} \right)^2 \right] \tag{3.2.6}$$

$$\varepsilon_{ci} = \varnothing_i \times C_i \tag{3.2.7}$$

Where

D: is depth of specimens which varies for the bema and wall portions.

dx: is the width of small fibers.

σ_{cci}: is the compressive strength of the fiber number *i* considering impact of confinement. .

ε_{ci}: is the compression strain of divided fiber *i.*

ε_{c0}: is taken to be 0.002 at the maximum stress.

$\emptyset_i$: is the curvature which can be given an arbitrary value to identify the correspondent value of nominal moment for plotting moment curvature curve.

C_i: is the distance of divided fiber *i* from neutral axis.

$$C_i = C_b - i \times dx \tag{3.2.8}$$

The value of the neutral axis C_b is iterated until the following Equation is satisfied:

$$N_{t1} + N_{t2} + \sum_{i=1}^{n} N_{cci} - P_n = 0 \tag{3.2.9}$$

P_n: is the nominal axial stress acting on the specimen.

The fiber analysis method is concisely explained with a flow chart shown in Figure 3.2.3. Accordingly, the analytical moment curvature curve of the specimen is obtained using Hognasted model. For the sake of comparison, the obtained moment-curvature curve is further developed to get a monolithic load-deflection curve. For this purpose, the plastic hinge length is assumed equal to the full depth of the specimen (250 mm) according to the result of first experimental test (See section 4.4.1). The monolithic load-deflection curve of the specimens is compared with the experimental based hysteretic curves of specimens 6NA, 12NA and 12HN as shown in Figure 3.2.4.

The model proposed by the Hognasted underestimates the drift capacity of the confined concrete after lateral drift of 0.5%. however; the predicted strength capacity of specimens based on the model is nearly complying with the experimental result with a scarce overestimation comparing to the specimen 6NA.

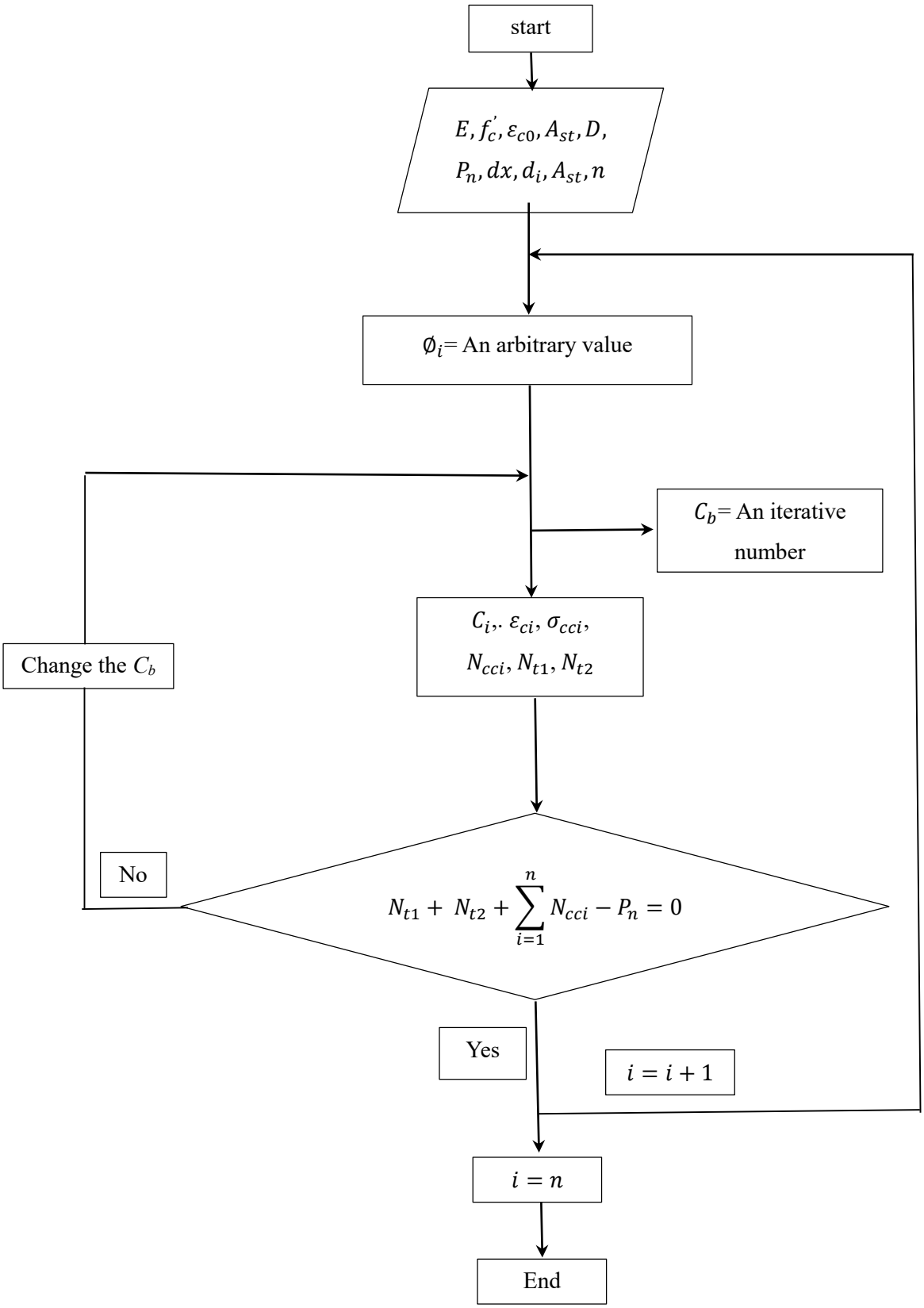

Figure 3.2.3. Procedure of the fiber analysis of the reinforced concrete element using Hognasted model.

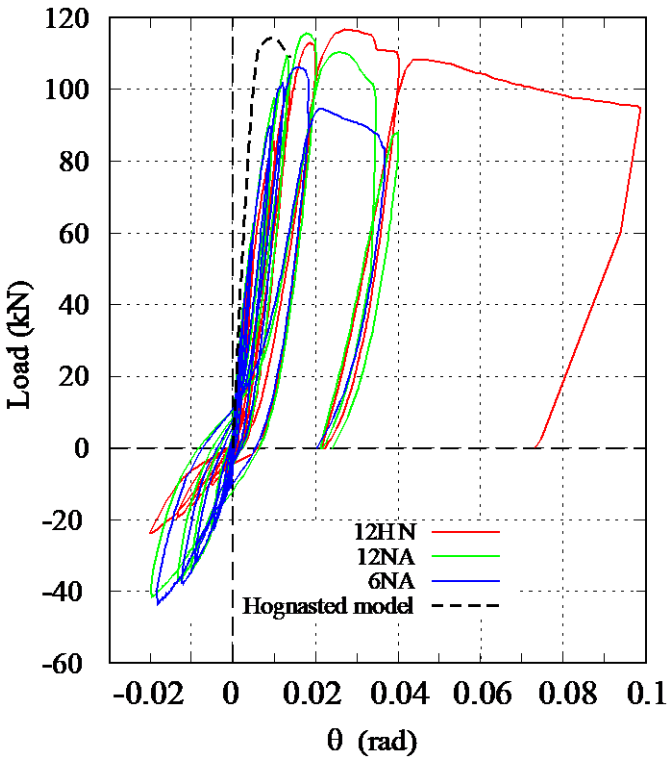

Figure 3.2.4. Comparison of experimental data and the Hognasted

3.3 Concrete Model Proposed by Mander (1988)

Mander et al. (1988a) first tested circular, rectangular and square full scale columns at seismic strain rates to investigate the influence of different transverse reinforcement arrangements on the confinement effectiveness and overall performance. Mander et al. (1988b) went on to model their experimental results. It was observed that if the peak strain and stress coordinates could be found, then the performance over the entire stress-strain range was similar, regardless of the arrangement of the confinement reinforcement used. To describe the entire stress-strain curve as shown in Figure 3.3.1, they adopted the 3-parameter Equation proposed by Popovics (1973).

The observed peak stress and strain of all tested specimens (Secion 4.3.1) are aimed to be analyzed using the Mander et al. (1988b) model as shown in Figure 3.3.1. According to Mander model, the confinement is to increase the strength and ultimate strain of concrete. Since the tested specimens have different detailing as well as different confinement types, therefore, the observed experimental data would further testify the model regarding detailing of the longitudinal reinforcement.

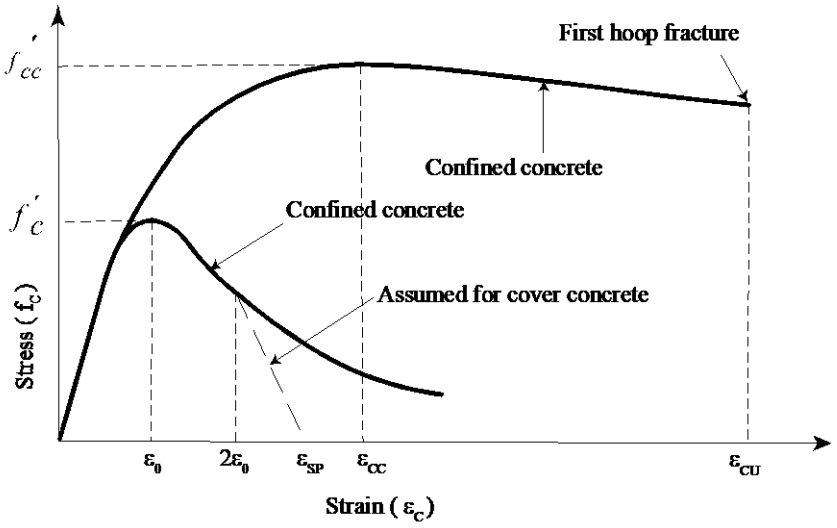

Figure 3.3.1. Stress-strain relation for monotonic loading of confined and unconfined concrete - Mander et al.

The Mander confined concrete stress-strain curve is defined by the following equations:

$$f_c = \frac{f'_{cc}\, xr}{r - 1 + x^r} \tag{3.3.1}$$

where *f'cc* compressive strength of confined concrete which is directly related to the effective confining stress f_l' that can be developed at the yielding of the transverse reinforcement and is given by Equation (3.3.2) and (3.3.3) for a rectangular section in the *x* and *y* directions.

$$f'_{lx} = K_e \rho_x f_{yh} \tag{3.3.2}$$

$$f'_{ly} = K_e \rho_y f_{yh} \tag{3.3.3}$$

ρ_x and ρ_y are the effective section area ratios of the transverse reinforcement to core concrete cut by planes perpendicular to the *x* and *y* directions as shown in Figure 3.3.2.

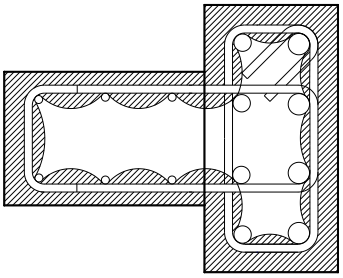

Figure 3.3.2. Confining of the concrete by rectangular hoops

K_e is a confinement effectiveness coefficient, relating the minimum area of the effectively confined core to nominal core area bounded by the centerline of the peripheral hoops. Typical values of K_e are 0.6 for the rectangular wall sections. Confined compressive stress is calculated using triaxle chart as shown in Figure 3.3.3, through ratio of effective confining stress f_c.

$$f'_{cc} = K\, f_c \tag{3.3.4}$$

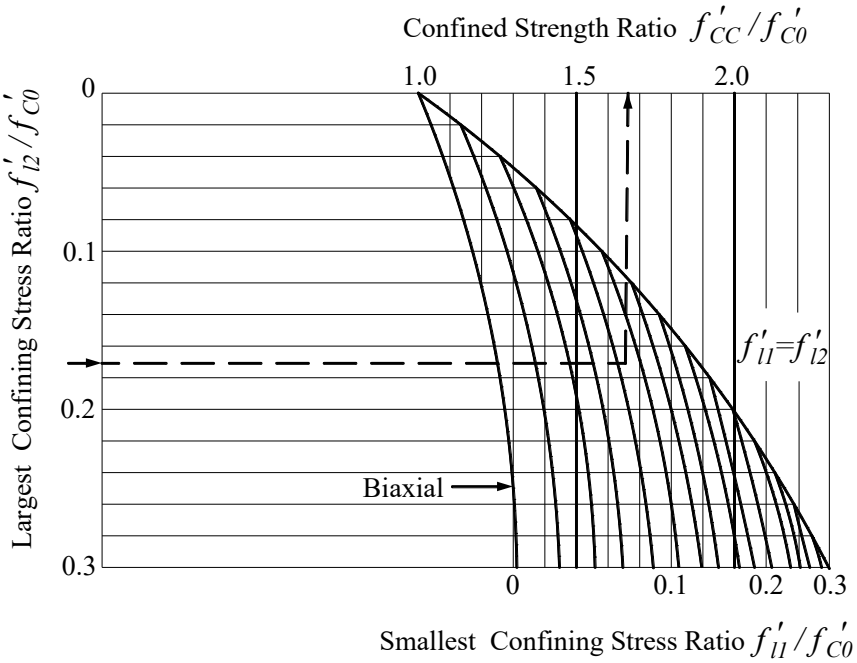

Figure 3.3.3. Abacus for the evaluation of the *k* strength increment factor of concrete for rectangular cross sections

K is measured at the tope axis of Figure 3.3.3 by interpolating between f'_{ly}/f'_c and f'_{lx}/f'_c.

Also *x* and *r* in Equation (3.3.1) are given by Equations (3.3.5), (3.3.6) and (3.3.7) as following:

$$x = \frac{\varepsilon_c}{\varepsilon_{cc}} \tag{3.3.5}$$

$$\varepsilon_{cc} = \varepsilon_{c0}\ \left[1 + 5\left(\frac{f'_{cc}}{f'_{c0}} - 1\right)\right] \tag{3.3.6}$$

$$r = \frac{E_c}{E_c - E_{sec}} \tag{3.3.7}$$

E_c and E_{sec} are the tangent and secant modulus of the concrete.

The analytical result of specimens which was obtained by the Monder model and peak observed experimental stress and strain for every specimen is plotted in Figure 3.3.4. The maximum stress and strain based on Mander model is shown with unfilled marks and the experimental result is shown with filled marks.

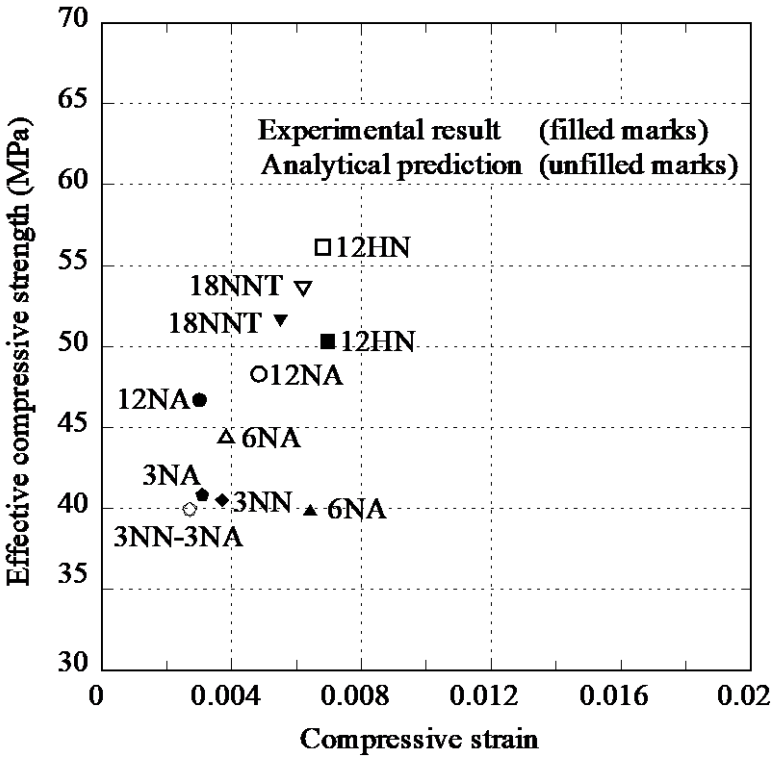

Figure 3.3.4. Comparison of the peak observed stress-strain and analytical stress-strain based the Mander model.

Comparison between the observed peak stress-strain in the experimental test and the peak stress-strain obtained using Mander model, is shown in Table 3.3.1.The peak observed strength of the tested specimens almost corresponds to the maximum strength, obtained using Mander model. The small differences between the experimental result and the model could be due to the detailing effect of longitudinal reinforcement, the variation of amount of transverse reinforcement, and concrete compressive strength. With this in mind, the ratio of Cal f'_{cc} / Exp f'_{cc} varies between 0.98 and 1.12. The average value of this ratio is 1.05 for the anchored detailing specimens and 1.03 for the non-anchored specimens. This indicates that the model scarcely overestimates the strength capacity of the non-anchored detailing specimen compared to anchored specimens. On the other hand, the impact of type of confining, placement of the longitudinal reinforcement, longitudinal reinforcement detailing and section geometry is not considered in this model while calculating the effective compressive strength.

Table 3.3.1. Test result parameters

Specimen	Peak stress-strain by Mander model		Peak stress-strain of test results		Ratio Cal f'_{cc} / Exp f'_{cc}	Ratio Cal ε_{cc} / Exp ε_{cc}
	Cal[1] f'_{cc}	Cal ε_{cc}	Exp[2] f'_{cc}	Exp ε_{cc}		
3NN	39.93	0.0027	40.8	0.0031	0.98	0.88
3NA	39.93	0.0027	40.5	0.0037	0.99	0.74
6NA	44.286	0.0038	39.8	0.0064	1.11	0.60
12NA	48.279	0.0048	48.3	0.0033	1.00	1.46
12HN	56.265	0.0068	50.3	0.0069	1.12	0.99
18NNT	53.724	0.0062	51.7	0.0055	1.04	1.13

[1] Calculated compressive stress-strain according the Mander model.

[2] Compressive stress-strain obtained from experimental test results.

On the contrary, the ultimate strain, obtained using Mander model, does not correspond to the peak observed strain of experimental results of anchored detailing specimens. In fact, the anchored detailing longitudinal reinforcement experienced compression-tension as a result of cyclic loading during the test which induced spreading of the cracks along the specimen and decreased the compression strain. However; the average ratio of Cal ε_{cc} / Exp ε_{cc} , for the specimen having non-anchored detailing, is equal to 1.0 which expresses that the strain predicted by the model almost comply with experimental results.

3.4 Summary

This chapter is aimed to evaluated Hognasted and Mander analytical models for confined concrete. Confinements resist shear stress, align the longitudinal reinforcement, prevent longitudinal reinforcement from buckling, reducing the spalling of concrete cover and confining the concrete. Transverse reinforcement in conjunction with longitudinal reinforcement acts to restrain the lateral expansion of the concrete, enabling higher compression stresses and more important, much higher compression strains to be sustained by the compression zone before failure occurs.

The model proposed by the Hognasted underestimates the drift capacity of the confined concrete after lateral drift of 0.5%. however; the predicted strength capacity of specimens based on the model is nearly complying with the experimental result with a scarce overestimation comparing to the specimen 6NA.

The model proposed by Mander scarcely overestimates the strength capacity of the non-anchored detailing specimen compared to anchored specimens. On the other hand, the impact of type of confining, placement of the longitudinal reinforcement, longitudinal reinforcement detailing and section geometry is not considered in this model while calculating the effective compressive strength.

On the contrary, the ultimate strain, obtained using Mander model, does not correspond to the peak observed strain of experimental results of anchored detailing specimens. However; the average ratio of Cal ε_{cc} / Exp ε_{cc} , for the specimen having non-anchored detailing, is equal to 1.0 which expresses that the strain predicted by the model almost comply with experimental results.

Chapter IV

Enhancement of Deformability of Reinforced Concrete Members with Non-Structural Wall

4.1 Introduction

Kumamoto earthquake in 2016 caused damages to the buildings, civil structures and human life. The earthquake and its consequences destroyed 248 non-residential public buildings including disaster management facilities in the city Asian Disaster Reduction Center (ADRC, 2016). In the event, reinforced concrete buildings, which were expected to be used as disaster management facilities following the earthquake, suffered severe damage and could not be used for post-disaster functions as intended (Fuji, et al., 2017). The examined post-disaster management buildings during the earthquake induced to find out necessary means to improve its safety and continues functionality (Saito, 2012).

The reinforcement bars either can be continued to the adjacent members or discontinued. An experimental study ascertained that discontinuity of a portion of the longitudinal web reinforcement in the possible weakened plane joint at wall mid-height and the lack of hooks on transverse reinforcement may have some negative influence on the expected shear strength of wall segments expected to fail in diagonal tension; but the influence is rather modest (Orakcal, et al., 2008).

The objective of this chapter is to evaluate methods that enhance deformability of non-structural spandrels. For this purpose, first of all it is aimed to evaluate the impact of seismic slit on the performance of a component having beam, standing and hanging walls, using cyclic loading experimental approaches. In addition, to ascertain the impact of AIJ and ACI based designed confinement reinforcing bars which are placed in the critical strip of spandrel walls. Moreover, this study aims to develop a new detailing method for spandrels which are aimed to be used as a means for enhancing of the seismic capability and continues functionality of post-disaster management buildings. The method was assessed for hanging walls through an artificial earthquake in a real three-story building to verify its effectiveness.

4.2 Detail of proposed method

A new detailing method for connection of a non-structural spandrel wall with either a column or another wing wall is proposed herein. The beam has an isolated non-structural hanging or standing wall casted to be monolithic with the frame elements. These walls are also casted to be monolithic with another wall or column element at its ends without seismic slits as shown in Figure 4.2.1a. As part of this proposed method, longitudinal reinforcement within the spandrel wall should not be anchored into the adjacent member as shown in Figure 4.2.1b; hence, this type of detailing is referred to as non-anchored detailing.

When the anchorage of longitudinal wall reinforcement is eliminated, cracks would then generally only occur at the wall ends, which prevents significant spread of cracks along the wall length and increase deformability. An experimental study verified that the deformation capacity of the composite Concrete Encased Steel (CES) shear walls improves by non-anchorage of the longitudinal wall reinforcement, because the damaged area of concrete of wall panel was reduced by the occurrence of slip between the wall panel and boundary beam after reaching the maximum strength (Suzuki, et al., 2012).

Furthermore, the wall would only contribute in compression, which increases initial stiffness and lateral strength moderately compared to using seismic slits. In summary, a beam member with spandrel wall whose longitudinal wall reinforcement is not anchored has larger or equivalent deformability compared with an anchored one. It can be assumed that the proposed structural system would demonstrate relatively higher lateral strength than beam and higher ductility compared to a member having wall reinforcement anchorage as shown in Figure 4.2.1c.

This proposed method of detailing is evaluated through static and dynamic experimental tests, firstly, the method tests on a member-by-member basis, secondly, to investigate how the design method affect the entire building, the dynamic test of a three story building is carried out.

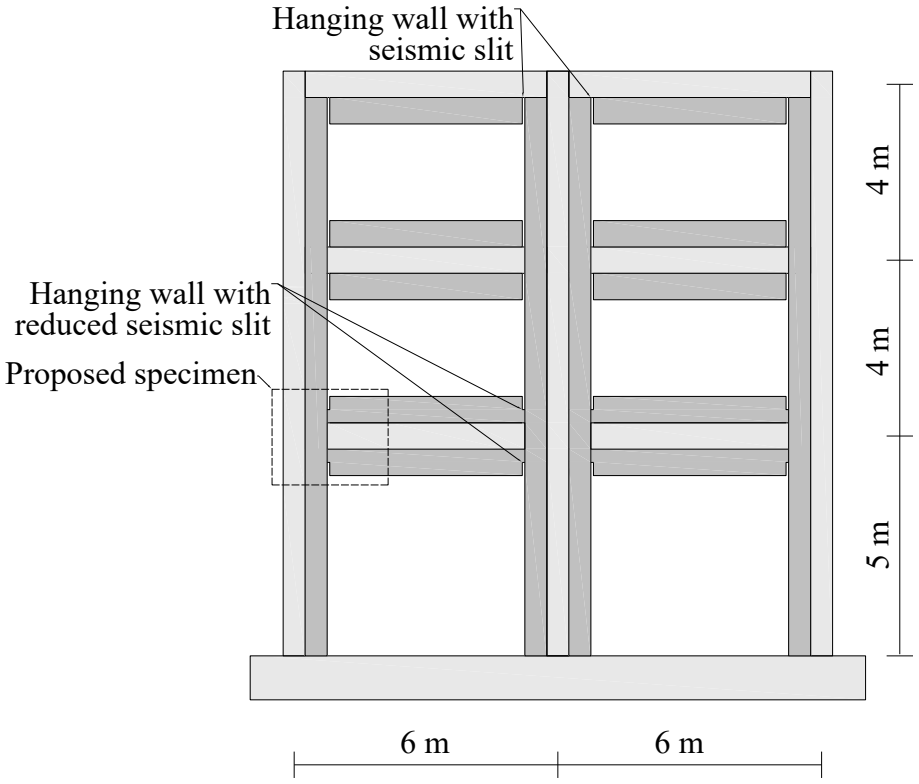

(a)

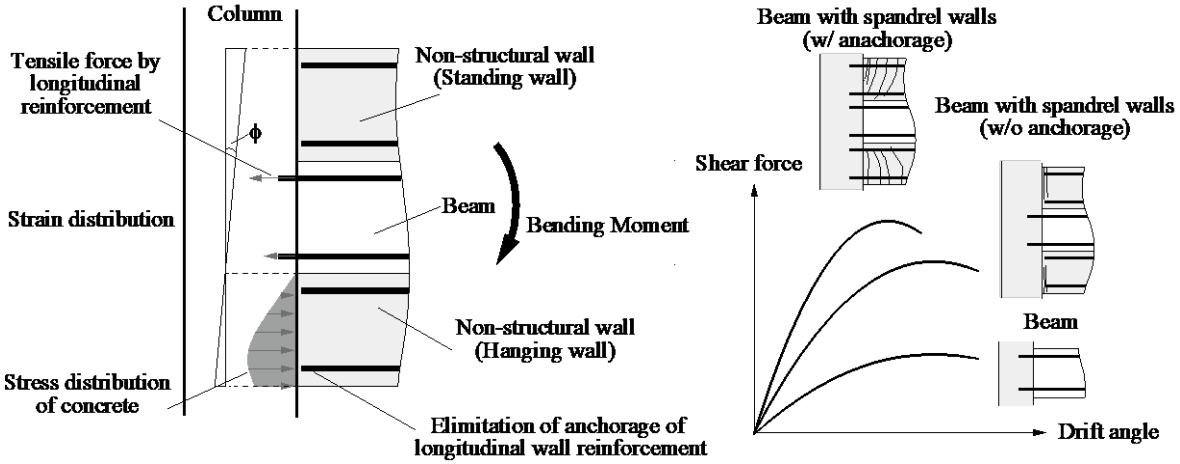

(b) (c)

Figure 4.2.1. Proposed new detailing of reinforced concrete member with non-structural walls: (a) specimen position in the frame; (b) working mechanism; (c) expected performance

4.3 Static Evaluation of Proposed Detailing Method

4.3.1 Test specimens

Two full-scale specimens were designed and tested under cyclic loading in order to verify the performance of the proposed method for isolated non-structural spandrel wall attached to a beam. The structural properties of the specimen were determined based on required demand forces for disaster management facilities. The specimen simulated a beam in the structural frame, which had spandrel walls as shown in Figure 4.3.2 and Figure 4.3.3.

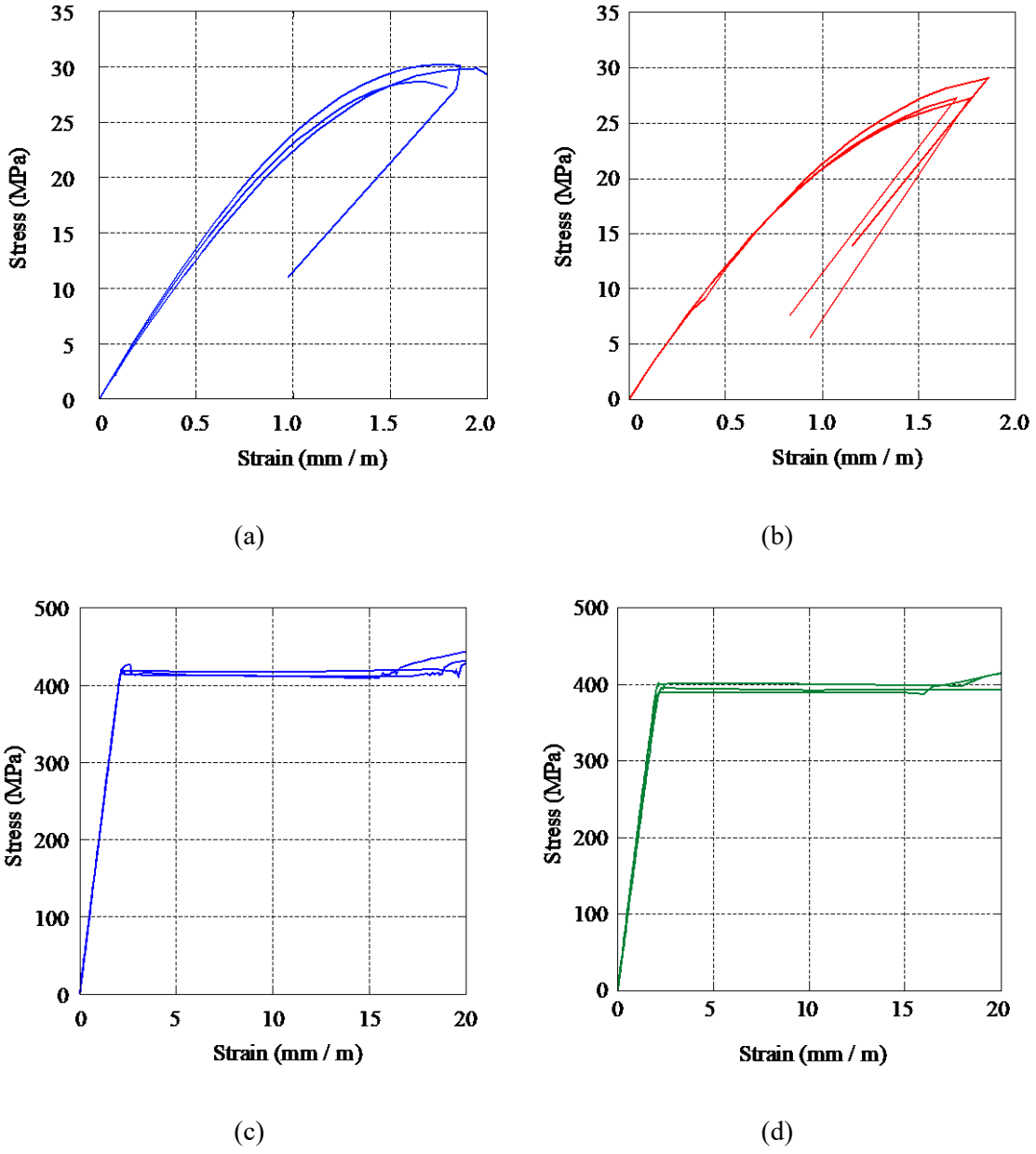

Figure 4.3.1.Stress-strain relation : (a) concrete of BS; (b) concrete of BSH; (c) steel bar D13; (d) steel bar D19

The reinforcement details of the specimen are shown in Table 4.3.3; concrete and steel properties of the specimens which were obtained from concrete cylinder compression and bar tensile pull tests are shown in Figure 4.3.1, Table 4.3.1 and Table 4.3.2.

Table 4.3.1. Concrete properties

	BS	BSH
Compressive strength (MPa)	30.0	27.9
Young's modulus (MPa)	26.9×10^3	23.9×10^3

Table 4.3.2. Steel properties

Number	D13	D19
Type	SD295A	SD345
Yield stress (MPa)	423	397
Tensile stress (MPa)	600	579
Young's modulus (MPa)	202×10^3	194×10^3

Table 4.3.3 Details of specimens

Name	BS	BSH
Type of member (B×D)	Beam (400 mm × 600 mm)	
Long. reinforcement	12-D19 (ρ_l = 1.56%)	
Trans. reinforcement	D13@150 (ρt = 0.42%)	
Wall type (Thickness)	Spandrel Walls (200 mm)	
Length of walls (mm)	600 (300 at the wall boundary)	
Long. wall reinforcement	2-D13@150	
Trans. wall reinforcement	2-D13@150 (0.84%)	

Design of confinement reinforcement	AIJ	ACI
Confinement reinforcement (X)	(0.85 %)	2-D13@75 (2.54%)
Confinement reinforcement (Y)	D13@150 (0.15%)	2-D13@75 (1.13%)
Initial target load (kN)	88 (1st) and 162 (2nd)	
Target drift angle (rad)	±1/400, ±1/300, ±1/200, ±1/150, ±1/75, ±1/50, ±1/37.5, ±1/25	

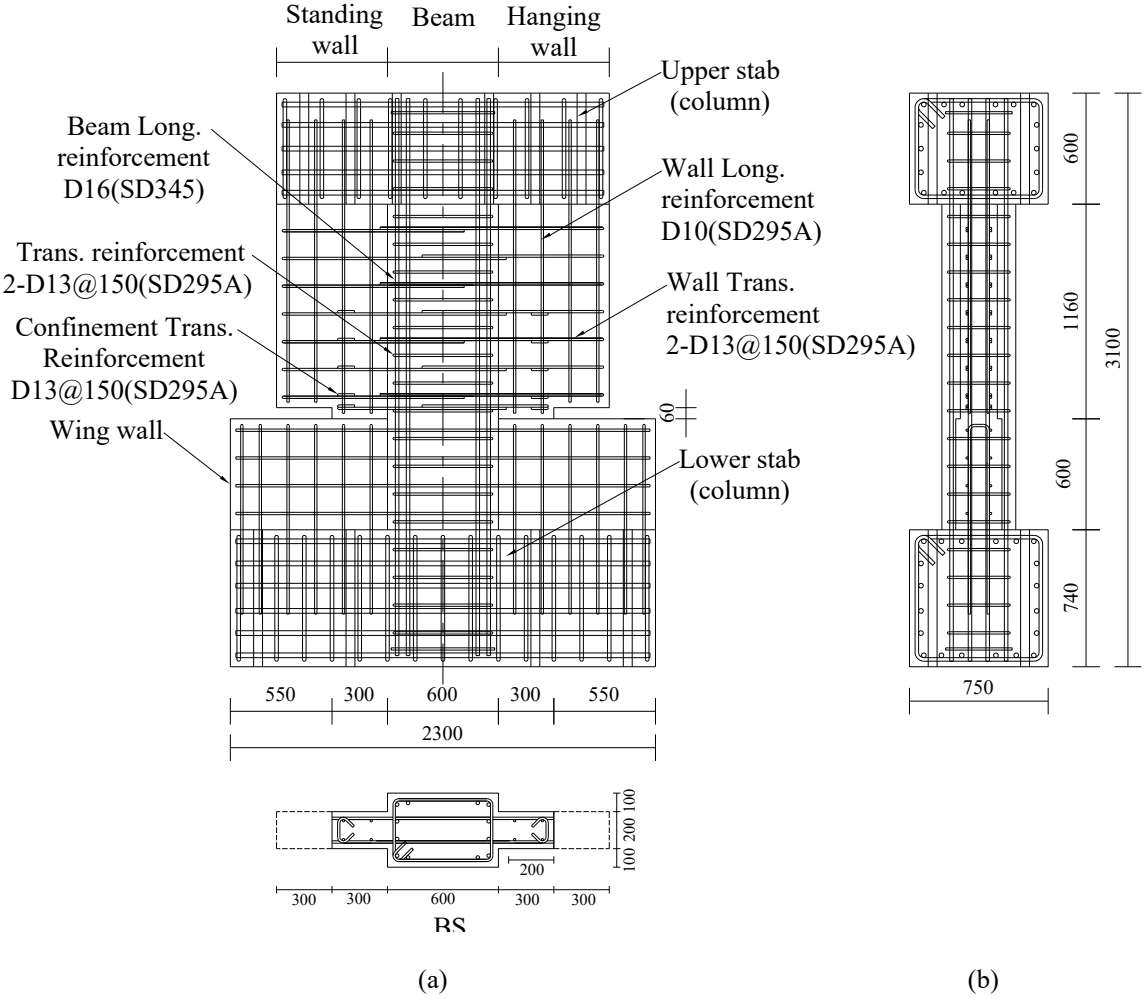

Figure 4.3.2. Geometry of specimen BS; (a) in-plane view; (b) out-plane view of

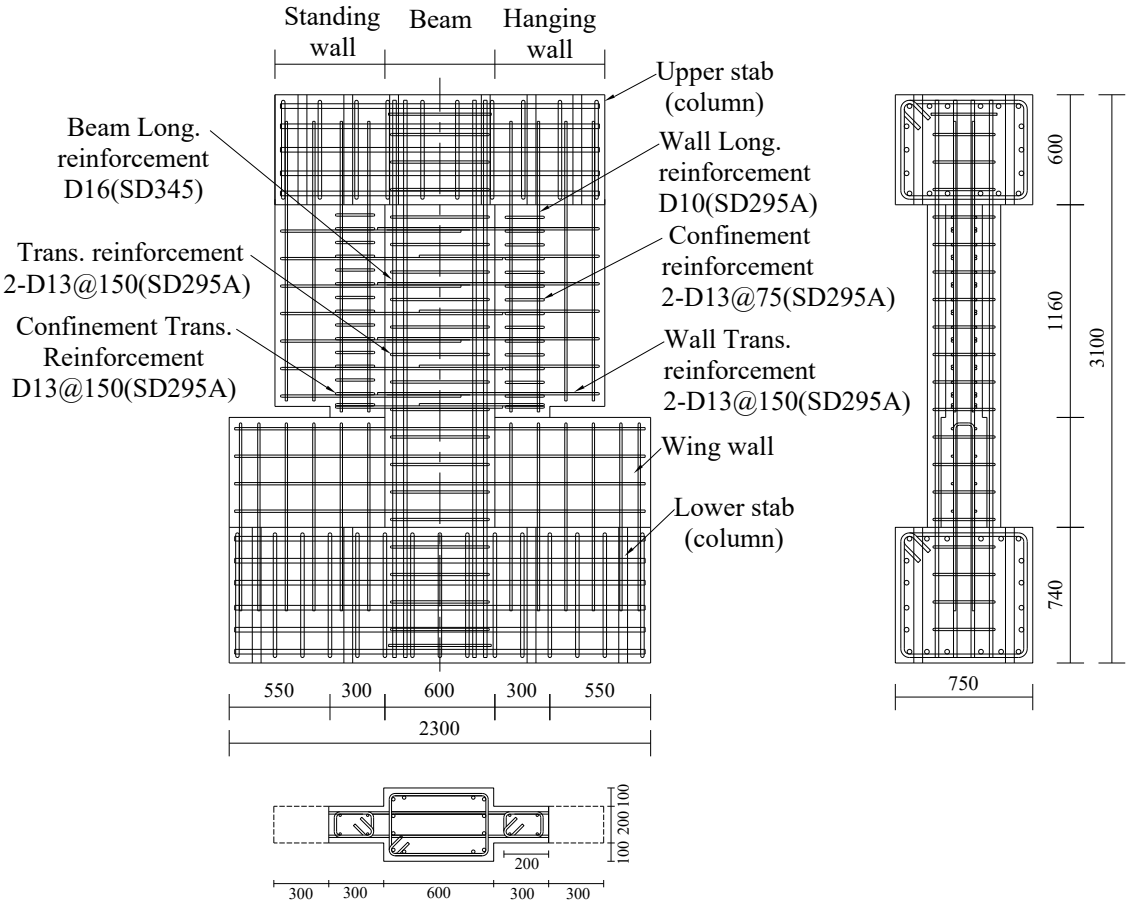

Figure 4.3.3. Geometry of specimen BSH; (a) in-plane view; (b) out-plane view of

The confinement stirrups are designed based on the special boundary element provision of the ACI-314 using Equations (4.3.1) and (4.3.2). The greater value of these equations will be considered as the boundary confinement ratio of the specimen.

$$\frac{A_{sh}}{Sb_c} = 0.3\left(\frac{A_g}{A_{ch}} - 1\right)\frac{f_c}{f_{yt}} \tag{4.3.1}$$

$$\frac{A_{sh}}{Sb_c} = 0.09\frac{f_c}{f_{yt}} \tag{4.3.2}$$

where,

Ag and A_{ch} expressions are defined as $A_g = \ell_{be} \times b$ and $Ach = b_{c1} \times b_{c2}$,

ℓ_b and $b_{c1} \times b_{c2}$ can be found based on Equation (4.3.3) and ACI provisions.

$$l_{be} = Max(C - 0.1l_w \ \ and \ \frac{C}{2}) \tag{4.3.3}$$

where *C* is center of neutral axes and calculated as following,

$$c \geq \frac{l_w}{600\,(1.5\,\delta_u / h_w)} \tag{4.3.4}$$

Confinement bar stirrups spacing is considered lesser of the following assumptions:

- shall be one-third of the least dimension of the boundary element.
- Six times the diameter of the smallest longitudinal bar.
- $4+((14\text{-}h_x)/3)$.

The main parameters of the specimens are existence and non-existence of the confinement reinforcement placed at the wall critical strip as shown in Figure 4.3.2 and Figure 4.3.3. The amount of longitudinal and transverse reinforcements of the members were determined based on required moment capacity and shear force assumed in the design under consideration. The confinement reinforcement at the wall boundary was designed according to the boundary element specified in the (ACI 318) code and the design standard for reinforced concrete buildings in Japan (AIJ, 2016). As previously mentioned, none of the longitudinal wall reinforcing bars were anchored.

The specimen BS and BSH were fabricated as beams with non-structural spandrel walls, hence, the spandrel wall was attached to the wing wall without seismic slit in the critical area. The slit width is set so that to avoid contacting with wing wall during loading, even the value at the interlayer deformation angle reached 1/15 rad as shown in Figure 4.3.4.

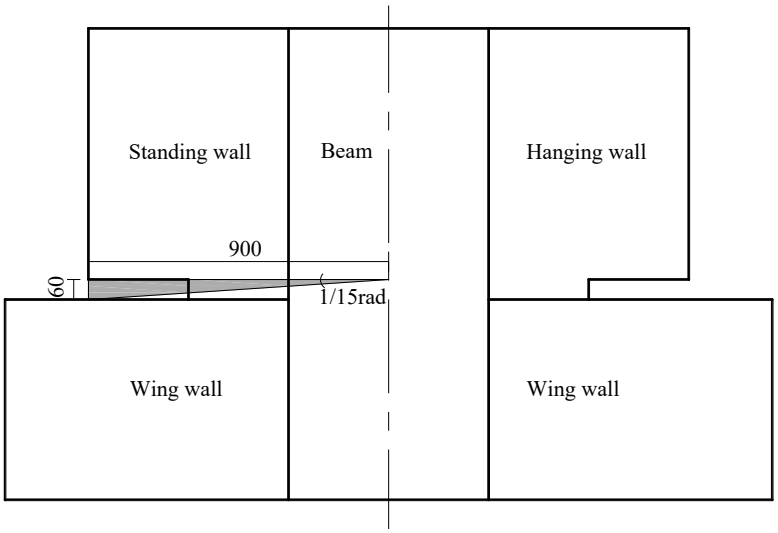

Figure 4.3.4.Seismic slit size to control hanging and wing walls contact under 1/15rad drift

As shown in Figure 4.3.3, the specimen BS and BSH consisted of beams, spandrel walls, and wing walls. The wing walls were placed horizontally below the wall boundaries, hence, the footing beam effectively serves as a column. The wall length was 600 mm, which corresponded

to the depth of the beam; however, at the wall boundary cross-section, the length was reduced to 300 mm because the moment capacity tended to be attributed to the wall length. The confinement reinforcement at the wall boundary was determined based on the AIJ and ACI codes. The amount of the confinement reinforcement specified by the ACI code was larger than that of the AIJ code. The confinement reinforcement ratio in each direction included the amount of the wall reinforcement.

Figure 4.3.5 shows the diagram of the experimental setup which was carried out in the Hiroshima university at the structural engineering experimental laboratory. The specimens were subjected to asymmetric bending moment controlled by two vertical jacks on both sides of the specimen. The horizontal load was applied using a hydraulic jack installed at the loading beam.

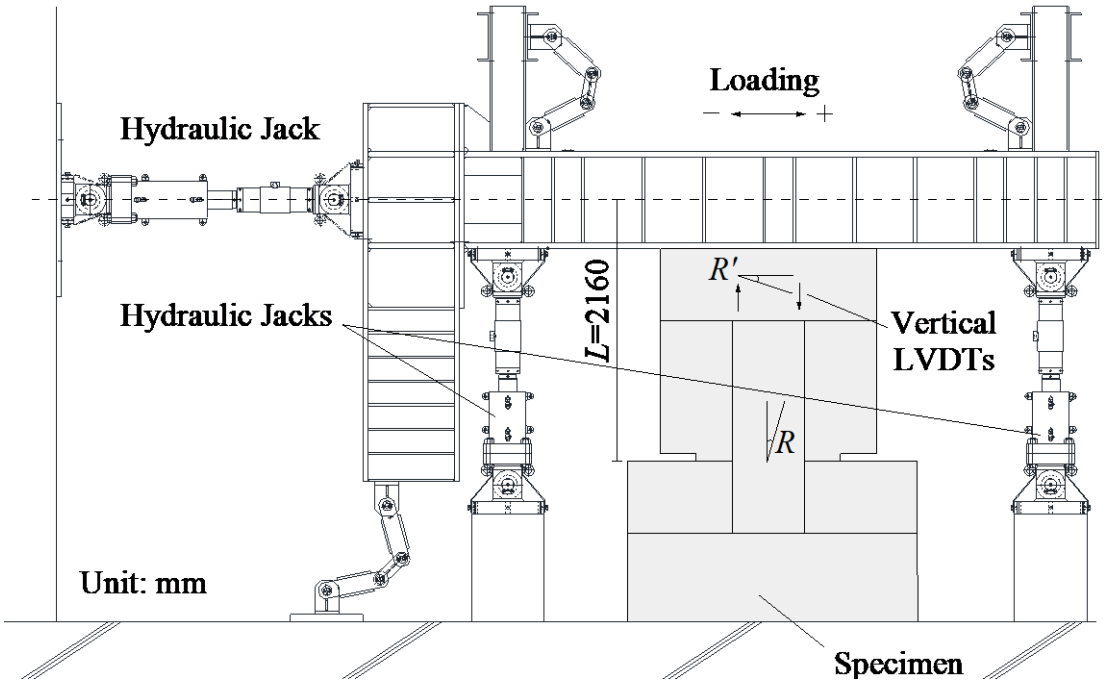

Figure 4.3.5. Experimental setup

The cyclic loading test was conducted by controlling the target horizontal load and drift angle. The loading started from the initial target load as shown in Table 4.3.3. The loads were designed based on the allowable stress design limit. After the initial loading, the specimen was pushed until it reached the target drift angle R (horizontal displacement divided by shear span length, L, of 2160 mm for the beam). The lower and upper stabs were fixed by threaded rods having 35 mm diameter, the upper stab was fixed to the top set up using 8 rods by applying 200kN force on each rod. Likewise, the upper stab was fixed to the bottom foundation, using 8 rods, with exerting 300kN on each rod.

4.3.2 Measurement instruments

The measurement instruments were used to record horizontal load, vertical axial load; horizontal displacement (lateral displacement), global vertical displacement of the specimen; local horizontal and vertical displacement of each element (beam, hanging wall and wing wall); strain of longitudinal and transverse reinforcements; cracking pattern and cracks width. Load cell having capacity of 15000 kN and sensitivity of 1.0 MV/V, attached to the hydraulic jack, measured the horizontal and vertical axial loads.

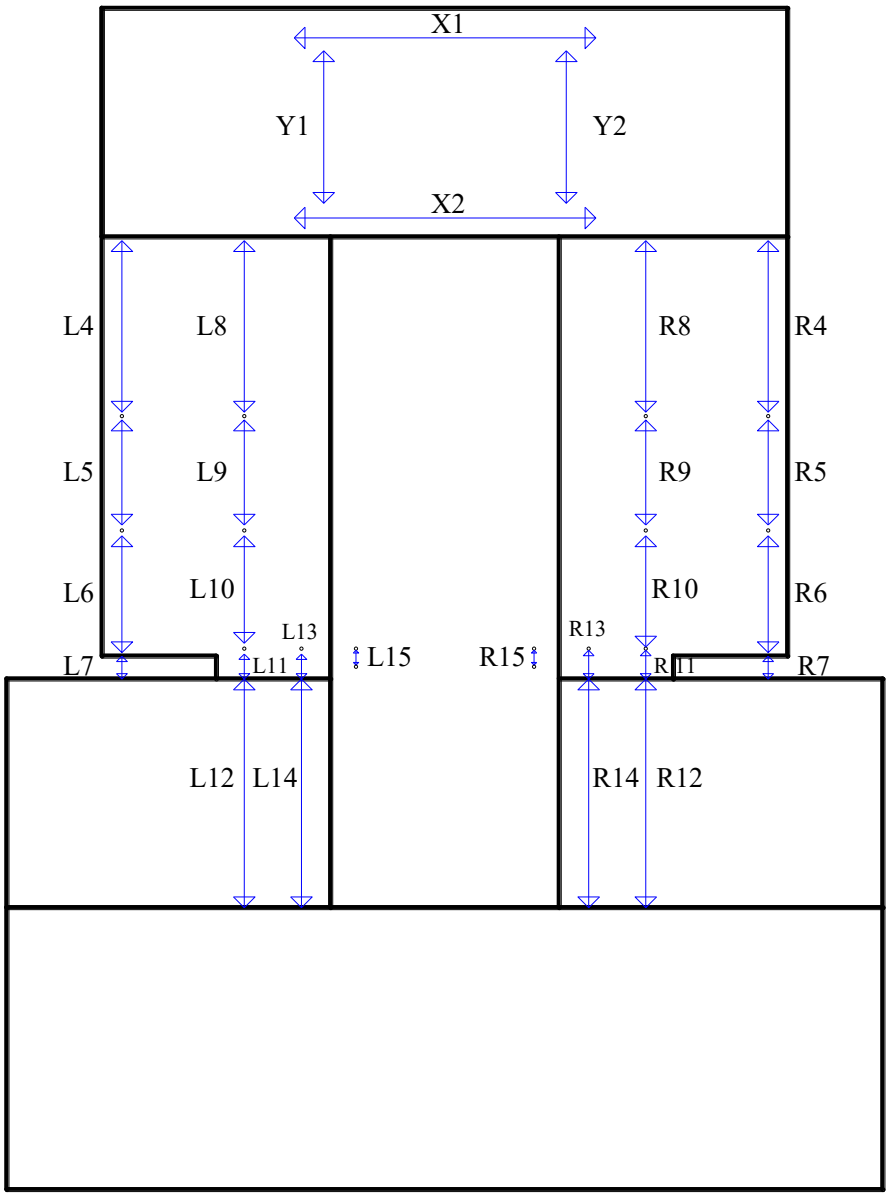

(a) LVDTs used for measurements of the total displacement of the specimens and spandrels;

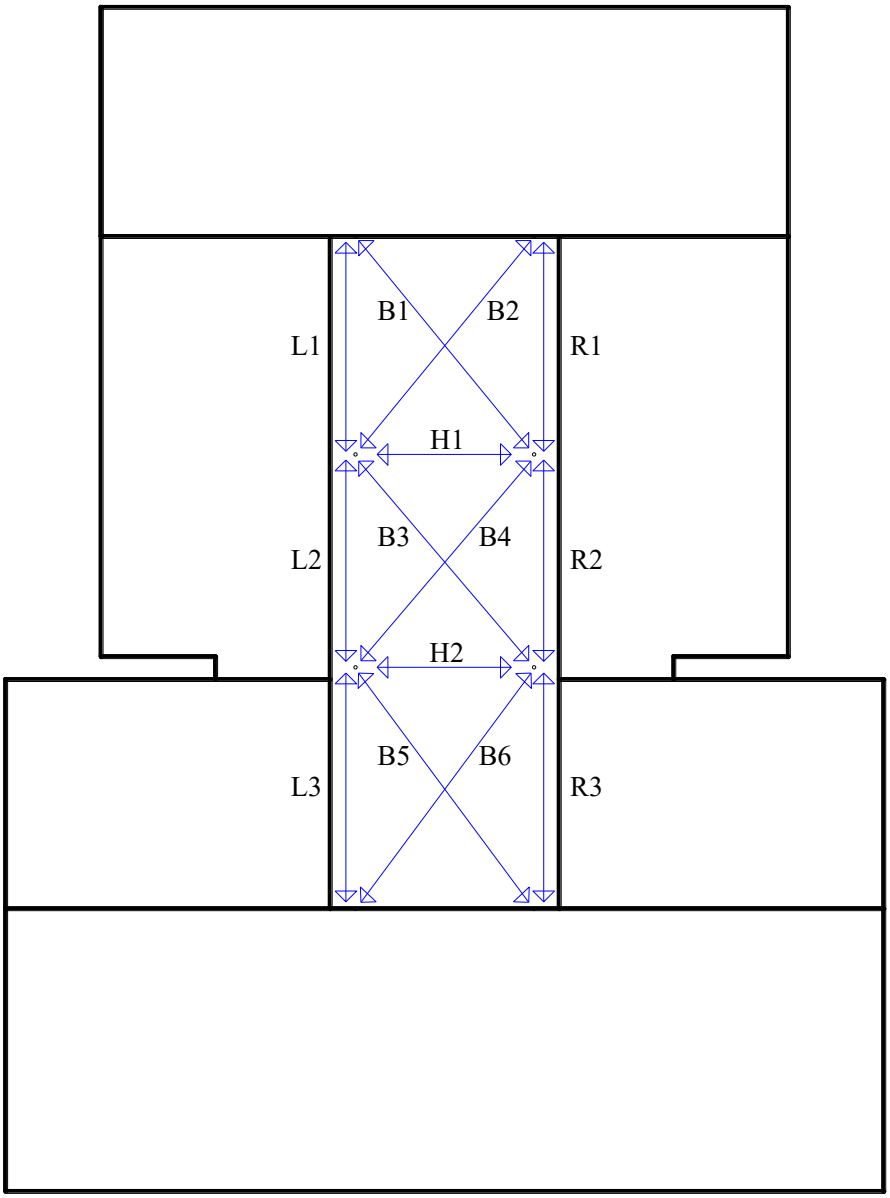

(b) LVDTs used for measurements of beam.

Figure 4.3.6.Locatio of the LVDTs on the surface of specimen BS and BSH:

The total lateral displacement of the specimen was calculated using average record of the X1 and X2 linear variable transducers (LVDT) which were installed on the back side of upper stab a long with loading plane; and the total vertical displacement was measured using average record of Y1 and Y2 transducers. The local deformation of the beam, hanging and winging walls was also measured by LVDTs installed on the back side of the specimen. A list of used LVDTs is shown in Table 4.3.4 and detail diagram is shown in Figure 4.3.6b.

Table 4.3.4 Detail of LVDTs on the surface of specimen BS and BSH

Name of LVDTs	Measurement location	LVDT Type	Capacity [mm]	Sensitivity [μ]
X1, X2	Upper stab horizontal Disp.[1]	SDP-200	200	50
Y1, Y2	Upper stub vertical Disp.	CDP-100	100	100
H1, H2	Beam horizontal Disp.	CDP-25	25	500
L1, L2, L3	Beam vertical Disp. (L)[2]	CDP-25	25	500
R1, R2, R3	Beam vertical Disp. (R)[3]	CDP-25	25	500
B1, B2, B3, B4, B5, B6	Beam shear direction Disp.	CDP-25	25	500
L4, L5, L6	Wall edge vertical Disp.(L)	CDP-25	25	500
L7	Wall edge Disp. at the end of slit (L)	CDP-100	100	100
L8, L9, L10	Vertical Disp. In the compression zone of wall (L)	CDP-25	25	500
L11, L13	Vertical Disp. of slit (L)	CDP-25	25	500
L12, L14	Critical zone Disp.(L)	CDP-50	50	200
L15	Beam vertical Disp. at the location of slit (L)	CDP-10	10	1000
R4, R5, R6	Vertical Disp. at end of wall (R)	CDP-25	25	500
R7	Wall edge Disp. at the end of slit (R)	SDP-200	200	50
R8,R9,R10	Vertical Disp. In the compression zone of wall(R)	CDP-25	25	500
R11, R13	Vertical Disp. of slit (R))	CDP-25	25	500
R12, R14	Critical zone Disp. (R))	CDP-50	50	200
R15	Beam vertical Disp. at the location of slit (R)	CDP-10	10	1000

[1] Displacement, [2] Lift , [3] Right

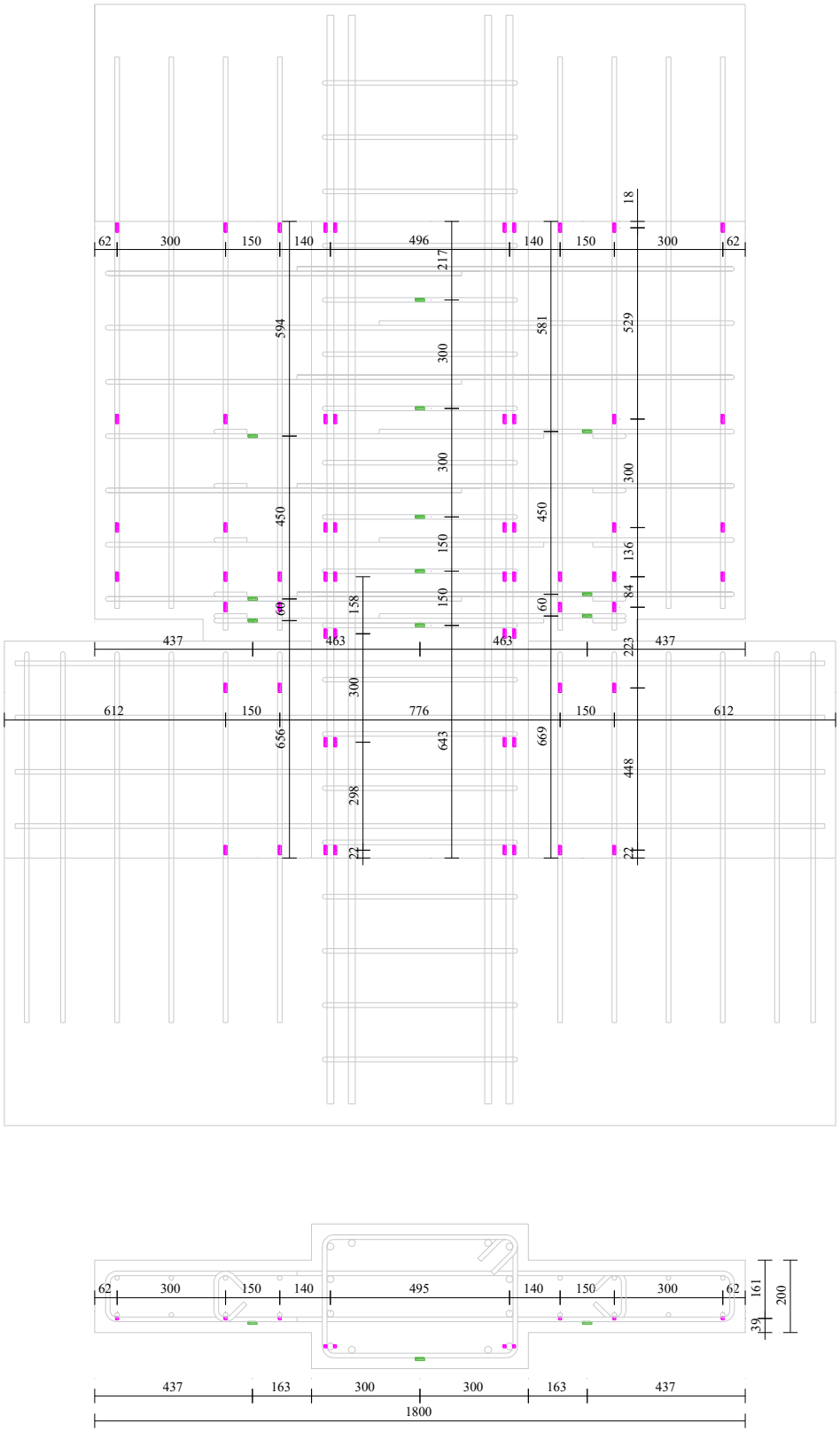

Figure 4.3.7. Location of the strain gauges on the reinforcement of specimen BS

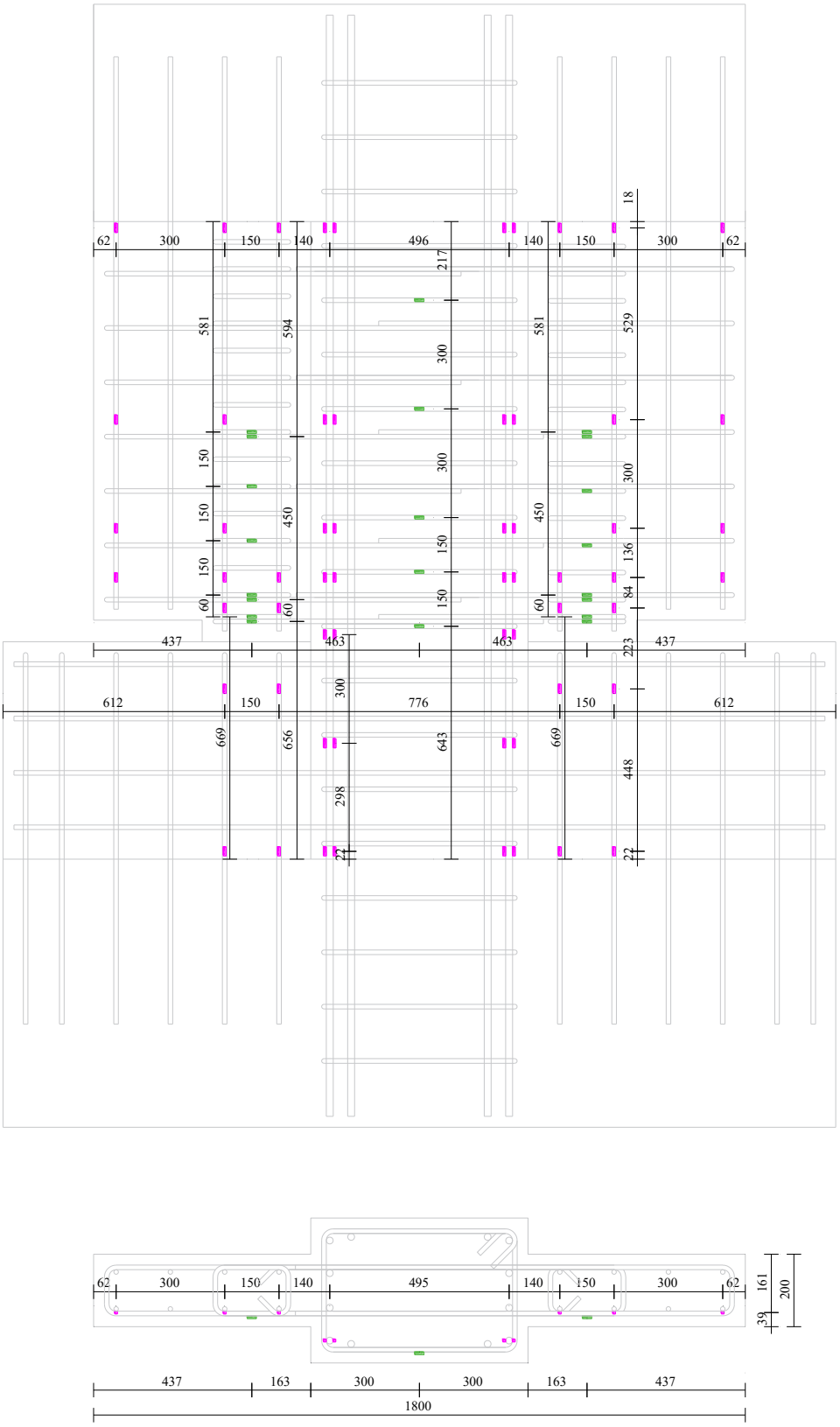

Figure 4.3.8. Location of the strain gauges on the reinforcement of specimen BSH

The strain gauges which were installed on the longitudinal and transverse reinforcement of beam, hanging and wing walls, measured the occurred strain on the reinforcements. The incurred strain on the confining reinforcement of the specimen BSH was recorded by strain gauges, pasted in plane and out of loading plane of confinements. as can be seen in Figure 4.3.7 and Figure 4.3.8, strain gauges were installed on the places where higher damage was expected.

4.4 Test Results

4.4.1 Relationship between horizontal load and drift angle

The relationships between horizontal load and lateral displacement are shown in Figure 4.4.1. The square and circle symbols represent the yielding of the longitudinal reinforcement and peak horizontal load observed, respectively. The beam longitudinal reinforcement of both specimens reached yielding limit at the drift of 1/200 rad. The maximum observed strength was obtained at the drift of 1/100 on the positive side; while the maximum strength in the negative side was observed at the 1/25 drift. The specimen BS and BSH showed similar trends.

Firstly, bending cracks occurred during initial loading cycle. Secondly, the longitudinal reinforcement of beam in both specimens yielded at 1/200 rad and minor stiffness degradation was seen. Thirdly, compression failure in the concrete cover of the non-structural wall was observed at 1/150 rad for both specimens. Afterwards, slip behavior was seen for both specimens following yielding of the longitudinal reinforcement. Finally, the horizontal load increased until reaching the peaks of 313 kN and 285 kN for specimens BS and BSH, respectively, at 1/25 rad drift angle.

The maximum horizontal load nearly agreed with the predicted shear strength using cross-sectional analysis. Moreover, high ductile performance was observed from both specimens regardless of the amount of the confinement reinforcement for the range of drift demands considered. Thus, it was confirmed that non-anchorage of the longitudinal spandrel wall reinforcement and reduction of the seismic slit increased flexural moment capacity and deformability to the structural member.

The dashed lines in Figure 4.4.1 represent the analytical predictions for the specimen, which were obtained from the moment–curvature relationship using cross-sectional analysis software Response-2000 [6]. Response-2000 allows analysis of beams and columns subjected to arbitrary combinations of axial load, moment and shear. It also includes a method to integrate the sectional behavior for simple prismatic beam-segments. The assumptions implicit in the program are that plane sections remain plane, and that there is no transverse clamping stress across the depth of the beam.

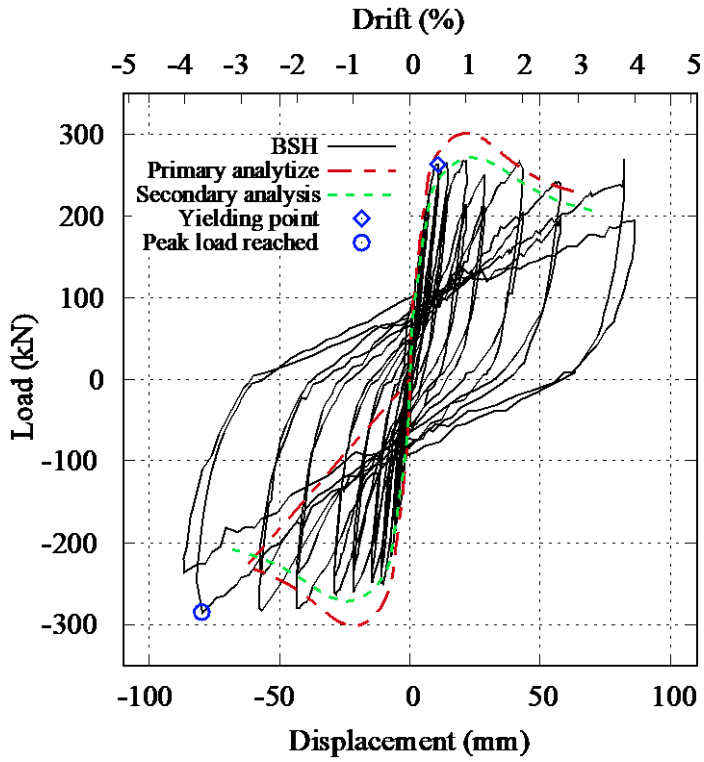

(a)

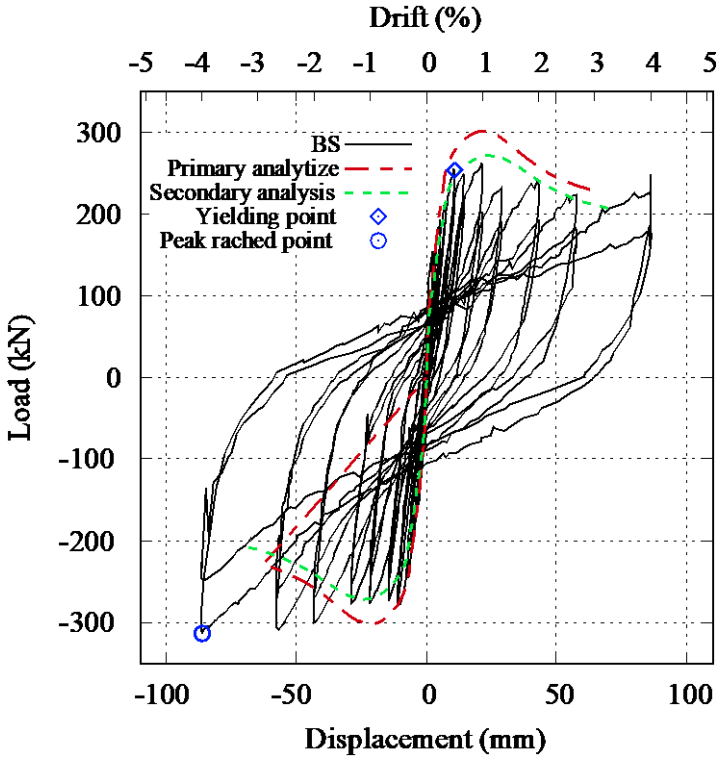

(b)

Figure 4.4.1. Relationship between horizontal load and lateral displacement: (a) BSH; (b) BS

Both specimens section was modeled in Response-2000 based on their detailed material property obtained from the experimental testing results as shown in Figure 4.3.1. The concrete stress-strain curve was assumed based on (Popvics, et al., 1973), model and steel stress-strain distribution was developed according to the modified input data. The analytical lateral load-deflection curve was obtained using following equation:

$$Q = \frac{M}{l} \tag{4.4.1}$$

$$\delta = \varnothing \times l_p \times l \tag{4.4.2}$$

Where:

Q: Lateral load carrying capacity of the specimen.

M: Moment which was obtained from sectional analysis.

l : Shear span length

δ : Lateral drift of the specimen

$\emptyset$: Curvature of the specimen section, obtained from sectional analysis.

l_p: Plastic hinge length.

Almost all of the above parameters was easily identified in the sectional analysis except shear span and plastic hinge lengths. According to the geometry of the specimen, the shear span length was considered to be 2160 mm in the primary analytical prediction which overestimated the strength capacity of the specimen compared to experimental result. Therefore the shear span length was ascertained using experimental data at each drift level, the detail is explained in section 4.4.4. The secondary anlaysis was carried out based on the refined shear span length that was observed during the test.

The determination of the length of plastic hinge length is a critical step in predicting the lateral load-drift response of columns. As it is difficult to estimate the plastic hinge length by using sophisticated computer programs, it is often estimated based on experimental data or by using empirical equations. However, several factors influence the length of plastic hinge, such as:1) Level of axial load; 2) Moment gradient; 3) The value of shear stress in the plastic hinge region; 4) The amount and mechanical properties of longitudinal and transverse reinforcement; 5) Strength of concrete; and 6) Level of confinement provided in the potential plastic hinge zone (Sungjin, et al., 2008).

Plastic hinge length of reinforced concrete columns discussion. The plastic hinge length was considered based on the curvature distribution along the beam height and extended shear span length to the wing wall. The curvature distribution which was found based on the strain gauge records, indicates the hinge length 600mm above the wing wall as shown in Figure 4.4.2. In addition, the shear span length extended to the wing wall until 300 mm according to the shear

span length predication analysis. Considering all these evidences the total plastic hinge length was assumed 900mm which almost corresponds with the experimental results.

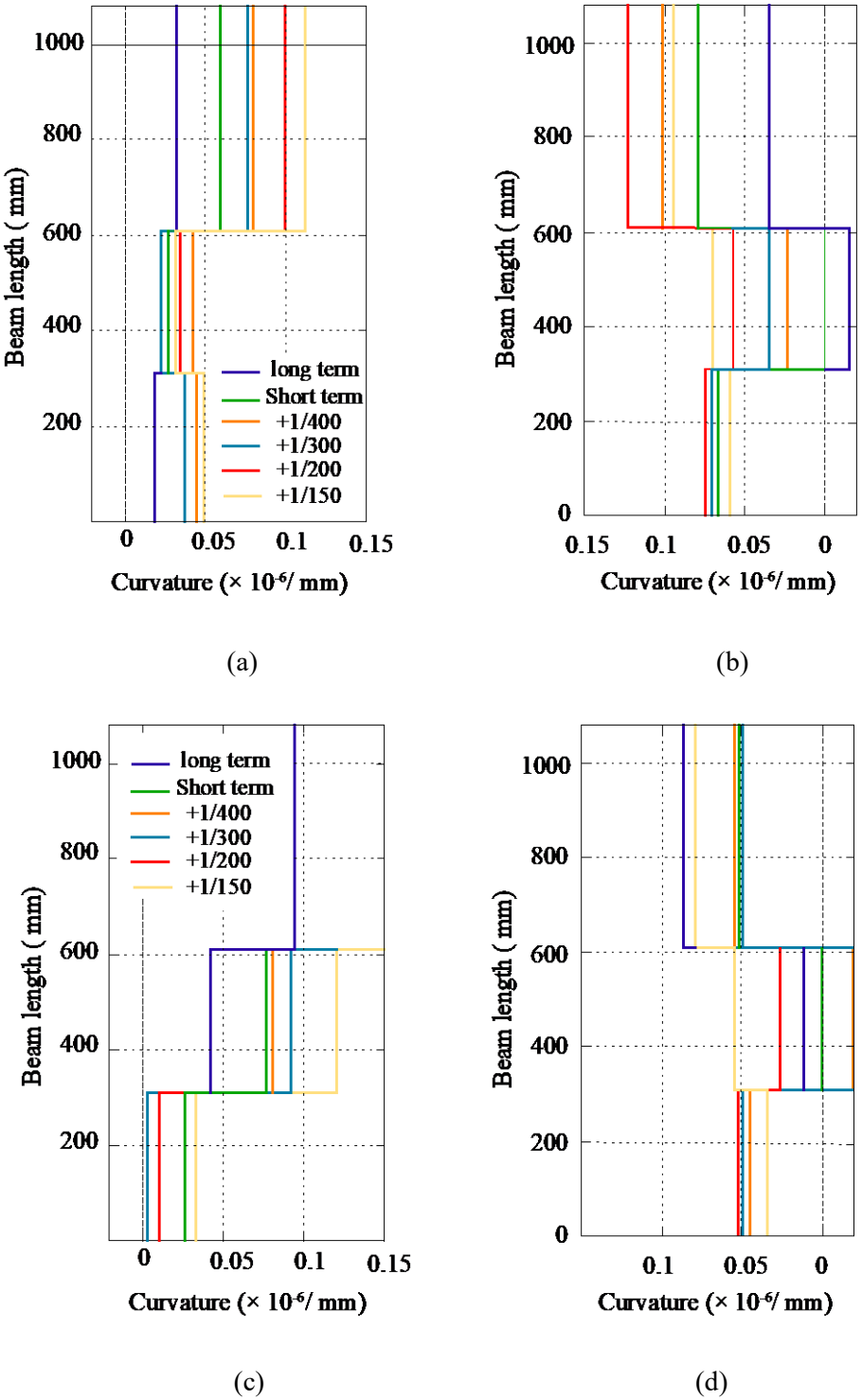

Figure 4.4.2. Curvature distribution along the height of the beam from LVDTs: (a) BS curvature under positive loading; (b) BS curvature under negative loading; (c) BSH curvature under positive loading; (d) BSH curvature under negative loading

4.4.2 Cracking behavior

Crack patterns in both specimens were drawn at a 1/50 and 1/100 rad drift angle, as shown in Figure 4.4.4 and Figure 4.4.4. The painted area represents the spalling area of the concrete. The bending cracks appeared in the spandrels at a drift angle of 1/200 rad and extended diagonally into the structural system as the drift angle increased. The spandrel walls of the beam showed dominant flexural behavior compared with the beam itself, owing to a larger cross-section at the middle of the spandrel wall than at its ends. The spalling area in the concrete was influenced by the amount of confinement reinforcement as shown in Figure 4.4.3 and Figure 4.4.4.

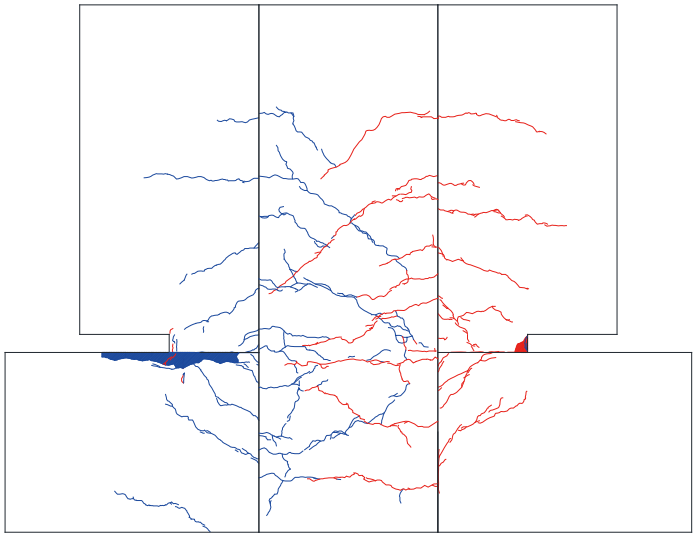

(a)

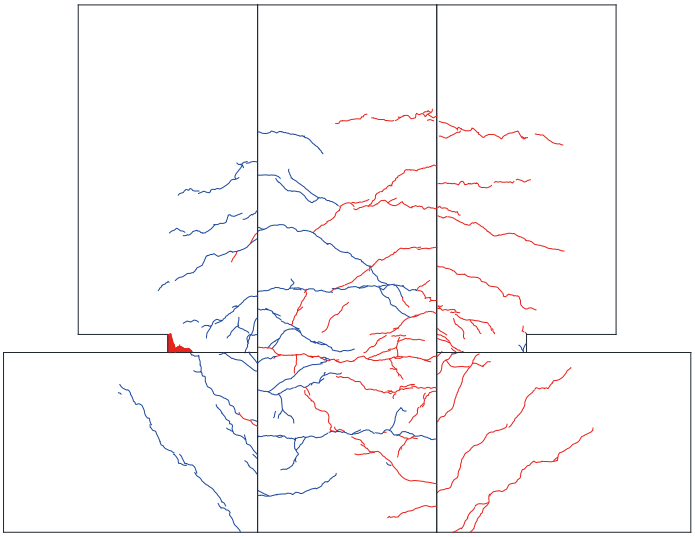

(b)

Figure 4.4.3. Crack patterns at 1/100: (a) BS; (b) BSH

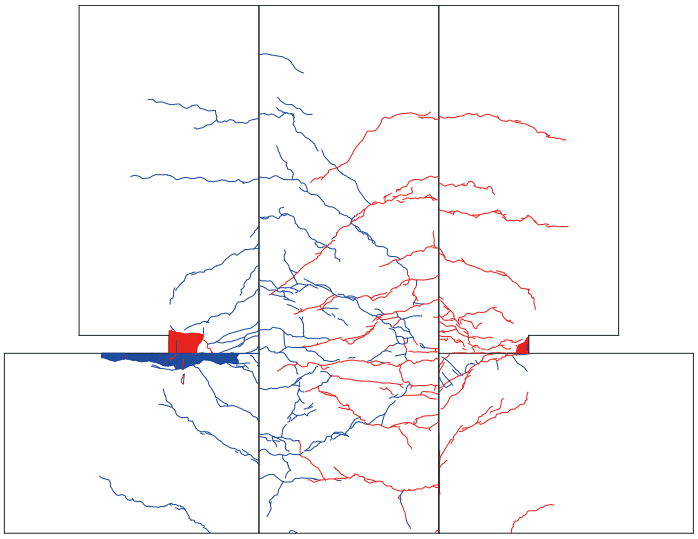

(a)

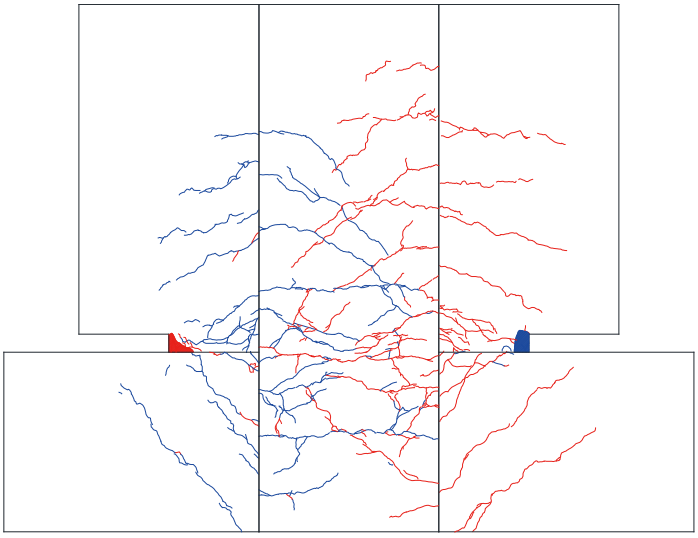

(b)

Figure 4.4.4. Crack patterns at drift 1/50: (a) BS; (b) BSH

Figure 4.4.5 shows the relationship between residual crack width and drift angle. The width was measured on the structural member and the wall. The crack width was observed to increase with increasing drift angle; however, a dominant wider crack was observed at the wing wall interface in both specimens because the longitudinal wall reinforcement was not tied to the footing beam. The dominant cracks between the wall boundary and the footing beam occurred at a drift angle of 1/50 rad, as shown in Figure 4.4.6.

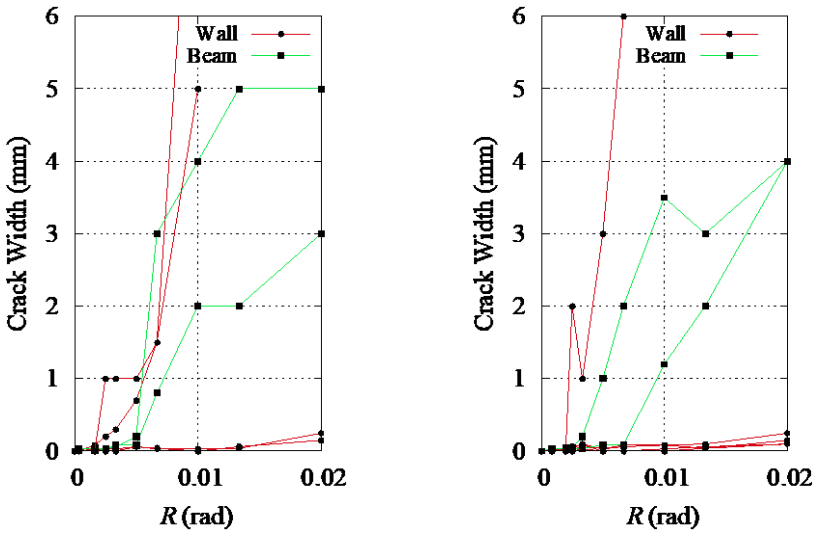

(a) (b)

Figure 4.4.5. History of residual crack width: (a) BS, (b) BSH

The cracks with similar color Figure 4.4.5 declares the dominant observed cracks of the elements of the specimens in the similar loading scenario.

Figure 4.4.6. Dominant large crack

4.4.3 Stress distributions

The stress distribution of the longitudinal reinforcement is shown in Figure 4.4.7. The stresses were determined by the strains, which were recorded using strain gauges installed at the longitudinal reinforcements as shown Figure 4.3.7 and Figure 4.3.8, assuming bilinear hysteretic stress–strain behavior for the steel reinforcing. The longitudinal reinforcement of the beam yielded in tension, while tension stresses in the wall longitudinal reinforcement for both specimens were negligible owing to the non-anchorage detailing. However, the wall longitudinal

reinforcements experienced noticeable compressive stresses. The neutral axis depth appeared to be in the boundary between the walls and the structural member.

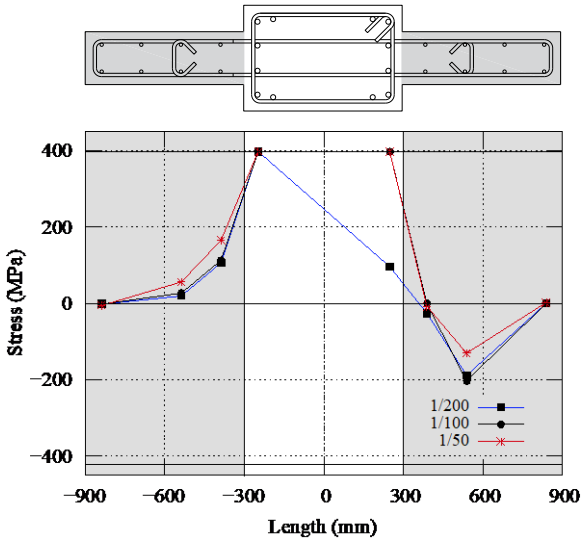

(a)

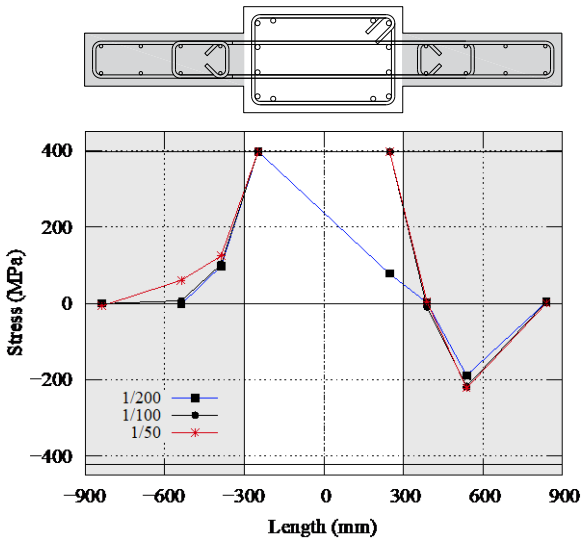

(b)

Figure 4.4.7. Stress distributions of longitudinal reinforcement: (a) BS; (b) BSH

Figure 4.4.8 shows the stress distribution of confinement reinforcement. The vertical axis represents the height of the strain gauges, and the horizontal axis represents the stress. The strain gauges were installed at the reinforcements both in-plane and out of the loading plane, as shown in Figure 4.3.8. For specimen BS, the stress at the wall boundary was compressive owing to the axial force at the concrete, as can be seen in the stress at the longitudinal wall reinforcement in Figure 4.4.7a and 8b. Thus, installation of confinement reinforcement at the wall boundary can be effective in damage restriction; however, as previously shown in Figure 4.4.1, the impact of confinement reinforcement on the strength of the element was not obvious in this study.

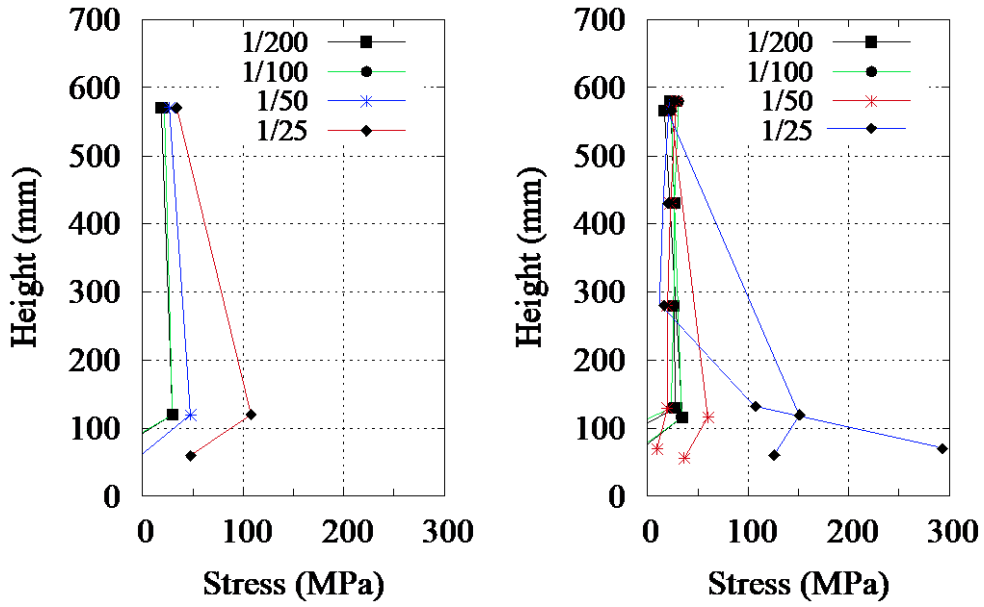

Figure 4.4.8. Stress distributions of confinement reinforcement: (a) BS, (b) BSH

4.4.4 Prediction of shear span length

Since the wall boundary of the beam specimen was connected to the wing walls, the critical cross-section was not clear. The critical cross-sections of the beam and of the non-structural walls extended to the inside of the wing wall causing cracks on the wing walls. When calculating bending moment from shear force or vice versa, shear span length should be considered.

The section where dominant horizontal cracks were observed can be considered as the critical section. However, as can be seen in Figure 4.4.4, cracks were well distributed around the beam-wing wall interface, and thus the boundary cannot be easily defined. Another way to estimate critical cross-section is by considering the drift angle and displacement. The length L′ from the loading point to the critical section, which represents shear span length, was derived by $L'=R'/\delta$ (where R′ is drift angle measured by vertical linear variable differential transformers (LVDTs) shown in Figure 4.3.5; and δ is displacement at the top of the specimen).

Figure 4.4.9 shows the relationship between estimated shear span length and drift angle in each loading direction. The dashed line represents the average of all data while the red solid horizontal line at 2160 mm was the length *L* from the loading point to the wing-wall boundary. The shear span length at smaller drift angle was varied, but it became closer to 2160 mm at 1/50 rad, where the longitudinal reinforcement yielded. The average estimated length was 2375 mm at 1/200 rad, which indicated that the shear span length was 200 mm deeper from the surface of the wing wall due to cracks on the wing walls.

The secondary analytical prediction for both specimen as shown in Figure 4.4.1, were obtained from the sectional analysis considering the average value at each respective drift of Figure 4.4.9, which was closer to the experimental result compared to the primary analytical prediction obtained using a shear length of 2160 mm.

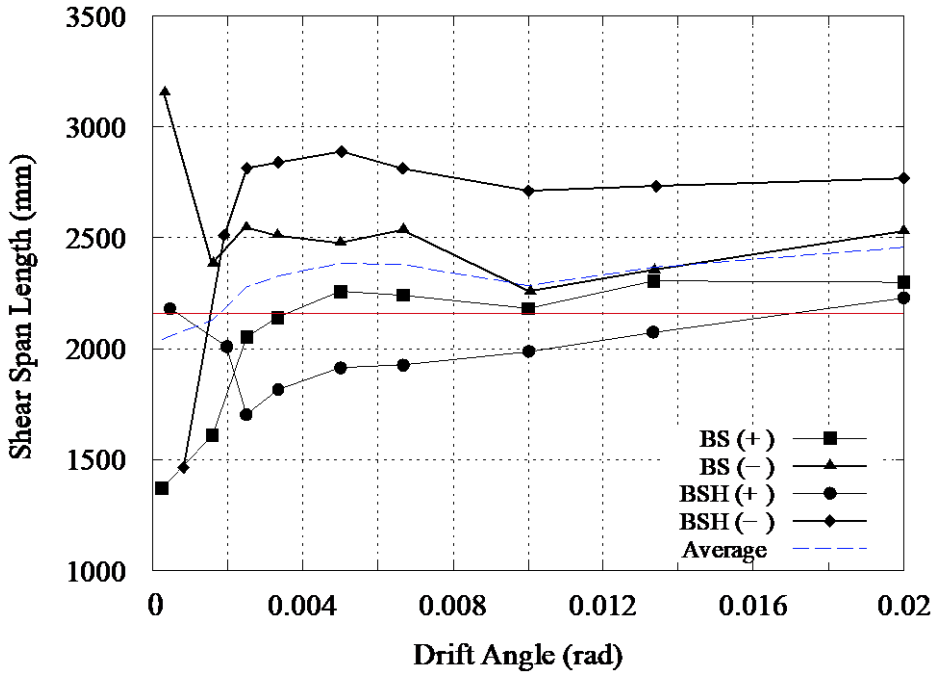

Figure 4.4.9. Shear span lengths assumed in the tests for the beam specimen

4.5 Dynamic Evaluation of the Proposed Detailing Method

The detailing method for the fabricated specimens, which were constructed based on the structural member of a real building (Figure 4.5.1), was used in the construction of an experimental three-story building. The building was tested by Japan's National Institute for Earth Science and Disaster Prevention (NIED) at the E-defense shake-table testing facility. One of the key objectives was to evaluate the performance of the proposed detailing method for hanging walls under dynamic waves in a real building, as well as to validate the new guidelines for important buildings with post-disaster functionality. While there were other objectives in the experiment, such as the performance of other non-structural elements (i.e. ceilings) and evaluation of structural health monitoring methods, these are outside the scope of this paper and will not be discussed.

4.5.1 Test specimen

The specimen was a three-story frame resisting structure with non-structural reinforced concrete wall segments, such as wing and spandrel walls, casted monotonically with structural

members (See Figure 4.5.1a). The building had two spans in the direction where shaking was applied and one span in the out-of-plane direction as shown in Figure 4.5.1b.

The columns were designated as C1 (central columns) and C2 (outer columns), both of which have the same gross cross sectional dimensions of 600 mm × 520 mm but with different reinforcing layout. The main beams parallel to the loading direction were labelled G1 and G1a (reverse of G1) with dimensions of 320 mm by 480 mm. Beams in the out-of-plane direction were G2 and G3 (280 mm × 480 mm), while the secondary beam in the in-plane direction was B1 (320 mm × 400 mm). For walls, the wing walls had dimensions of (180 mm × 480 mm) and were attached to the columns, and the hanging walls (180 mm × 400 mm), standing wall (180 mm × 880 mm) were attached to the beams as shown in Figure 4.5.2.

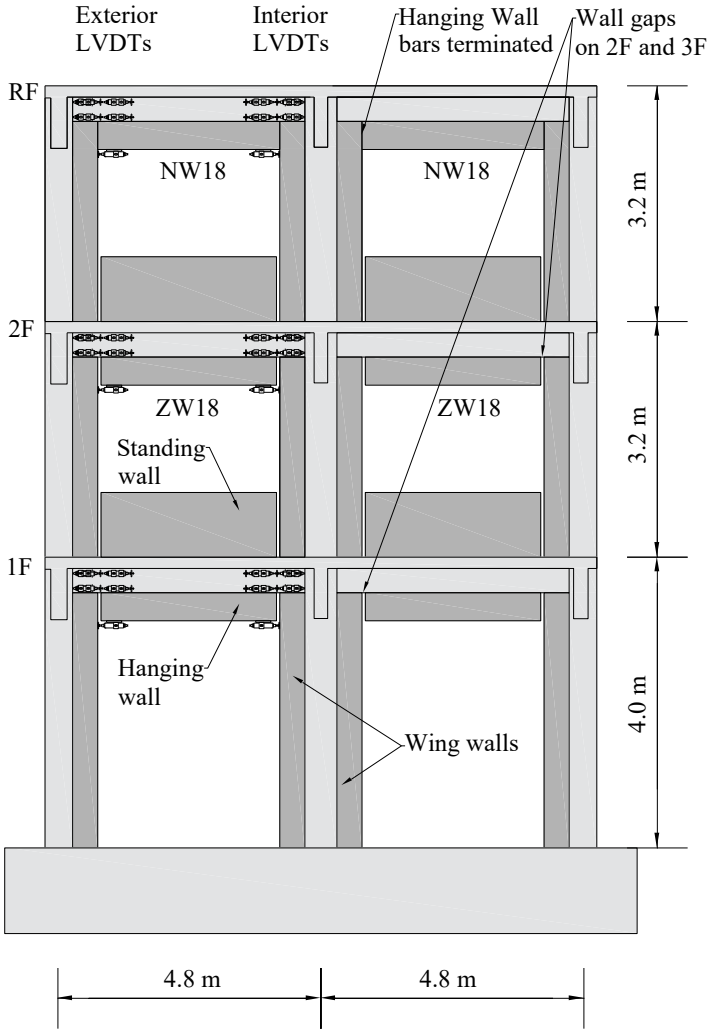

(a) In-plane view of the frame

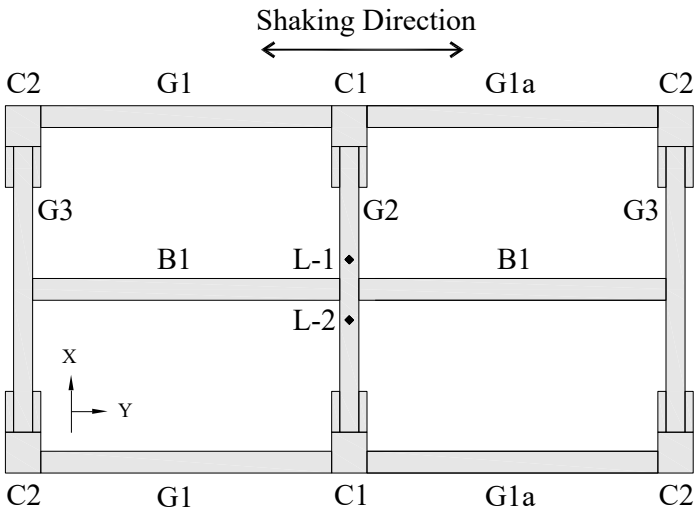

(b) Floor plane

Figure 4.5.1. E-defense specimen geometry

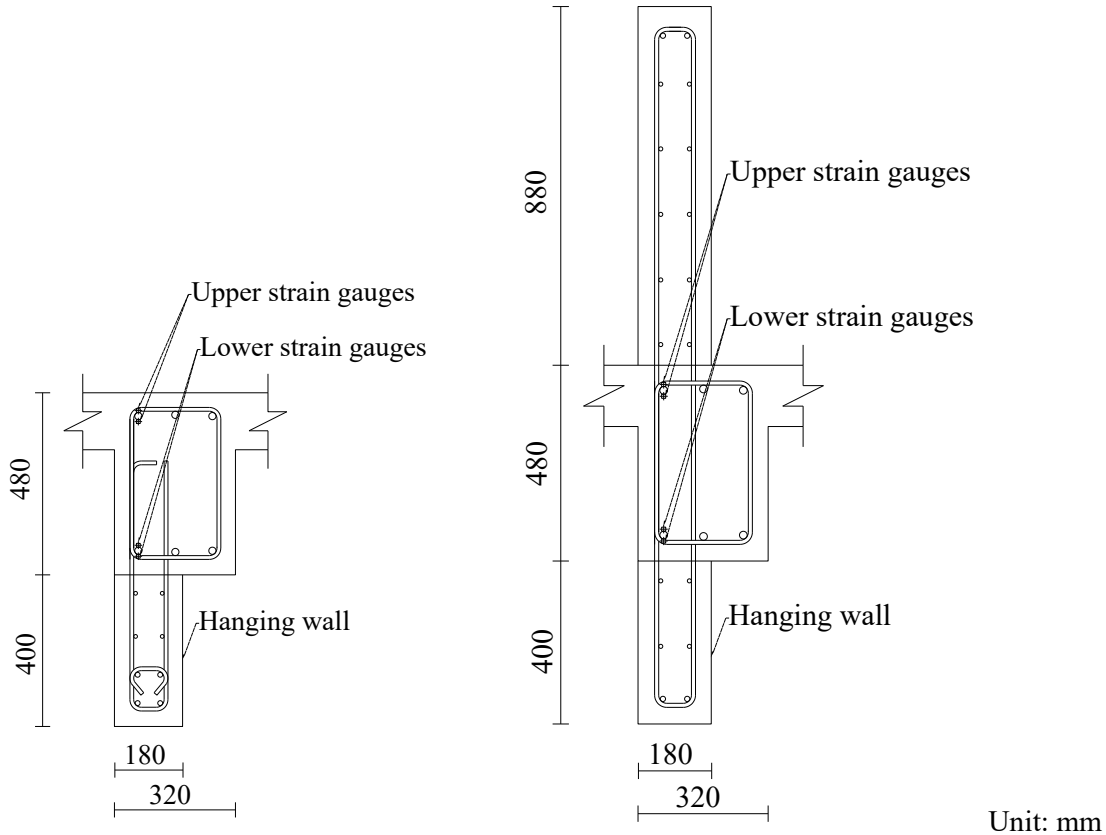

(a) (b)

Figure 4.5.2. Cross section of the beam member: (a) hanging wall (NW18); (b) hanging and standing (ZW18)

To evaluate the performance of the spandrel/hanging walls in both the existing and proposed detailing methods under shaking excitations, the walls were casted to be monolithic with structural beams with a seismic slit present at the end of these walls at the wing wall interface on the first and second floors; while on the third floor, there was no seismic slit but longitudinal reinforcing bars were not anchored, as shown in Figure 4.5.1a. The tie bars were placed at the boundary of the third floor hanging walls, as shown in Figure 4.5.2a, to inhibit buckling. Cyclic load reversals may lead to buckling of boundary longitudinal reinforcement, even in cases in which wall boundaries do not require special boundary elements. Therefore, ties are required for walls with moderate amounts of boundary longitudinal reinforcement, to inhibit buckling (ACI, 2014). A larger spacing between ties was used owing to lower deformation demands at the walls. The hanging wall reinforcement details are shown Table 4.5.1.

Table 4.5.1. Hanging walls reinforcement details

Name	Third floor	First and second floors
Type of member ($B \times D$)	Beam (320 mm × 480 mm)	
Long. reinforcement	6-D19 (SD345) ρ_g = 1.1%	
Trans. reinforcement	D10@160(SD295A) ρ_t=0.28%	
Wall type (Thickness)	Spandrel Walls (180 mm)	
Height of hanging wall	400 mm	
Height of standing walls	-	880 mm
Long. wall reinforcement	4-D13, 4-D10 (1.1%)	2-D13, 4-D10 (0.75%)
Trans. wall reinforcement	D10@160 (0.5%)	D10@160 (0.5%)

The specimen was tested by applying artificial waves five times with different scale factors over three days of testing (two on the first day, one on the second, and the final two on the third). White noise excitations were applied at the start and end of each day and between consecutive excitations (8 total) to track changes in the building's dynamic properties resulting from incurred damage during each shaking event. However, as the focus of this study is on the behavior of specific structural elements, results using white-noise excitations will not be discussed. For artificial waves, applying a scale factor 1 waves would make its response spectrum equivalent to the design spectrum used in the Japanese building code for ordinary building (AIJ, 2016). As

shown in Table 4.5.2, the first test used a scale factor of 0.2 and was performed to confirm that the building could achieve serviceability requirements for frequent shaking events. The second excitation had a scale factor of 1.0 to assess if the building would remain elastic with a peak inter-story drift of less than 0.3%, which is a requirement for buildings with post-disaster functions at code-level shaking. The third test had a scale factor of 1.5, which was representative of the design demands for buildings with post-disaster functions. This level of shaking was repeated for the fourth test to evaluate if the building was capable of withstanding an aftershock at an intensity equal to its design demand as required by the Japanese building standards. The final excitation had a scale factor of 1.6 to observe the building's performance (both structural and non-structural) against largest possible earthquake in its fully inelastic range and its capability to withstand multiple significant seismic events.

Table 4.5.2. Expected response of the building

Number of trails	Max designed acceleration	Scale factor	Expected response of the building
1	5.95 m/s^2	0.2	Serviceability should be maintained for frequent earthquakes
2		1.0	Story drift limit should be less than 0.33%.
3		1.5	Story drift limit should be less than 1.5%
4		1.5	Building should survive an aftershock of equal intensity to the main shock (1.5 times code-level for buildings with post-disaster functionality)
5		1.6	To observe performance of both structural and non-structural elements in its fully inelastic range and its capability to withstanding multiple significant seismic events.

4.5.2 Instrumentation

Different types of accelerometers, such as those shown in Fig. 4.5.3a, were installed on all floors. This was to evaluate the accuracy of cheaper sensors compared to more expensive variants and the global building performance Laser transducers (Fig. 4.5.3b) were installed at three locations on each floor to measure inter-story drift; one next to each exterior frame at the mid-width of the east-side bay and a third near the center of each floor.

The transducer and the target were attached to aluminum H sections bolted to the bottom and top slab, respectively. The center location had two transducers in parallel to capture rotation effects.

- Displacement potentiometers (Fig. 4.5.3c) were attached to the exterior of the northeast bay at column bases and joints between beams/hanging walls/standing walls and wing walls. These were also used on windows to capture window drift.
- Other instrumentation and equipment installed in the building included video cameras, strain gauges, optical fibers, wires, and 3D scanners; among others.

(a) (b) (c)

Fig. 4.5.3 – Instrumentation applied in building; (a) accelerometers, (b) laser transducers, (c) displacement potentiometers

4.5.3 Test Results

The performance of the building was evaluated through lateral drift level and its member response under the action of dynamic waves carried out on a shaking table.

Story drift was measured using laser transducers L-1 and L-2 installed at the geometrical center of every story as shown in Figure 4.5.1b, and LVDT installed at locations expected to incur more damage. LVDTs installed at the exterior wall-column showed larger story drift compared to the interior LVDTs as shown in Figure 4.5.1a, but had smaller story drift compared to the laser transducers second and third floors as shown in Table 4.5.3.

This difference might be due to the angular deviation of the beam element during shaking which could not be recorded directly by the LVDT. However, both drift and angular rotation records were comparable as shown in Figure 4.5.4. Thus, from all these measurements the maximum and minimum story drifts were found to occur in the first floor and at the top of the building, respectively.

Table 4.5.3 Story drift and angular rotation of the hanging walls

Number of stories	Story drift (%)	Beam rotation by LVDT (%)		Rotation/story drift (Exterior LVDT)	Rotation/story drift (interior LVDT)
		Exterior LVDT	Interior LVDT		
1	3.46	3.19	2.24	1.04	0.73
2	3.29	2.87	1.92	0.95	0.64
3	1.70	0.88	0.33	0.59	0.21

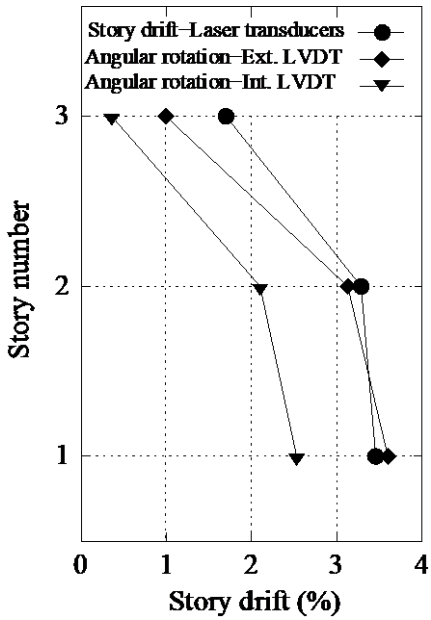

Figure 4.5.4. Story drift under the 160% design wave

Due to the high stiffness of the column/wing-wall components, the rotation angle of a beam member could be considered as being similar to the story drift angle of the same story. Hence, the ratios between the rotation angle of hanging walls and the story drifts indicate the effectiveness levels of the different types of hanging walls as shown in Table 4.5.3. When the ratio is closer to one, the angular rotation is nearly equal to the story drift level in the wall. Conversely, a smaller ratio indicates that the angular rotation of the beam is less than that of the story drift. A lower ratio of story drift to angular rotation of beam, indicates that the hanging wall is capable of restricting inelastic deformation. As can be seen in Table 4.5.3, the ratio between hanging wall rotation and

story drift was smaller in the third floor where the hanging wall was constructed based on the proposed detailing method.

Members' responses were recorded using strain gauges, which were installed at different locations in each structure member. Performance of the beam members, including hanging walls, were evaluated using average record of the upper and lower strain gauges attached at both sides of the longitudinal reinforcement as shown in Figure 4.5.2. The average of first and second floors story drift, as well as the average of second and third story drift, are used for the first and second stories beam members respectively, and the third floor story drift is used for roof floor beam member. The relationship between average drifts and strains of the beams in every story were compared and are as shown in Figure 4.5.5.

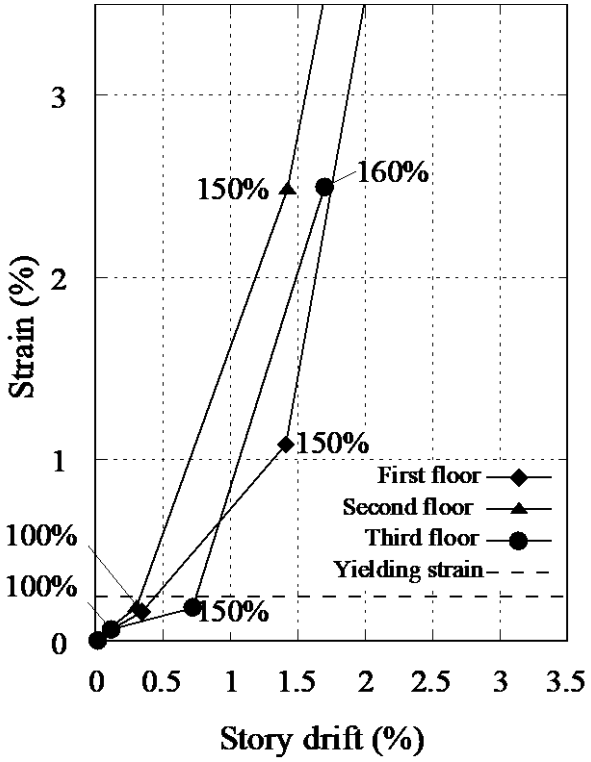

Figure 4.5.5 Comparison of the hanging walls under different earthquake waves considering story drift-strain relation

As can be seen in Figure 4.5.5a, compared to the hanging walls at the first and second floors, the hanging wall at the third floor provided higher strength to the beam, which resulted in a relatively smaller strain at higher drift before the yielding of the longitudinal reinforcement. The hanging wall with proposed method of detailing was observed at the critical zone under compression load resulted from lateral dynamic waves Likewise, it was observed that the existence of the spandrel walls in the first and second floors, could not restrict the formation of the plastic hinges in the critical zone of the beam members. This means that, the spandrel walls of the first and second floors were found to be not so effective on the member stiffness of beam

components due to presence of the seismic slit. The post yielding performances of the beams shown in Figure 4.5.5a were different from those of the pre-yielding state due to unstable strain gauge records for post-yielding state; hence, comparison with the post yielding state might not be practical.

Following the 100%, 150% (first run), and 160% excitations, damage observations and residual crack measurements were performed. Smaller crack widths were observed in the third floor compared with those in the first and second floors at similar story drifts as shown in Figure 4.5.6 . Hence, the damages and strains on hanging walls using the proposed detailing method were found to be satisfactory compared to those on hanging wall with seismic slits.

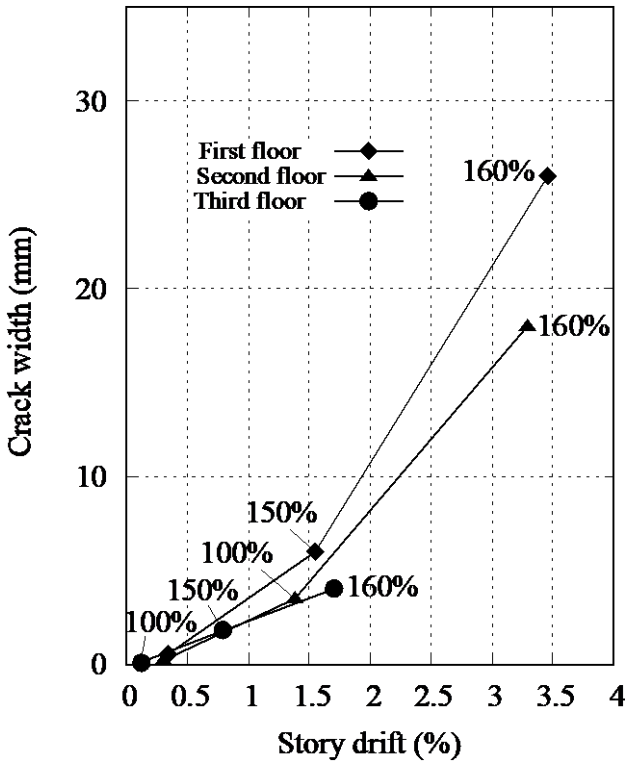

Figure 4.5.6 Comparison of the hanging walls under different earthquake waves considering story drift-crack widths relation

The beam with a hanging wall showed different damage patterns in the dynamic and static load tests. Previous studies showed that reinforced concrete elements that failed in flexure under static load could fail in shear under dynamic load (Magnusson, et al., 2010). Dynamic loads that result in different types of damages to the reinforced concrete element generally refer to waves emerging from blasting and other civil activities. Thus, the beams tested in this study experienced comparable damage patterns (Figure 4.4.4 and Figure 4.5.9c) and nearly equal cracking widths (Figure 4.4.5a, Figure 4.4.5b, and Figure 4.5.5b) under static and dynamic loads at similar drifts

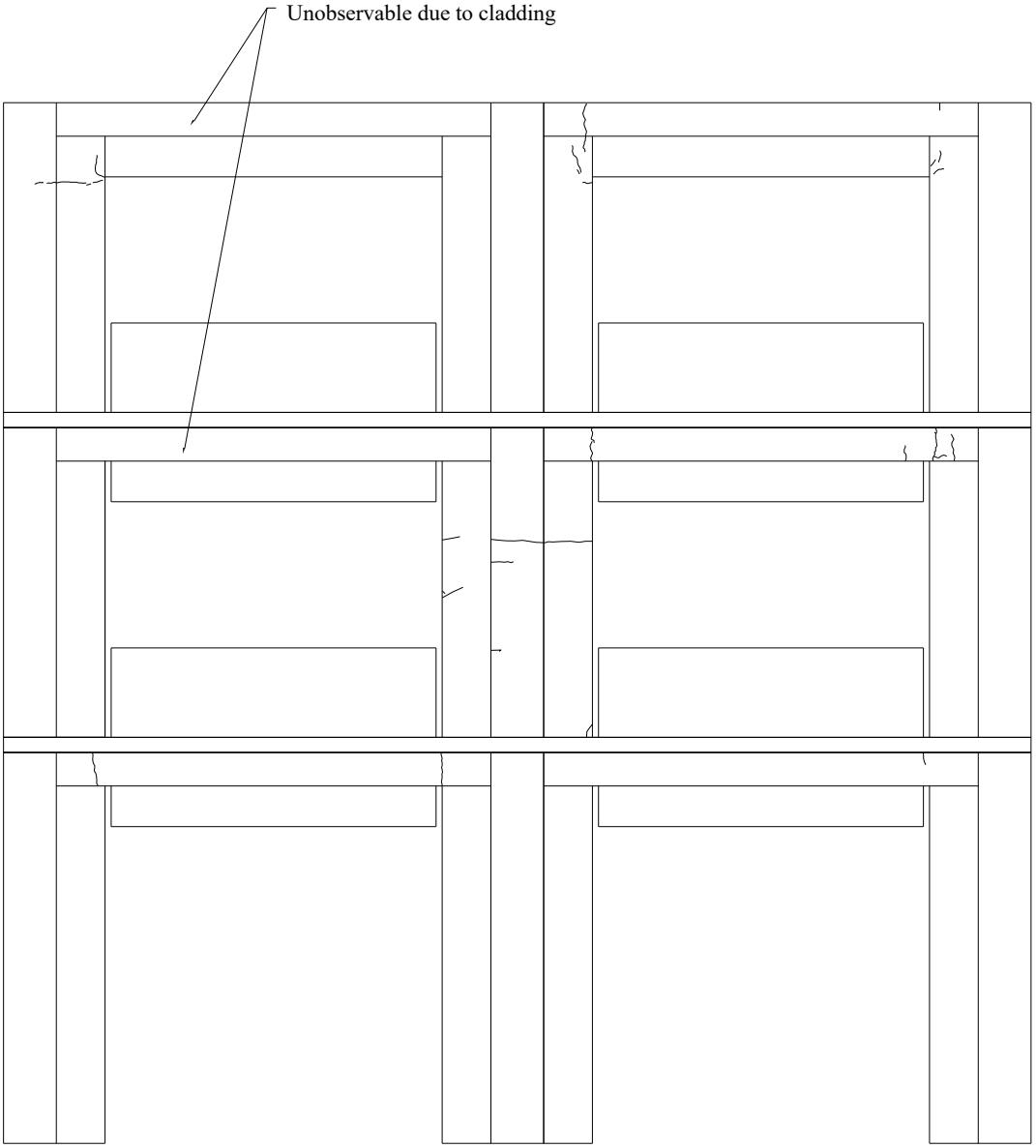

Figure 4.5.7. Damage observation of the frame at 100% of the designed waves

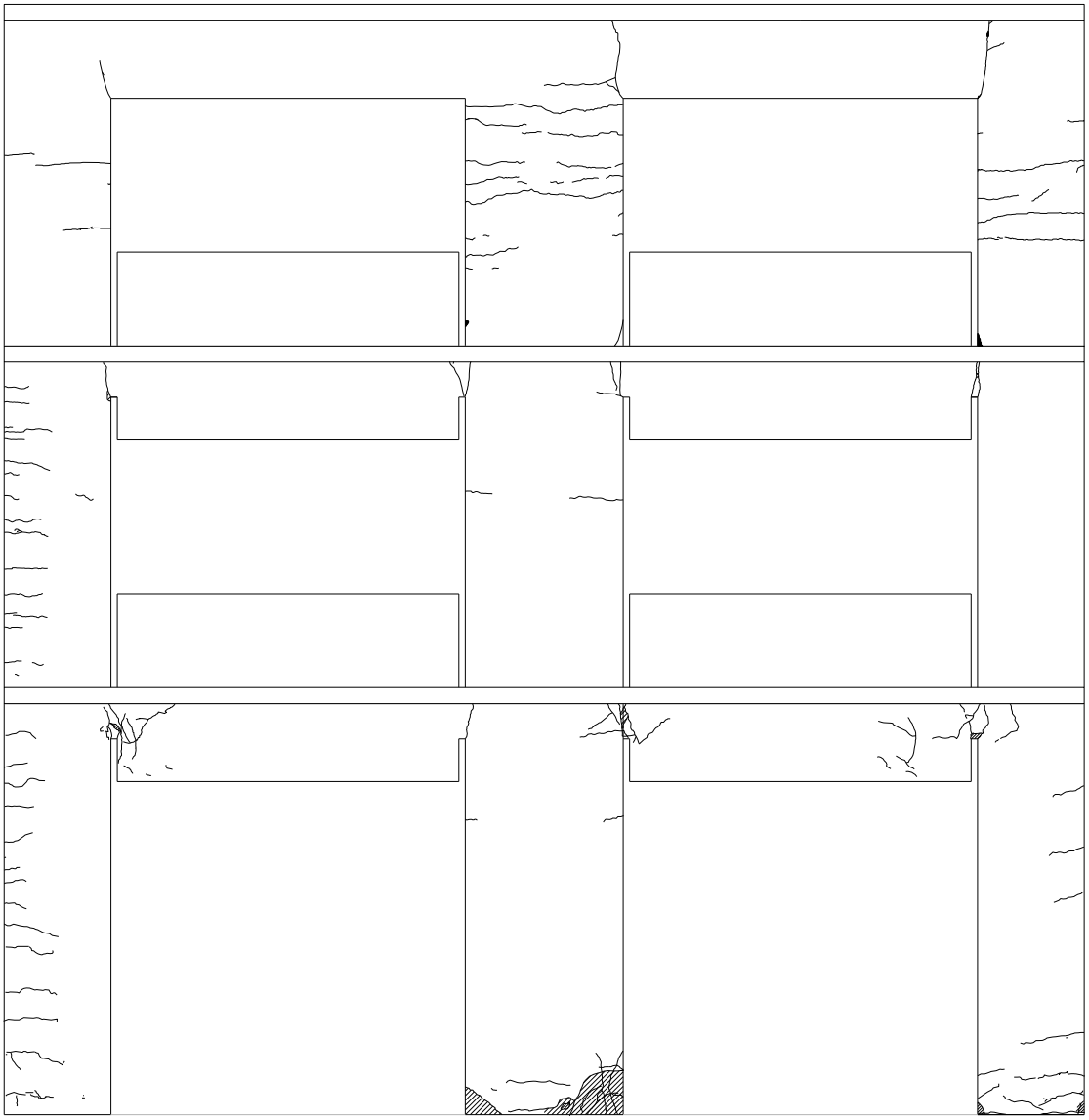

Figure 4.5.8. Damage observation of the frame at 150% of the designed waves

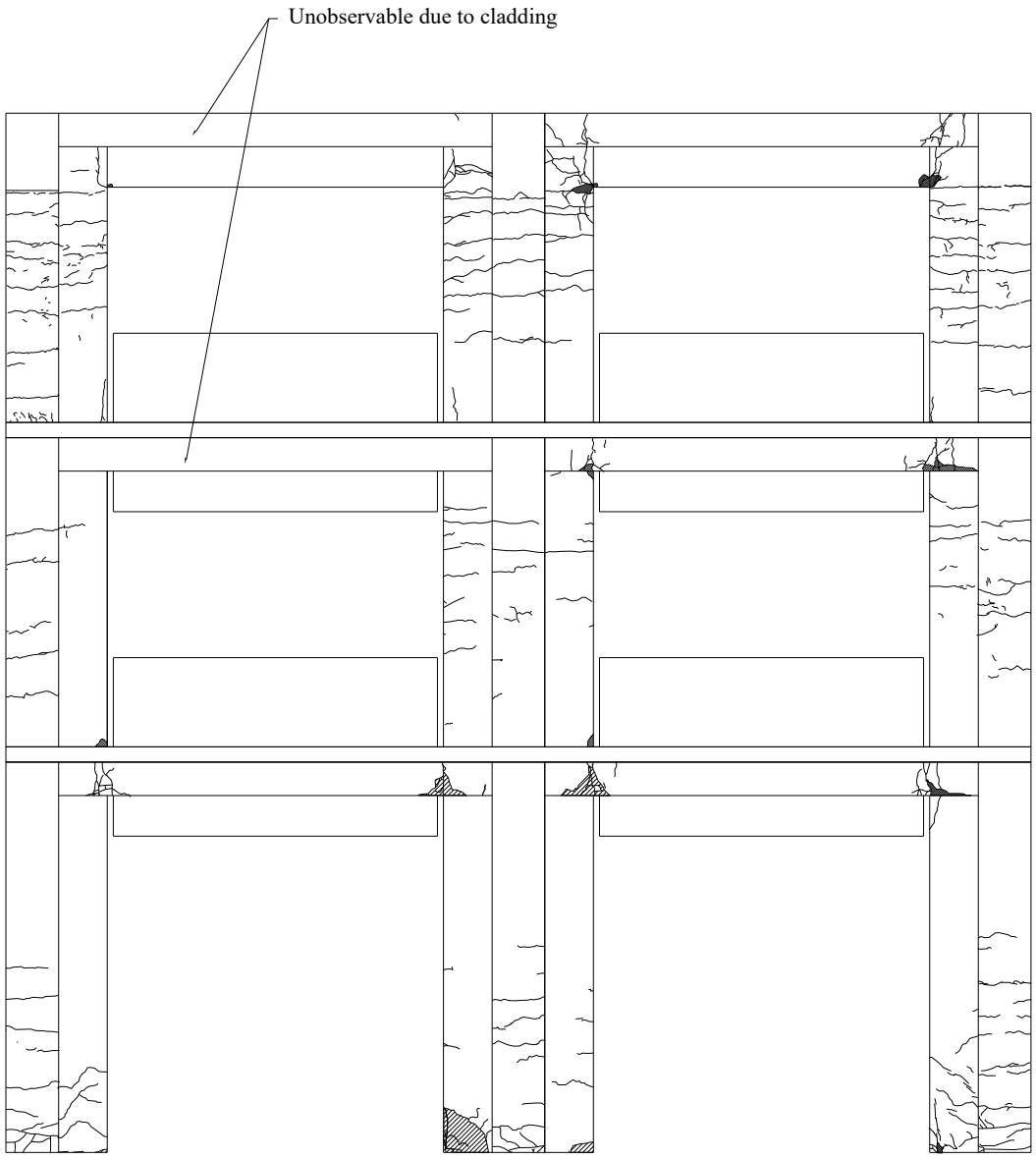

Figure 4.5.9. Damage observation of the frame at 160% of the designed waves

The observed cracking patterns for the hanging wall are shown in Figure 4.5.7, Figure 4.5.8 and Figure 4.5.9. In the first and second story, diagonal cracks in hanging walls formed and originated at the corner of the slit under 100% shaking intensity. When the first 150% shaking intensity was applied, propagation of big cracks around the slit area, as well as spalling of the concrete, occurred. When 160% of the designed wave was applied, big hinges occurred in the slit area and spalling of concrete increased. Cracking in the third floor hanging walls appeared in the wall boundary when 100% of the designed waves was applied. Although the cracks did not spread around the wall segments joint area at 150% of the designed waves, the cracks widths increased. At 160% of the designed waves, minor spalling of concrete occurred and crack widths increased. Thus, the designed waves resulted in formation of dissimilar types of cracks in hanging walls with and without slit as shown in Figure 4.5.10. As can be seen in Figure 4.5.10, noticeable cracking has been occurred on the column members of top floor, of which, most of them are superficial and does not declare any an unusual behavior.

(**a**) (**b**) (**c**)

Figure 4.5.10. Damage at hanging walls under 150% of the designed waves: (**a**) first floor; (**b**) second floor; (**c**) third floor

4.6 Summary

Past significant seismic events in Japan have induced the Japanese Building Code to increase the required design base shear and drift-limit requirements for post disaster management buildings. To satisfy these requirements, a method of reinforcement detailing for connection of a monolithic non-structural wall with structural frame was introduced in this study.

The performance of non-structural hanging wall, which was built according to the proposed method of detailing, were experimentally validated under the static and dynamic loads to develop non-structure walls system that could increase performance of buildings and their capability for continuous use during future aftershocks.

The load-drift angle relationship of beam having non-structural hanging walls and non-anchorage of the longitudinal reinforcement demonstrated high deformability during cyclic loading

test. However, the relationship, was not affected by the difference in the amount of confinement reinforcement. A large dominant crack formed at the wall boundary of non-structural wall having non-anchorage of the longitudinal reinforcement during the cyclic loading test; however, large strength degradation was not observed in horizontal load versus drift angle relationship for the range of drifts considered (up to 1/25).

The shaking table test results indicated that beam members with non-structural hanging walls based on the AIJ standard were more vulnerable during artificial earthquakes compared to other structural members. The responses of hanging walls on damage level and strain in a beam under artificial earthquakes using the proposed detailing method was found satisfactory compared to hanging walls with seismic slits.

Finally, the impact of confinement reinforcement was not obvious in the static test results; however, further investigation of compatibility of different detailing with confinements and concrete, as well as amount of reinforcement along with detailing of longitudinal reinforcement, may explore the details.

Chapter V

Theoretical Shear Strength Prediction of Reinforced Concrete Members Subjected Axial Load

5.1 Introduction

It was expressed in section (1.3.2 that a beam member having spandrel wall at one side either as hanging or standing walls, may fail in the shear (Nayuko, et al., 2015), The shear failure occurs at the boundary of beam due to action of higher flexural strength resulting from the spandrel wall.

The shear failure aspect of the beam with spandrel requires to be observed in the design phase. Currently there is no generally accepted method of shear strength observation for beam member; however, traditionally, shear strength prediction is performed differently on members according to the shear reinforcement. The shear strength observation of reinforced concrete members has been one of the fact-finding topic and therefore numerous researches have been launched (Nielsen et al., 1978; Vecchio et al., 1986; Bentz, et al., 2006). Several well-established theories based on equilibrium considerations can be applied when shear reinforcement is provided, leading to safe design solutions. On the other hand, the actual shear failure mechanism cannot be demonstrated by these approaches and the shear strength is often estimated too conservatively.

As a solution for that issue, Muttoni et al. (2008) and Zhang et al. (2016) have investigated the shear strength of reinforced concrete members without stirrups based on a critical shear crack. It is realized that recently developed methods are restricted to the certain condition and property of material and cannot be directly applied to new technology. Therefore, a method is desired for the prediction of shear strength to have applicability over all conditions based on rational shear failure mechanism.

The equation proposed by Ohno and Arakawa (Ohno, et al., 1960) is considered to be an accurate method for shear strength prediction of members having non-structural wall in Japanese standards. Likewise, the formulas obtained based on the truss and arch mechanism of shear stress transformation, is used to theoretically predict the shear strength of beam member; however, these formulas do not consider impact of axial load. Considering stress condition of the beam with spandrel walls, the beam is subjected to axial load. Therefore, the shear strength subjected to axial load cannot be estimated theoretically based on current design standard. Accordingly, it is

necessary to investigate theoretical shear strength prediction method for beams subjected to axial load.

In this chapter it is attempted to propose an equation for shear prediction of beam with spandrel wall, designed according to the proposed method of detailing of spandrel wall connection discussed in chapter II. Moreover, to observe the applicability of Mohr-Coulomb theory on shear prediction of concrete member using an experimental approach.

5.2 Shear Strength Prediction of Beam with Spandrel

As explained in section 4.4.1, the shear strength capacity of a beam with spandrel can be reasonably well estimated by performing cross-sectional analysis considering force equilibrium. The proposed method of spandrel wall connection with the frame or adjacent member (Sec 4.2) suggests non-anchorage of longitudinal reinforcement, therefore the calculation should be easy enough to estimate shear strength due to existence of the only tensile stresses of the longitudinal reinforcements in tensile zone and the axial load. In order to reach out to an easy Equation for shear strength prediction of a beam having spandrels, experimental data of tested specimen in sec 4.3.1 is used.

To simplify the approach, it can be assumed that all the longitudinal reinforcements yielded at the maximum load as shown in Figure 5.2.1. The tensile force T by all the longitudinal reinforcements and the axial load P were assumed at the center of the gross member area. The compression force, C, was the sum of the tensile force of the longitudinal reinforcement combined, T, and the member axial load.

The neutral axis depth, c, was calculated using Equation (5.2.1), which assumes that c was less than the depth of the wall and that the concrete stress block had a depth of $0.85f'_c$. The compression force C acted at the center of the stress block. The bending moment around the center of the member was given by Equation (5.2.2) . It should be noted that the longitudinal wall reinforcement was not considered in the calculation for both tension and compression and the concrete was neglected in the calculation for tension.

$$c = \frac{C}{0.85 f'_c b_w} \tag{5.2.1}$$

$$M = C \cdot \left(\frac{D}{2} + D_w - \frac{c}{2} \right) \tag{5.2.2}$$

b_w: Thickness of the wall

M : Moment capacity of the section

D : Depth of structural member

D_w : The length of the wall

b_w: Thickness of the wall

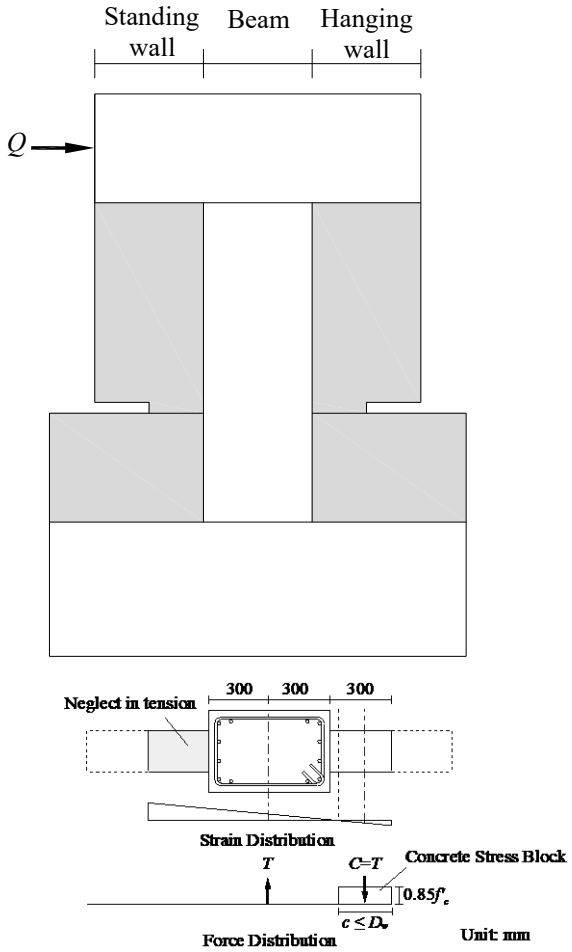

Figure 5.2.1. Schematic diagram of the forces on the cross-section

Table 5.2.1. Prediction of shear strength

Property	Specimen	
	BS	BSH
Maximum horizontal load from test	313 kN	285 kN
Predicted shear force by cross-sectional analysis (Bending moment)	301 kN (651 kN·m)	301 kN (651 kN·m)
Tension force T	1367 kN	
Compression force C	1367 kN	

Neutral axis depth c	268 mm	288 mm
Predicted shear force by Equation (5.2.2)	295 kN	289 kN
(Bending moment)	(637 kN·m)	(623 ·m)

Table 5.2.1 shows the horizontal load-carrying capacity predicted using cross-sectional analysis and Equation (5.2.2). As shown in Table 5.2.1, the predicted neutral axis depth nearly corresponded to what is shown in Figure 5.2.1. The shear force was calculated using the moment and the shear span length, *L*. The prediction from the cross-sectional analysis underestimated the maximum horizontal load for the BS, but overestimated that for the specimen BSH. The prediction from Equation (5.2.2) was either identical or nearly identical to that from the cross-sectional analysis for the column and the beam.

5.3 Shear Strength Prediction of Column Using Mohr-Coulomb Theory

A shear strength prediction of reinforced concrete members with Mohr-Coulomb criterion has been proposed by (Pujol, et al. 2016). When the Mohr circle's stress reaches the criterion internally, shear stress is given as shown in Figure 2.3.1.

The Mohr-Coulomb theory is a mathematical model describing the response of brittle materials such as concrete, or rubble piles, to shear stress as well as normal stress. The Mohr-Coulomb theory express correlation between normal and shear stress along with failure load and angle of friction. Coulomb's friction hypothesis is utilized to determine the combination of shear and normal stress that will cause a fracture of concrete. Mohr's circle is used to clarify which principal stresses will produce this combination of shear and normal stress, and the angle of the plane in which this will occur. The Mohr-Coulomb failure criterion represents the linear envelope that is obtained from a plot of the shear strength of concrete τ versus the applied normal stress σ. This relation is expressed as:

$$\tau = k_1 f_c' + k_2 \sigma \tag{5.3.1}$$

where k_1 and k_2 are the coefficient pertaining to cohesion and internal friction angle of concrete. (Pujol, et al. 2016) has suggested the following Mohr-Coulomb criteria as the failure envelope;

$$\tau = 0.17 f_c' + 0.75\sigma \tag{5.3.2}$$

$$\sigma \leq f_t \tag{5.3.3}$$

where f_t is the tensile stress of concrete.

The ultimate shear strength given by Mohr-Coulomb criterion has a valid theoretical bases, but the proposed theory is not proven with actual concrete stress and the stress condition inside of a member subjected to axial and horizontal loads. Furthermore, (Pujol, et al. 2016) suggests that the proposed procedure may be too conservative for a column having axial load ratio of larger than 0.4 and small amounts of transverse reinforcements. Those conditions are not considered generally for ductile members; however, when it happens the members may show unexpected failure. Therefore, it is important to consider the mechanism of the failure of the members.

Hibino, et al. (2017) has tried to propose a method to predict the strength of concrete with Mohr-circle but the circles exceed tensile limit before reaching to maximum stress and therefore the strength could not be evaluated correctly. He also declared that Mohr circle can be used for prediction of diagonal tension failure strength but the circle cannot be evaluated.

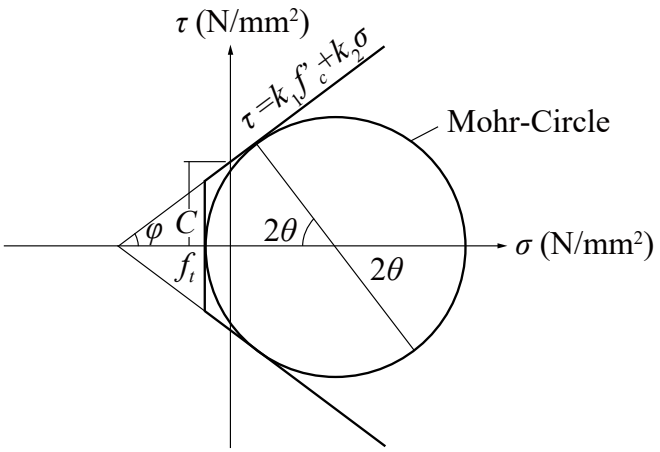

Figure 5.3.1. Mohr-Coulomb criterion

In this paper, it is attempted to investigate those Mohr-circles, restricted in the specified boundary of tensile stress and forming failure criteria which based on that correlation between shear and normal strength of the element is modified. To this end, Mohr circles were investigated considering all steps of cyclic loading until fracture, particularly on the step shear crack occurred. Mohr circles which based on that Mohr-coulomb failure criteria for each series of specimen is modified, are observed for different strain gages, installed inside series of specimen.

Concrete strength in the concrete core section at ultimate state was evaluated. Predicted Mohr stress circles drawn by measured strain depending on the axial load ratio and concrete strength. The combination of large number of circles, evolved from corresponding steps pertaining to the modified strain gage of each specimen, could lead us to find out circles which could reveal the real status inside the concrete as well as fracture limit. Furthermore, the combination of the circles simulates graphical correlation between shear and normal strength and Mohr-Coulomb failure criteria which relatively restate coefficients for Equation according to experimental records.

5.3.1 Test specimens

Three series of specimens, R1; R2 and R3, were designed to investigate internal strength status and failure criteria of brittle reinforced concrete beam that has small amounts of transverse reinforcements as shown in Table 4.3.3. Geometric properties were the same in all specimens: the cross section is 120mm×200mm; shear span length is 600mm; and shear span-to-depth ratio is 1.5. Concrete strength and magnitude of axial load were selected as the parameters. The configuration of the specimen is shown in Figure 5.3.2. The high strength steel bars, K13 were used as longitudinal reinforcement and concrete strength f'_c, 60MPa and 80MPa were used (properties are shown in

Table 5.3.2, Table 5.3.3). The transverse reinforcement ratio was arranged so that the column demonstrates brittle shear failure. Bi-directional double-curvature cyclic loadings were applied to the specimen under constant axial load N_u that simulates gravity load with specified magnitude: N_u/bhf'_c=0; 0.2; and 0.3.

Table 5.3.1. Specimen properties

Series	Specimen	b (mm)	d (mm)	L (mm)	M/Vd	f'_c (MPa)	Longitudinal reinforcement	Shear reinforcement	N_u/bdf'_c
R1	R1-0	120	200	600	1.5	80	4-K13 (ρ_t=1.17%)	D6@260 (SD295A)	0
	R1-2								0.2
	R1-3								0.3
R2	R2-0							D4@100 (SD295A)	0
	R2-2								0.2
	R2-3								0.3
R3	R3-0					60		D6. D4@50 (SD295A)	0
	R3-2								0.2
	R3-3								0.3

where b, d, L are width, depth and length of the beam respectively.
M/Vd shows shear span to depth ratio.

Table 5.3.2. Steel properties

	Strength	Yield strength (MPa)	Yield strain (μ)	Tensile strength f_t (MPa)
K13	KW785	859	6339	1042
D6	SD295A	370	3370	549
D4	SD295A	376	3389	529

Table 5.3.3. Concrete properties

Series	Compressive strength, f'_c (MPa)	Tensile strength, f_t (MPa)	Modulus of elasticity (GPa)
R1	82.7	5.47	44.9
R2	76.03	5.33	43.6
R3	72.71	5.49	45

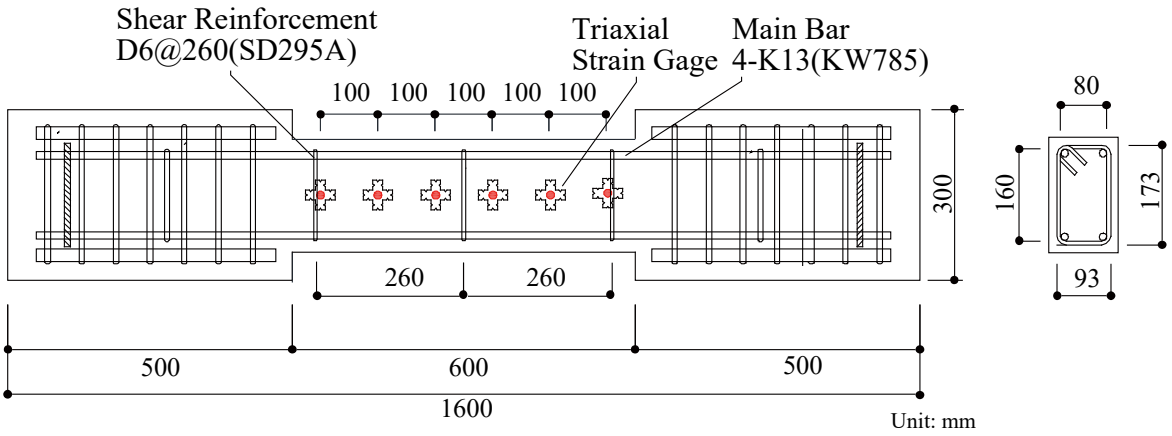

Figure 5.3.2. Configuration of specimens

The loading program was controlled by drift angle *R,* which is given by the relative lateral displacement of column divided by its height *L*. The target drift ratio was ±0.125%×2, ±0.25%×2, ±0.5%×2, ±1%×2, ±1.5%×2, and ±2%×2. To measure the strain and relative strength condition of concrete, acrylic bars furnished with triaxial strain gages, were placed in the core section of columns, as shown in Figure 5.3.3. The acrylic bars have serrated configuration to improve

bonding performance with concrete. The positon of the triaxial strain gages (SG-1 to SG-6) are shown in Figure 5.3.2.

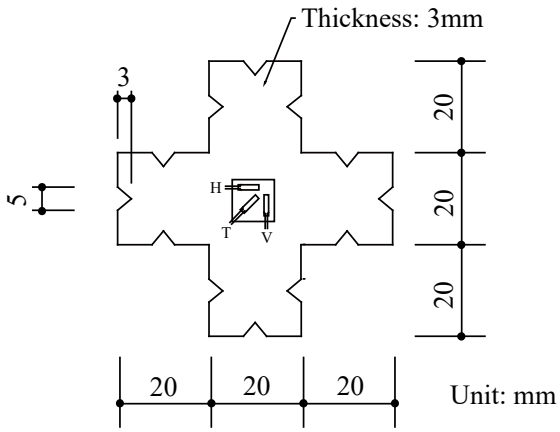

Figure 5.3.3. Shape of triaxle strain gauge

5.3.2 Experimental Results

The load deflection response of the specimens is shown in Figure 5.3.4. The maximum lateral load increases with the increase of axial load ratio and concrete strength. The lateral load after the maximum point drastically decreased due to the shear failure for all the specimens and all the specimens demonstrated brittle failure.

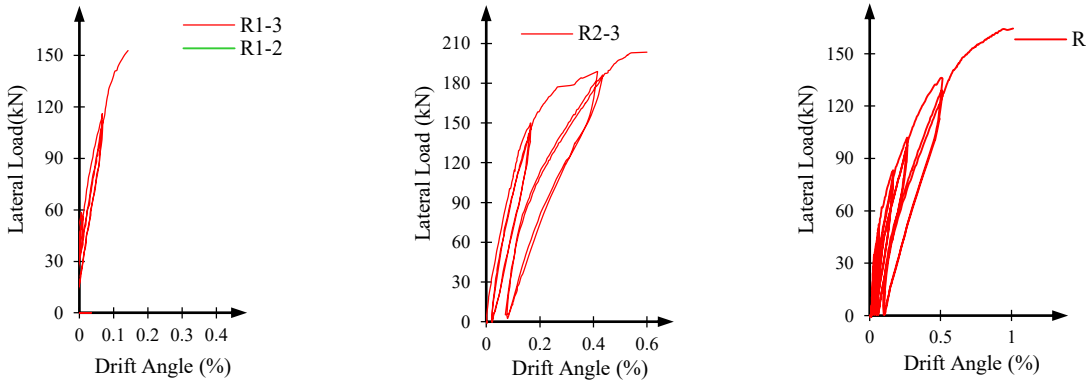

(a) R1 series (b) R2 series (c) R3 series

Figure 5.3.4. Lateral load-drift relationship

The maximum observed lateral load Q_{max} and the nominal analytical shear stength is shown in Table 5.3.4 . The nominal cpacity of the specimenes are obsereved using (ACI318, 2014) provissions. The following equations were used to anlayze the nominal shear strength of specimens;

$$V_n = V_{st} + V_c \tag{5.3.4}$$

$$V_{st} = \frac{A_v f_y \, s}{d} \tag{5.3.5}$$

$$V_c = \frac{1}{6}\left(1 + 0.07\,\frac{N_u}{A_g}\right) \sqrt{f_c'}\; b\, d \tag{5.3.6}$$

Where:

V_n: is the nominal shear strength

V_{st} : is the shear strength of transverse reinforcement

V_c : is the shear strength of concrete which can be determined by different formula, generally in case of non-prestressed concrete with axial compression Equation (5.3.6) is used.

A_v : is the shear reinforcement (two bar areas for U-stirrup)

N_u: is a compressive axial load in MPa

s: is the spacing between stirrups in a direction parallel to the axis of the member

f_c' and f_y: are tensile and compressive strength of steel and concrete respectively.

The observed crack patterns are shown in Figure 5.3.5. Diagonal wide cracks were observed and similar cracks occurred in all the specimens. This procedure is based on the assumption that if shear crack strength V_{cr} is larger than ultimate shear strength V_u, the shear crack strength governs the maximum strength. The shear crack strength V_{cr} derived from the theoretical model are given by Equation (5.3.7), as shown in Table 5.3.4.

$$V_{cr} = \frac{bd}{1.5}\sqrt{f_t^2 + \frac{f_t N_u}{bd}} \tag{5.3.7}$$

For all specimens, diagonal shear crack appeared with drastic shear deterioration, the observed failure type was therefore diagonal tension (DT) failure. DT failure is evaluated because shear crack strength V_{cr} shown in Table 5.3.4 are larger than computed shear strength V_n.

Figure 5.3.6 shows the comparison of experimental results $Q_{\max}$, V_{cr} and V_n. The shear crack strength V_{cr} overestimates measured shear strength for all the specimens and the shear strength V_u underestimates the shear strength. This disagreement between computed and measured shear strength suggests that DT failure can be determined by neither tension failure of concrete assumed in the shear crack strength V_{cr} nor compression failure of concrete assumed in the nominal shear strength V_n.

Table 5.3.4. Strength and failure type of specimen

Specimen		Q_{max} (kN)	V_{cr} (kN)	V_n (kN)
	R1-0	71	88	42
R1	R1-2	84	255	76
	R1-3	183	320	99
	R2-0	91	86	43
R2	R2-2	121	255	74
	R2-3	204	309	91
	R3-0	65	88	58
R3	R3-2	164	222	63
	R3-3	188	310	88

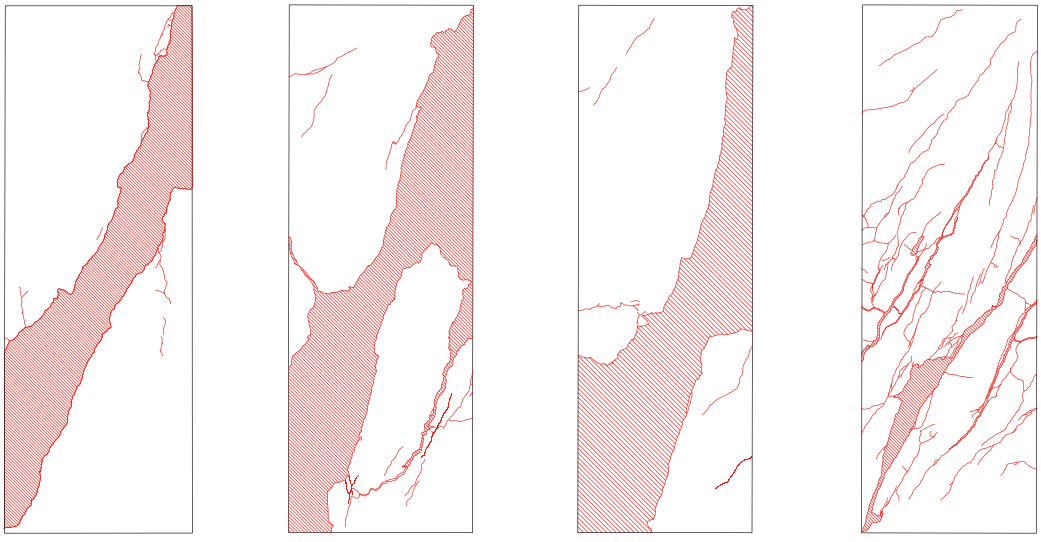

(a) R1-2 (b) R1-3 (c) R2-3 (d) R3-1

Figure 5.3.5. Crack drawings

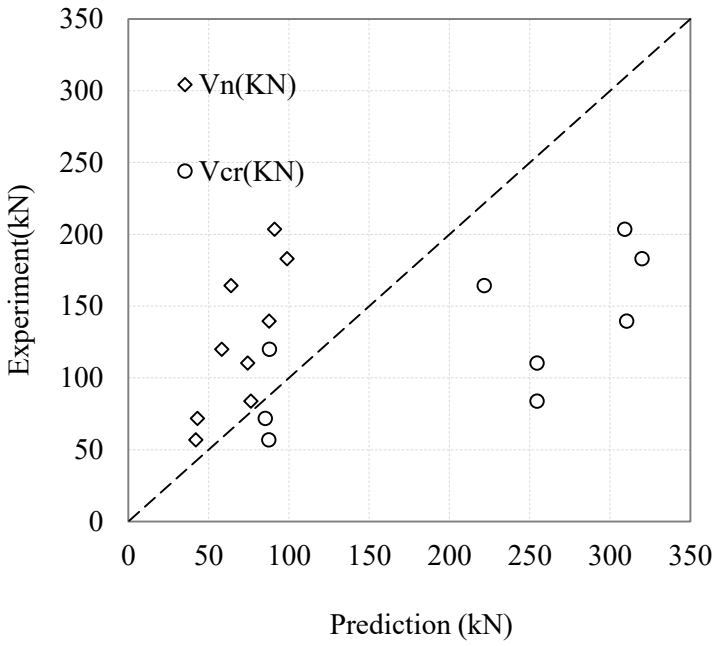

Figure 5.3.6. Comparison Q_{max}, V_{cr} and V_u

5.3.3 Mohr-Coulomb Failure Envelope

The Mohr-Coulomb criteria is defined as the tangential line to those Mohr circles which have maximum diameter corresponding modified limit. Mohr circles are plotted for each step of cyclic loading corresponding to σ_{max} and σ_{min}, created inside the specimen. Based on experimental records for each specimen, step corresponding failure of specimen are considered as a margin of strains and strengths.

In order to recognize any ambiguous step which may have been recorded by slipped strain gages prior to reaching the cracking boundary, all data taken from strain gages are read subtly. Mohr circles are plotted based on concrete strain, resulted inside the specimen from every step of cyclic loading until the shear crack is occured. If any of these plotted circles crsse the tensile limte, dominated by the Equation (5.3.8) and shown in Figure 5.3.1, the step is neglected and considered as a tensile boundary for remaining data.

$$f_t = \frac{1}{12}\sqrt{f'_c} \tag{5.3.8}$$

Mohr circles are investigated using Rosette analysies for each step of cyclic loading until cracking.

According to Rosette analysies, the maximum principal stress σ_{max} and minimum stress σ_{min} of core concrete measured by triaxial strain gages are derived by the following equations.

$$\sigma_{max} = \frac{E_c}{1-\nu^2}(\epsilon_{max} + \nu\epsilon_{min}) \quad (5.3.9)$$

$$\sigma_{min} = \frac{E_c}{1-\nu^2}(\epsilon_{min} + \nu\epsilon_{max}) \quad (5.3.10)$$

Where:

ϵ_{max}: is the maximum principal strain

εmin : is the minimum principal strain

ν: is the Poisson's ratio (=0.2).

The principal strains were calculated by measured strains using Rosette analysis. Note that stress-strain characteristic of concrete was idealized by elastic perfectly plastic approximation. Mohr circles are plotted for each steps of cyclic loading of each strain gage separately as shown in Figure 5.3.7; this is to separate real recorded strain of concrete form combined recorded strain comprised of strain of acrylic bars and strains owing to gage sliding.

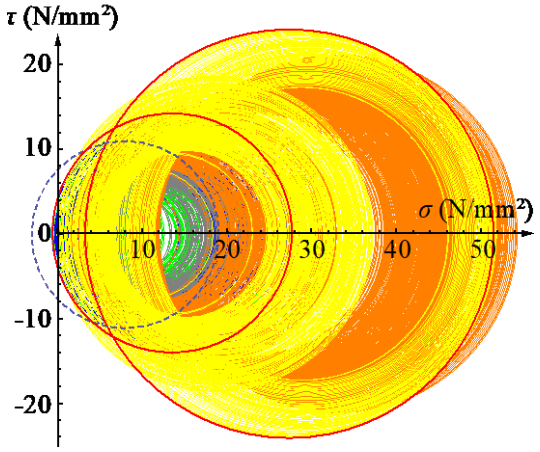

(a) R1-3

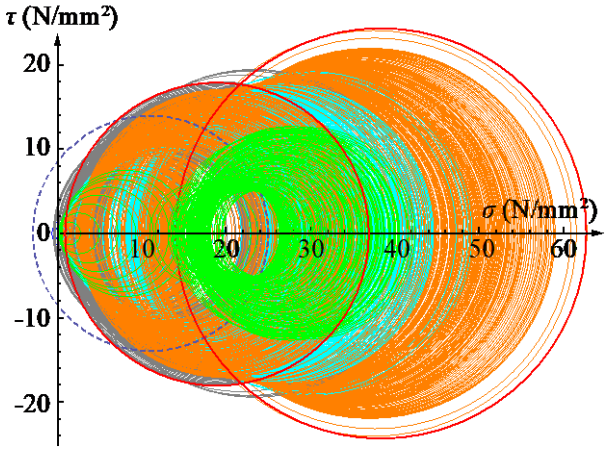

(b) R2-3

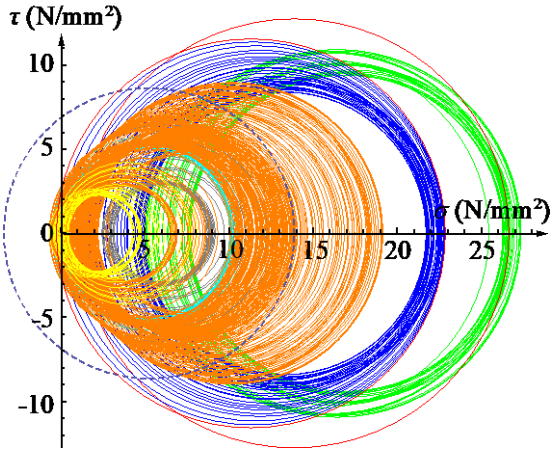

(c) R3-2

Figure 5.3.7. Set of Mohr circles combined from all strain gages of series

Mohr circles derived through this process are combined together to simulate a Mohr-Coulombs failure envelope as shown in Figure 5.3.8. Those series which have experienced short drift until peak loading manifest the critical status of concrete strength.

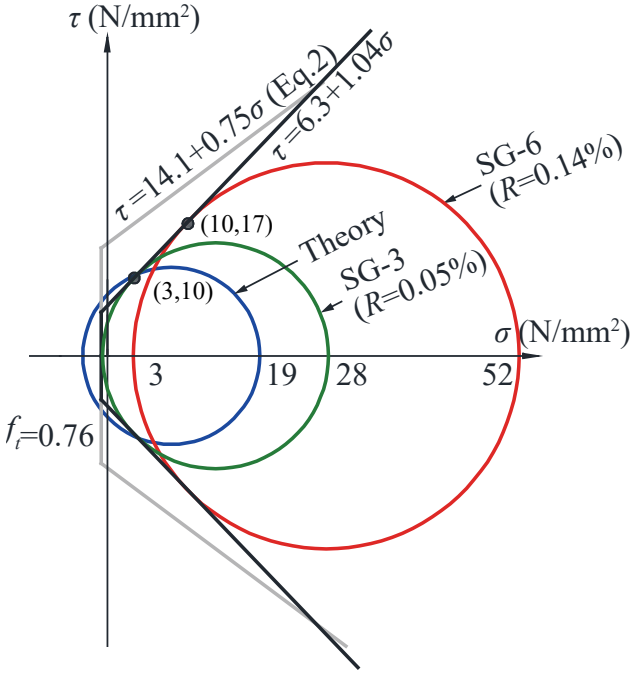

(a) R1-3

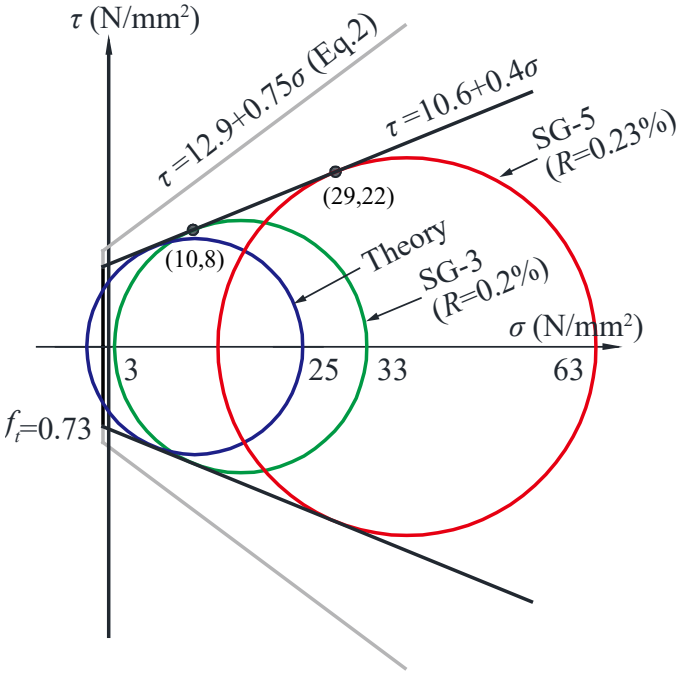

(b) R2-3

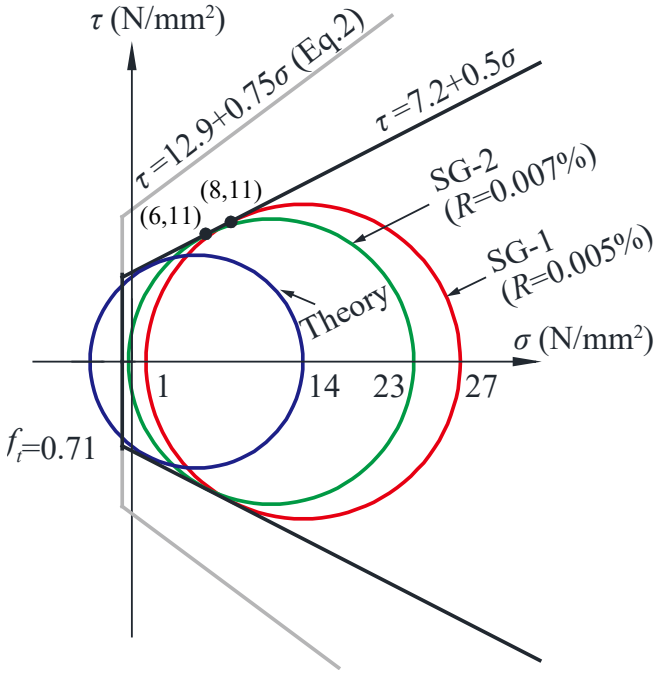

(c) R3-2

Figure 5.3.8. Mohr-Coulomb failure criteria of series

Some of the tested specimen shown in Figure 5.3.8 was realized that experienced relatively lower drift until maximum cyclic loading. The may rise question about the validity of the observed internal stress and requires anlatyical confirmation.

Blue dashed circles in Figure 5.3.8 illustrates the strength condition of concrete which is computed based on the analytical Equation of shear τ_{xy} and normal stress σ_x of equations (5.3.11) and (5.3.12) for maximum observed load.

$$\sigma_x = \frac{N_u}{bd} \tag{5.3.11}$$

$$\tau_{xy} = \frac{Q}{bd} \tag{5.3.12}$$

where N_u and Q are maximum applied axial and shear load corresponding failure of specimen.

Mohr stress circles resulting from the theoretical analysis are smaller compared to the largest circle of concrete stress, resulting from experiment data. The largest stress circles (red circles in Figure 5.3.8) show the cracking shear stress of concrete.

The difference between theoretical and experimental based Mohr circles expresses variation of acting shear force through every concrete fiber. This shows that Equations (5.3.11) and (5.3.12) can be used to observe the concrete status in a complimentary status rather than critical condition. Mohr circles which predict largest strength capacity of each series (red circles) are selected for recognition of Mohr-Coulomb failure envelope in Figure 5.3.8.

The Mohr-coulomb criterion illustrated in Figure 5.3.8 suggests that angle of fracture as well as correlation of shear and normal strength are not constant for all of the specimen but is a function of different parameters such as drift angle, concrete compressive strength, failure type, axial load and shear web reinforcement. Specimen series R1-3 addressed the above mentioned assumption.

On the other hand, Mohr circles resulted from mentioned series either crossed from concrete tensile strength in Equation (5.3.8) in the early steps or simulate retrogress failure envelope as shwon in Figure 5.3.9. Therefore shear and normal strength fracture criterion for experimental and Equation (5.3.2) based result is compared, as shown in Figure 5.3.9. Correlation between shear and normal strength is suggested for R1-3, R1-2, R2-3, R3-2 series as shown in Figure 5.3.10 and compared with Equation (5.3.2). Some of the modified equations cross the Equation (5.3.2) criterion at high stress condition.

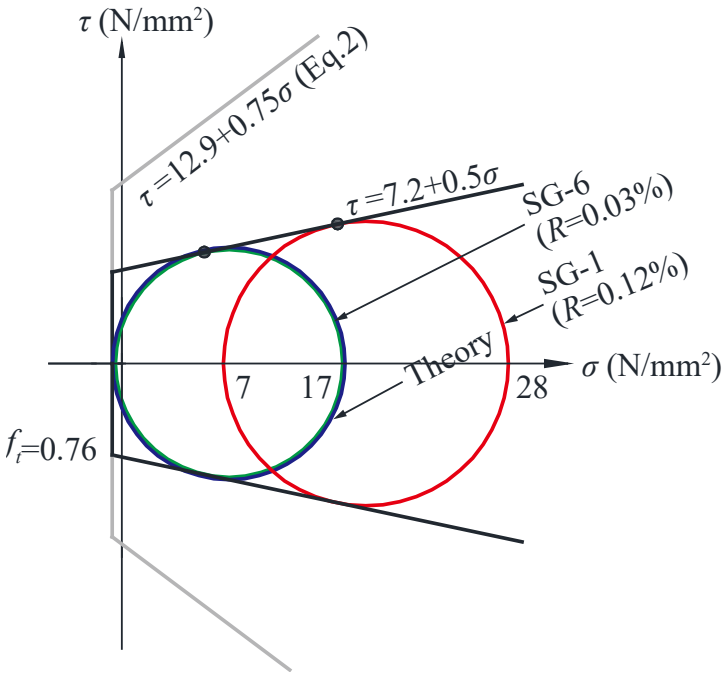

Figure 5.3.9. Mohr-Coulomb failure envelope (R1-2)

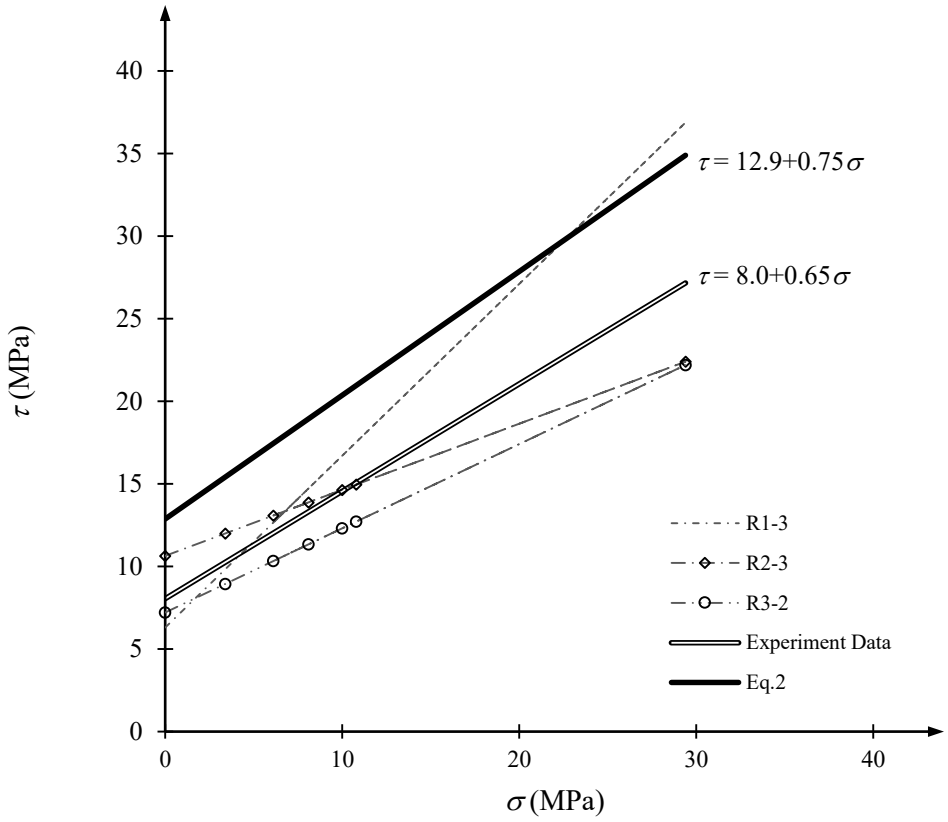

Figure 5.3.10. Comparison of experimental and theoretical equations

5.4 Summery

In this chapter shear strength prediction of concrete member is discussed. In the first part, the experimental test result of beam specimen with spandrels are analyzed. The analytical result is then used to propose a simple Equation for shear strength prediction of a beam having monolithic spandrels. The proposed Equation can predict shear strength capacity of the component with significant accuracy.

In the second part of this chapter, shear strength of concrete beam is experimentally observed to verify Mohr-Coulomb failure criteria for a concrete member experiencing brittle failure. For this purpose, Mohr stress circles are drawn using recorded stress of internal concrete. The Mohr stress circle shows different diameter and shape owing to different axial load ratio. The. Diameter of Mohr stress circle of specimen increase as the axial load ratio increases and vice versa.

The Mohr-Coulomb failure envelopes investigated shows that the angle of fracture of concrete as well as correlation of shear and normal strength are not constant for all of the specimens, but it is proportional to different parameters such as drift angle, concrete compressive strength, failure type, axial load and shear web reinforcement.

Additionally, it is realized that concrete Mohr stress circles resulting from the theoretical analysis can only predict shear strength of a concrete member in the complimentary status rather than critical condition inside the member. The tested specimen in this study realized that the shear strength prediction formula underestimates the shear strength and Mohr-Coulomb modified criteria overestimate the shear strength. Shear is initially resisted by three shear-carrying mechanisms: cantilever action, aggregate interlock, and dowel action. These mechanisms create a state of tensile stresses in the concrete that leads to the development of the critical shear crack.

Chapter VI

Conclusions and Summary

From the experiments and analysis conducted in this research, the following conclusions can be drawn:

The first experimental test included two beam specimens which were comprised from a beam with spandrels (hanging and standing wall) and connected to the wing walls with reduced (half) seismic slit. The specimens were tested under static cycling loading test. The geometry, reinforcements and non-anchorage detailing of both specimens were similar unless the boundary confinement.

The test result showed that the removal (reduction) of seismic slit containing spread of cracks along the beam member and limits damage to the boundary area. Damage and cracking distribution is controlled with formation of a large dominant crack at the spandrel wall boundary during the cyclic loading test; however, the appearance of the large dominant crack did not result in large strength degradation until lateral drift of 1/25.

The capability of both specimens was not affected by the difference in the amount of confinement reinforcement. Because, a large number of transverse reinforcement was placed in the spandrels which inhibited the establishment of critical stress condition around the spandrels and led to counteraction of the confinements.

Another large scale experimental test was conducted to ascertain the effectiveness of the proposed method of detailing of the non-structural wall used in the static loading test. It was aimed to observe the impact of different method of non-structural wall connection on the performance of the building using an artificial earthquake. The specimen was a three story 0.8 scale building and was tested on the E-defense shaking table. It was tested to identify the possibility of continuous use of the buildings in the post-disaster scenario, focusing on the effectiveness of the non-structural wall.

The shaking table test results indicated that beam members with non-structural hanging walls based on the AIJ standard were more vulnerable during artificial earthquakes compared to other structural members. The responses of hanging walls on damage level and strain in a beam under artificial earthquakes using the proposed detailing method was found satisfactory compared to hanging walls with seismic slits.

The analytical result of the tested beam specimens is then used to propose a simple Equation for shear strength prediction of a beam having monolithic spandrels. The proposed Equation can predict shear strength capacity of the component with significant accuracy.

Shear strength observation of the beam members having spandrels are experimentally observed using Mohr-Coulomb criteria. The Mohr-Coulomb failure envelopes investigated shows that the angle of fracture of concrete as well as correlation of shear and normal strength are not constant for all of the specimens, but it is proportional to different parameters such as drift angle, concrete compressive strength, failure type, axial load and shear web reinforcement.

In a coherent experimental study which was the continuity of the former experiments, was aimed to assess the influence of different reinforcement detailing and transverse reinforcement on the strength and drift capacity of the non-structural wall, to develop walls with higher capability. For this purpose, seven specimens which were comprised from a beam with hanging wall and had different specification, were tested.

It was observed that non-anchorage of the wall longitudinal bar significantly increases the drift capacity of the wall and limiting damage. The significant increase of drift capacity of the non-structural wall can be established where:

- There is a non-anchored detailing of longitudinal reinforcement;
- The amount of longitudinal reinforcement is equal or greater than transverse reinforcement;
- The confinements are placed at the critical zone of the wall.

Transverse reinforcement in terms of boundary confinements was more influential when limited to the critical zone. It could better confine the core concrete of the wall and led the specimen to have higher effective compressive stress and strain.

The workability of the confinements and non-anchored detailing was found effective and resulted in the beam member to have higher strength and drift capacity. However; The strength capacity of the anchored detailing specimens with minimum amount of reinforcements was higher than that of the non-anchored specimen.

The slenderness of the non-anchored detailing specimen did not significantly impact the drift capacity despite of having higher quantity of transverse reinforcement it also decreased the strength of hanging wall. The decrease of wall thickness decreased the concrete compression area and damaged establishing expected interaction between concrete, transverse reinforcement and non-anchored detailing.

The impact of boundary confinement on the longitudinal reinforcement under flexural load was higher in the non-anchored case compared to anchored detailing due to different load carrying capacity of the longitudinal reinforcement.

The data of experimental test was observed analytically using Hognasted and Mander models in order to identify accuracy of these models for the beam members. The model proposed by the Hognasted underestimates the drift capacity of the confined concrete after lateral drift of 0.5%. however; the predicted strength capacity of specimens based on the model is nearly complying with the experimental result with a scarce overestimation.

The model proposed by Mander scarcely overestimates the strength capacity of the non-anchored detailing specimen compared to anchored specimens. On the other hand, the impact of type of confining, placement of the longitudinal reinforcement, longitudinal reinforcement detailing and section geometry is not considered in this model while calculating the effective compressive strength.

On the contrary, the ultimate strain, obtained using Mander model, does not correspond to the peak observed strain of experimental results of anchored detailing specimens. However; the average ratio of Cal ε_{cc} / Exp ε_{cc} , for the specimen having non-anchored detailing, is equal to 1.0 which expresses that the strain predicted by the model almost comply with experimental result .

Consequently, the non-anchored detailing of longitudinal reinforcement and existence of the confinement in the boundary of the spandrels resulted in higher compressive strain and strength and accordingly higher capability of the specimen.

Eventually, findings of the researches included in this dissertation suggests construction of the beam members without seismic slit and non-anchorage of the longitudinal bars along with placement of boundary confinement. This model is observed to enhance the seismic capability of beam members using potential capability of the non-structural wall and may grant the building a possibility of continues use during post-disaster scenario.

References

American Concrete Institute; (2014). *Building Code Requirements for Structural Concrete (ACI 318-14) and Commentary (ACI 318R-14)*; American Concrete institute: Farmington Hills, MI, USA.

Aoyama, H., (2001). RC Highrise Building in Seismic Areas. In *Design of modern highrise reinforced concrete structures*; Elnashai, A.S.; Dowling, P.J.; Imperial College Press: London, UK; Vol. 3, pp. 22-25.

Architectural Institute of Japan; (2010a). *AIJ Standard for Structural Calculation of Reinforced Concrete Structures*, Architectural Institute of Japan: Tokyo, Japan. (in Japanese)

Architectural Institute of Japan; (2010b). *Recommendation for detailing placing of concrete reinforcement*. Architectural Institute of Japan: Tokyo, Japan.

Architectural Institute of Japan; (2013). *2011 Great East Japan Earthquake Disaster Survey Report*, Architectural Institute of Japan: Tokyo, Japan.

Architectural Institute of Japan; (2016). *AIJ Standard for Lateral Load-Carrying Capacity Calculation of Reinforced Concrete Structures (Draft)*; Architectural Institute of Japan: Tokyo, Japan.

Architectural Institute of Japan;(1997). *Preliminary Reconnaissance Report of the 1995 Hyogoken-Nanbu Earthquake*; English edition; Architectural Institute of Japan: Tokyo, Japan.

Asian Disaster Reduction Center (ADRC); (2016). *2016 Kumamoto Earthquake Survey Report (Preliminary)*. Asian Disaster Reduction center: Kobe, Japan.

Bentz, E. C.; Vecchio, F. J.; Collins, M. R.;(2006). Simplified Modified Compression Field Theory for Calculating Shear Strength of Reinforced Concrete Elements, *ACI Structural Journal*, **103** (4), 614–624 .

Bentz, E.; Collins, M.P.;(2001). *Response 2000, Version 1.0.5*, University of Toronto: Toronto, Canada.

Building Research Institute and National Institute for Land and Infrastructure Management; (2011). *Summary of the field survey and research on The 2011 off the Pacific coast of Tohoku Earthquake*, Technical Note of National Institute for Land and Infrastructure Management No.647 and BRI research paper No.150. URL: http://www.kenken.go.jp/english/contents/topics/20110311/0311summaryreport.html (accessed on 4th December 2019)

Chang, L.; Ye, X.; Li, K.; (2008). Analysis of seismic energy response and distribution of RC frame structures. *Proceeding of the 14th World Conference on Earthquake engineering: Beijing*, China, Paper ID 0224.

Fuji, K.; Yoshida, S.; Nishimura, T.; Furuta, T.; (2017). Observations of damage to Uto City Hall suffered in the 2016 Kumamoto Earthquake. *In Proceedings of the 8th European Workshop on the Seismic Behavior of Irregular and Complex Structures*: Bucharest, Romania, 17–18; 19–20.

Han, J.; Zhang, Y.; Zheng, N.; Wang, L.; (2008). Analysis on nonlinear seismic response of multi-story torsion-irregular Nstructures. *Proceeding of the 14th World Conference on Earthquake engineering*: Beijing, China, Paper ID 0046.

Hibino, Y., Yamaki, Y. ;(2017). Shear Strength Prediction For Brittle Reinforced Concrete Member Considering Concrete Stress Conditions, *Proceedings of the 16th World Conference on Earthquake*, :Tokyo, Japan, Paper ID 2810.

Hognestad, E.; (1951). A study on combined bending and axial load in reinforced concrete members. Univ. of Illinois Engineering Experiment Station, *Univ. of Illinois at Urbana-Champaign*, IL, 43-46.

Watanabe, F.; (1997). Behavior of Reinforced Concrete Buildings during the Hyougoken-Nanbu Earthquake. *Cement and Concrete Composites*. *19*, 203-211.

Japan Concrete Institute (2005). *A technical report on the structural performance of high-strength concrete structures*; Japan Concrete Institute: Tokyo, Japan. (in Japanese)

Johnson, B; (2010). Anchorage Detailing Effects on Lateral Deformation Components of R/C Shear Walls. M.S. Thesis, University of Minnesota, Department of Civil Engineering, Minneapolis, MN, United States.

Ju, R.S.; Lee, H. J.; Chen, C.C.; (2012). Experimental study on separating reinforced concrete infill walls from steel moment frames. *Journal of Construction Steel Research*, *71*, 119-128.

Kabeyasawa T., Kim Y., Kabeyasawa T., Fukuyama H. *Evaluation on Flexural Deformability of Reinforced Concrete Columns with Wing Walls*. In: Fischinger M. (eds) PerformanceBased Seismic Engineering: Vision for an Earthquake Resilient Society. Geotechnical, Geological and Earthquake Engineering, *32*. Springer, Dordrecht.

Kabeyasawa, T.; Kato, S.; Hosokawa, Y.; (2014). Effect of spandrel and hanging walls on flexural capacity of reinforced concrete columns with wing walls. *Proceeding of the 10th U.S. National conference on earthquake engineering*, Alaska, United State, Paper ID 115.

Kato, H.; Tajiri, S.; Mukai, T.; (2010). Preliminary reconnaissance report of the Chile earthquake 2010. Building Research Institute: Tokyo, Japan.

Lee, H.J.; Ju, R.S.; Chen, Y. L.; (2008). Experimental studies on seismic performance of building frames with infilled RC walls, Architectures and Building Research Institute, Ministry of the Interior: Taiwan, Report No.097301070000G1016.

Maeda, M.; Hamood, A.; Kazuki, S.; Kanako, T.; (2012). Damage of RC Building Structures due to 2011 East Japan Earthquake. *In Proceedings of the structures congress 2012*: Chicago, IL, USA, 29–31; pp. 1023–1034.

Magnusson, J.; Hallgren, M.; Ansell, A.;(2010). Air-Blast-loaded High-Strength Concrete Beams, Part I: Experimental Investigation. *Magazine of Concrete Research 62*, 127–136.

Mander, J.B.; Priestley, M.J.N.; Park, R.; (1984). Theoretical Stress-Strain Model for Confined Concrete. *Journal of Structure Engineering*. 114(3), 1804-1826.

Mochizuki, K.; Obana, K.;(2003). Seismic Activities along the Nankai Trough. *Bulletin of the Earthquake Research Institute. 78*,185-195.

Moehle, J.P.; Acevedo, C.; Creagh, A.; (2010). Exploratory tests of wall boundary elements subjected to alternating tensile and compressive loadings, Poster and oral presentations at 2010 PEER Annual Meeting.

Moehle, J.P.; Wallace, J.W.; (1989). Ductility and detailing requirements of shear wall buildings. *In proceedings of the Fifth Chilean Conference of Seismology and Earthquake Engineering*: Santiago, Chile, pp.131-150.

Muttoni, A.; Ruizr, M. F.; (2008). SheaStrength of Members *without* Transverse Reinforcement as Function of Critical Shear Crack Width. *ACI Structural Journal*, *105* (2), 163-172.

National Institute for Land and Infrastructure Management; (2018). *Design Guidelines for Buildings at disaster bases*, National Institute for Land and Infrastructure Management: Tokyo, Japan (Draft in Japanese). URL:http://www.nilim.go.jp/lab/bcg/siryou/tnn/tnn1004pdf/ks100414.pdf (accessed on 4th March 2020)

Nayuko, U.; Akira, T.; Kusuoki, K.; Sauod, M.; (2015). Experimental study on structural performance and boundary damage condition of RC beam member with spandrel, with seismic slit, *Annual papers of concrete Engineering, 37* (2), pp.223-228. (in Japanese)

Nielsen, M. P.; Braestrup, M. W.; Jensen, B. C.; Bach, F.; (1978). *Concrete Plasticity, Beam Shear–Shear in Joints– Punching Shear*, Special Publication, Danish Society for Structural Science and Engineering.

Ohno, K.; Arakawa, T.; (1960). A study on the shear resistance of reinforced concrete beams, *Architecture institute of Japan, 66*, 10-20 (in Japanese).

Okawa, I.; Satoh, T.; Sato, T.; Tohdo, M.; Kitamura, H.; Torii, S.; Tsuji, Y.; Kitamura, Y.; (2013). Study on long-period ground motions and response of super high-rise building etc. Building Research Institute: Tsukuba, Japan. URL: https://www.kenken.go.jp/japanese/contents/publications/data/144/8_all.pdf

Orakcal, K.; Massone, L.; Wallace, J.; (2009). Shear strength of lightly reinforced wall piers and spandrels, *ACI Structres Journal, 106*(4), 455-465.

Orakcal1, K.; L. Massone, M.; Wallace, J.W.; (2008). Shear strength of lightly reinforced wall piers and spandrels. *Proceeding of the 14th World Conference on Earthquake engineering*: Beijing, China.

Otani, S.; (2004). Japanese seismic design of high-rise reinforced concrete buildings - an example of performance-based design code and state of practices. *Proceeding of the 13th World Conference on Earthquake engineering*: Vancouver, Canada, Paper ID 5010.

Paulay, T. M.; Priestley, M.J. N.; (1992). Seismic design of reinforced concrete and masonry buildings: New York.

Pauley T. M.;(1986a). The Design of Ductile Reinforced Concrete Structural Walls for Earthquake Resistance, *Earthquake Spectra*, *2* (4), pp.783-823.

Popovics, S.; (1973). A Numerical Approach to the Complete Stress - Strain Curve of Concrete. *Cement and Concrete Research*, *3*, 583-599.

Priestley M. J. N.; (2003). *Myths and fallacies in earthquake engineering, revisited*, IUSS Press: Pavia, Italy.

Pujol, S.; Hanai, N.; Ichinose, T., Sozen, M. A.; (2016). Using Mohr-Coulomb Criterion to Estimate Shear Strength of Reinforced Concrete Columns, *ACI Structural Journal*, American Concrete Institute, *113* (3), 459-468.

Richart, F.E.; Brabdzaeg, A.; Brown, R.L.; (1928). A Study of the Failure of Csoncrete Under Combined Compressive Stresses, *Univ. of Illinois Eng. Exp. Station*, Bullitin, No.185.

Saatcioglu, M.; Razvi, S.; (1992). Strength and Ductility of Confined Concrete. *ASCE Journal of Structure Engineering*, Vol.118, pp.1590-1607.

Saito, T.; (2012). Damage of buildings and actions taken during the 2011 great east japan earthquake in the disaster prevention facilities. *In Proceedings of the International Symposium on Engineering Lessons Learned from the 2011 Great East Japan Earthquake*: Tokyo, Japan; pp.1250-1257.

Sato, H.; Yamaguchi, K.; (2000). Stress-strain behavior of square confined concrete column. *In Proceeding of the 12th World Conference on Earthquake engineering*: Lisbon, Portugal, Paper ID 2284.

Segura, C. L.; Wallace, W. J.; (2018). Seismic Performance Limitations and Detailing of Slender Reinforced Concrete Walls. *ACI Structure Journal*, *115*(3), 849-860.

Sheikh, S.A.; Uzumeri, S.M.; (1982). Analytical Model for Concrete Confinement in Tied Columns. *ASCE Journal of Structure Engineering*, Vol.108, pp.925-950.

Shizuoka Prefecture Department of Emergency Management; (2010). *Tokai Earthquake Preparedness in Shizuoka Prefecture*, Shizuoka Prefecture Department of Emergency Management: Shizuoka, Japan. URL:https://www.pref.shizuoka.jp/bousai/equakes/center/guidebook/english/documents/earthquakepreparedness_in_shizuoka2010.pdf (accessed on 10th May 2020)

Sungjin, B.; Oguzhan, B.; (2008). Plastic Hinge Length of Reinforced Concrete Columns. *ACI Structural Journal, 99*(4), pp. 290.

Suzuki, S.; Kuramoto, H.; Matsui, T.; (2013). Restoring force characteristics model of CES shear walls. *Journal of Structural and Construction Engineering (Transactions of AIJ)*, *78*(693), 2027-2034.

Taylor, C. P.; Cote, P. A.; Wallace, J. W., (1998). Design of Slender RC Walls with Openings. *ACI Structural Journal*, *95*, pp. 420-433.

The Building Center of Japan (BCJ); (2016). *The Building Standard Law of Japan on CD-Rom*; The Building Center of Japan: Tokyo, Japan.

Tsubaki, M.; Sanada, Y.; Zhang, Z.; Kusunoki, K.; Hibino, Y.; (2019). Experimental structural performance evaluation of RC columns with wing walls without wall vertical rebar anchorage. *Journal of Structure and Construction Engineering*, *84*, 1881–8153. (in Japanese)

Vecchio, F. J.; Collins, M. P.; (1986). The Modifie Compression-field Theory for Reinforced-concrete Elements Subjected to Shear. *Journal of the AmericanConcrete Institute, 83* (2), 219–231 (1986)

Vecchio, F. J.; Collins, M. P.; (1988). Predicting the response of reinforced-concrete beams subjected to shear using modified compression field-theory. *ACI Structural Journal*, *85* (3),pp. 258–268.

Walid, A.S.; Hibino, Y.; Kusunoki, K.; Tomohisa, M.; Sanada, Y.; Izumi, N.; Trevor, Z.Y.; Satoru, F.; (2020). Structural performance of reinforced concrete members with monolithic non-structural wall under static and dynamic loads. *Journal of Building*, Vol. 10,

Wallace, J.; Orakcal, K.; (2001). ACI 318-99 Provisions for seismic design of structural walls. ACI Struct. J. 2002, 99(4), 499-508.

Wallace, J.W.; (2012). Behavior, design, and modeling of structural walls and coupling beams – lessons from recent lab tests and earthquakes. *International Journal of Concrete Structures & Materials*, 6(1), pp. 3-18.

Welt, T. S.; (2015). Detailing for Compression in Reinforced Concrete Wall Boundary elements: Experiments, Simulations, and Design Recommendations. Ph.D. Thesis, University of Illinois, Urbanna Champaign, IL, USA.

Yanagisawa, M; (2008). An experimental study on structural performance of R/C frame with non-structural slit wall: part 2 discussion of test results, *Summaries of Technical Papers of Annual Meeting of Architectural Institute of Japan*, Tokyo, Japan, C-2, Structures IV, 393-394. (in Japanese)

Yoon, R.; Sanada, Y.; Akahaori, T.; (2017). Seismic performance evaluation of RC moment-resisting frames with typical non-structural walls in japan. *Journal of Advanced Concrete and Technology*, *15*, 544–557.

Zhang, T.; Visintin, P.; Oehlers, D. J.; (2016). Shear strength of RC beams without web Reinforcement, *Australian Journal of Structural Engineering*, *17* (1), 87-96.

ANEX A

Table A-1 Data of compression tests

Test Type: Cylinder compression test Specimen ID: BS Cylinder ID: C-1					
SG[1]-1	SG-2	SG-3	SG-4	Compressive stress	Average strain
0.00	0.96	0.00	0.00	0.00	0.24
0.96	0.96	0.96	0.00	-0.06	0.72
37.50	20.19	33.65	27.88	0.81	29.81
46.15	26.92	42.31	37.50	1.06	38.22
84.62	68.27	84.62	77.88	2.18	78.85
92.31	77.88	92.31	85.58	2.43	87.02
86.54	72.12	86.54	80.77	2.12	81.49
84.62	70.19	84.62	78.85	2.12	79.57
116.35	103.85	119.23	116.35	3.12	113.94
150.96	142.31	154.81	156.73	4.12	151.20
189.42	184.62	195.19	202.89	5.18	193.03
227.89	225.00	234.62	248.08	6.18	233.89
263.46	264.42	272.12	290.39	7.18	272.60
297.12	300.00	305.77	327.89	8.05	307.69
344.23	348.08	353.85	381.73	9.24	356.97
385.58	387.50	396.15	426.92	10.24	399.04
426.92	421.15	438.46	466.35	11.17	438.22
475.96	457.69	487.50	510.58	12.17	482.93
525.96	498.08	536.54	557.69	13.23	529.57
573.08	538.46	585.58	604.81	14.23	575.48
620.19	582.69	633.65	652.89	15.29	622.36
667.31	625.00	682.69	700.00	16.23	668.75
715.39	669.23	732.69	750.96	17.23	717.07
765.39	714.42	786.54	802.89	18.23	767.31
816.35	759.62	839.42	854.81	19.23	817.55
872.12	809.62	898.08	908.65	20.22	872.12
934.62	865.39	962.50	971.15	21.29	933.41
994.23	915.39	1025.00	1029.81	22.22	991.11
1065.38	974.04	1098.08	1097.12	23.28	1058.65
1135.58	1027.88	1167.31	1159.62	24.22	1122.60
1221.15	1091.35	1251.92	1232.69	25.16	1199.28
1328.85	1161.54	1351.92	1314.42	26.28	1289.18
1439.42	1228.85	1455.77	1392.31	27.28	1379.09
1581.73	1301.92	1587.50	1482.69	28.21	1488.46
1787.50	1382.69	1775.96	1590.38	29.15	1634.13
2062.50	1440.38	2028.85	1679.81	29.71	1802.89
2361.54	1433.65	2267.31	1725.00	29.84	1946.88
2657.69	1311.54	2368.27	1725.96	29.15	2015.87
-678.85	-26.92	1260.58	796.15	8.99	337.74
-728.85	-37.50	1236.54	777.89	8.74	312.02
-699.04	-43.27	1213.46	770.19	8.68	310.34
-661.54	-50.00	1188.46	768.27	8.55	311.30
-292.31	-31.73	501.92	625.00	0.06	200.72
-299.04	-6.73	483.65	622.12	0.00	200.00

[1] Strain gauge

Table A-2 Data of compression tests

Test Type: Cylinder compression test Specimen ID: BS Cylinder ID: C-2					
SG-1	SG-2	SG-3	SG-4	Compressive stress	Average strain
0.96	0.00	0.00	-0.96	0.00	0.00
0.00	0.00	0.00	0.00	0.00	0.00
34.62	43.27	42.31	31.73	1.12	37.98
71.15	79.81	83.65	66.35	2.18	75.24
108.65	116.35	125.00	99.04	3.31	112.26
146.15	153.85	165.39	132.69	4.37	149.52
177.89	185.58	200.96	159.62	5.24	181.01
221.15	229.81	248.08	199.04	6.43	224.52
259.62	269.23	291.35	234.62	7.49	263.70
293.27	304.81	329.81	265.39	8.43	298.32
334.62	349.04	376.92	303.85	9.55	341.11
371.15	385.58	417.31	336.54	10.55	377.64
400.96	418.27	451.92	363.46	11.36	408.65
441.35	460.58	497.12	400.96	12.36	450.00
485.58	503.85	544.23	439.42	13.42	493.27
527.89	550.00	593.27	478.85	14.54	537.50
566.35	590.39	638.46	515.39	15.48	577.64
607.69	631.73	682.69	550.00	16.42	618.03
649.04	674.04	728.85	587.50	17.35	659.86
702.89	727.89	787.50	633.65	18.54	712.98
740.39	763.46	825.96	665.39	19.29	748.80
797.12	817.31	886.54	712.50	20.41	803.37
848.08	866.35	940.39	753.85	21.35	852.16
905.77	916.35	1000.96	797.12	22.28	905.05
968.27	975.00	1067.31	844.23	23.28	963.70
1034.62	1031.73	1135.58	892.31	24.28	1023.56
1110.58	1091.35	1213.46	941.35	25.22	1089.18
1120.19	1099.04	1224.04	947.12	25.34	1097.60
1202.88	1159.62	1307.69	996.15	26.28	1166.59
1296.15	1222.12	1414.42	1033.65	27.22	1241.59
1340.38	1250.00	1463.46	1053.85	27.59	1276.92
1425.96	1300.00	1561.54	1087.50	28.21	1343.75
1469.23	1323.08	1612.50	1102.88	28.53	1376.92
1594.23	1382.69	1765.38	1137.50	29.21	1469.95
1666.35	1411.54	1858.65	1152.88	29.52	1522.36
1750.96	1442.31	1974.04	1164.42	29.84	1582.93
1880.77	1474.04	2148.08	1169.23	30.09	1668.03
2062.50	1501.92	2412.50	1148.08	30.21	1781.25
2291.35	1524.04	2546.15	1087.50	30.09	1862.26
3180.77	1496.15	2172.12	520.19	27.96	1842.31
1287.50	884.62	1764.42	-40.38	10.99	974.04
1213.46	871.15	1712.50	-48.08	10.80	937.26
1108.65	865.39	1618.27	-54.81	10.86	884.37
887.50	280.77	1069.23	-34.62	0.12	550.72

Table A-3 Data of compression tests

Test Type: Cylinder compression test Specimen ID: BS Cylinder ID: C-3					
SG-1	SG-2	SG-3	SG-4	Compressive stress	Average strain
0	0	0	0	0	0
-0.96	0.00	0.96	0.96	0.00	0.24
53.85	40.38	55.77	54.81	1.50	51.20
82.69	67.31	85.58	81.73	2.31	79.33
119.23	102.89	125.00	121.15	3.37	117.07
153.85	136.54	161.54	159.62	4.37	152.88
190.39	172.12	198.08	200.96	5.37	190.38
229.81	213.46	241.35	247.12	6.49	232.93
265.39	249.04	277.89	286.54	7.43	269.71
303.85	290.39	319.23	331.73	8.49	311.30
339.42	327.89	358.65	372.12	9.49	349.52
378.85	368.27	400.96	417.31	10.55	391.35
419.23	410.58	444.23	465.39	11.61	434.86
453.85	447.12	482.69	506.73	12.48	472.60
497.12	492.31	529.81	558.65	13.61	519.47
537.50	534.62	572.12	607.69	14.61	562.98
575.00	572.12	610.58	650.96	15.48	602.16
615.39	614.42	655.77	700.00	16.48	646.39
661.54	661.54	705.77	755.77	17.48	696.15
706.73	707.69	755.77	811.54	18.54	745.43
746.15	747.12	799.04	859.62	19.35	787.98
800.00	800.00	856.73	925.00	20.41	845.43
846.15	845.19	908.65	980.77	21.29	895.19
900.96	900.00	973.08	1049.04	22.35	955.77
962.50	955.77	1044.23	1124.04	23.41	1021.63
1050.00	998.08	1151.92	1189.42	24.34	1097.35
1120.19	1050.00	1237.50	1260.58	25.28	1167.07
1205.77	1113.46	1351.92	1352.88	26.34	1256.01
1275.96	1161.54	1455.77	1428.85	27.09	1330.53
1290.38	1172.12	1480.77	1445.19	27.22	1347.12
1346.15	1206.73	1581.73	1501.92	27.71	1409.13
1413.46	1246.15	1733.65	1564.42	28.21	1489.42
1462.50	1269.23	1860.58	1598.08	28.46	1547.60
1531.73	1297.12	2079.81	1625.96	28.65	1633.66
1554.81	1304.81	2174.04	1625.96	28.65	1664.91
1575.00	1311.54	2274.04	1619.23	28.59	1694.95

Table A-4 Data of compression tests

Test Type: Cylinder compression test
Specimen ID: BSH
Cylinder ID: C-1

SG-1	SG-2	SG-3	SG-4	Compressive stress	Average strain
0.00	0.00	0.00	-0.96	0.00	-0.24
5.77	1.92	2.88	0.96	0.00	2.88
3.85	0.00	1.92	0.00	0.00	1.44
65.38	36.54	52.88	33.65	1.19	47.12
114.42	80.77	101.92	73.08	2.43	92.55
152.89	115.39	140.39	105.77	3.37	128.61
185.58	143.27	170.19	132.69	4.12	157.93
233.65	183.65	216.35	173.08	5.18	201.68
281.73	225.00	263.46	213.46	6.18	245.91
327.89	262.50	307.69	251.92	7.18	287.50
375.96	302.89	352.89	294.23	8.18	331.49
447.12	364.42	421.15	355.77	9.18	397.12
489.42	402.89	462.50	393.27	10.24	437.02
534.62	440.39	505.77	430.77	11.30	477.88
583.65	481.73	551.92	472.12	12.30	522.36
633.65	523.08	598.08	513.46	13.23	567.07
689.42	569.23	650.96	559.62	14.29	617.31
745.19	616.35	702.89	605.77	15.36	667.55
801.92	662.50	755.77	650.96	16.35	717.79
863.46	713.46	813.46	700.96	17.35	772.84
920.19	759.62	864.42	745.19	18.29	822.36
984.62	810.58	923.08	795.19	19.29	878.37
1054.81	866.35	986.54	850.00	20.35	939.42
1129.81	923.08	1051.92	904.81	21.35	1002.40
1207.69	982.69	1121.15	961.54	22.28	1068.27
1291.35	1044.23	1193.27	1018.27	23.28	1136.78
1392.31	1113.46	1278.85	1083.65	24.28	1217.07
1499.04	1184.62	1371.15	1150.00	25.22	1301.20
1635.58	1269.23	1487.50	1228.85	26.28	1405.29
1768.27	1348.08	1605.77	1300.96	27.22	1505.77
1950.96	1446.15	1775.96	1384.62	28.15	1639.42
2286.54	1580.77	2088.46	1475.96	29.09	1857.93
880.77	996.15	2004.81	733.65	13.86	1153.85
858.65	1000.00	2005.77	736.54	13.92	1150.24
671.15	295.19	756.73	162.50	0.06	471.39
661.54	281.73	712.50	156.73	0.00	453.13

Table A-5 Data of compression tests

Test Type: Cylinder compression test Specimen ID: BSH Cylinder ID: C-2					
SG-1	SG-2	SG-3	SG-4	Compressive stress	Average strain
-0.96	-0.96	0.00	0.00	0.00	-0.48
-2.88	-2.88	-0.96	0.00	0.00	-1.68
38.46	41.35	49.04	40.38	1.19	42.31
76.92	84.62	94.23	80.77	2.31	84.13
118.27	125.00	138.46	119.23	3.37	125.24
155.77	162.50	177.89	156.73	4.31	163.22
199.04	209.62	225.96	202.89	5.43	209.38
242.31	256.73	273.08	247.12	6.55	254.81
280.77	298.08	313.46	288.46	7.49	295.19
318.27	339.42	357.69	328.85	8.43	336.06
360.58	387.50	404.81	374.04	9.43	381.73
404.81	436.54	454.81	421.15	10.55	429.33
447.12	484.62	501.92	467.31	11.49	475.24
488.46	529.81	548.08	512.50	12.42	519.71
539.42	587.50	605.77	567.31	13.55	575.00
586.54	639.42	658.65	618.27	14.54	625.72
632.69	692.31	710.58	669.23	15.54	676.20
682.69	749.04	768.27	724.04	16.54	731.01
733.65	804.81	826.92	777.89	17.48	785.82
786.54	864.42	886.54	834.62	18.48	843.03
843.27	928.85	952.89	895.19	19.48	905.05
903.85	996.15	1023.08	959.62	20.47	970.67
965.39	1064.42	1096.15	1024.04	21.41	1037.50
1044.23	1152.88	1193.27	1106.73	22.53	1124.28
1098.08	1212.50	1260.58	1163.46	23.22	1183.66
1202.88	1324.04	1387.50	1268.27	24.41	1295.67
1302.88	1433.65	1511.54	1371.15	25.41	1404.81
1428.85	1573.08	1672.12	1496.15	26.47	1542.55
1561.54	1726.92	1857.69	1629.81	27.28	1693.99
771.15	679.81	1440.38	430.77	7.55	830.53
712.50	646.15	1386.54	324.04	6.74	767.31

Table A-6 Data of compression tests

Test Type: Cylinder compression test
Specimen ID: BSH
Cylinder ID: C-3

SG-1	SG-2	SG-3	SG-4	Compressive stress	Average strain
-0.96	0.00	0.00	0.00	0.00	-0.24
-0.96	0.96	0.00	0.00	0.00	0.00
75.96	76.92	87.50	68.27	2.06	77.16
106.73	106.73	119.23	94.23	2.93	106.73
128.85	129.81	145.19	116.35	3.50	130.05
168.27	171.15	187.50	153.85	4.49	170.19
206.73	212.50	229.81	192.31	5.43	210.34
251.92	260.58	278.85	237.50	6.62	257.21
283.65	293.27	313.46	267.31	7.37	289.42
328.85	340.39	362.50	311.54	8.43	335.82
374.04	387.50	411.54	355.77	9.43	382.21
420.19	437.50	464.42	401.92	10.61	431.01
463.46	482.69	511.54	444.23	11.49	475.48
509.62	530.77	562.50	489.42	12.48	523.08
557.69	580.77	615.39	534.62	13.48	572.12
608.65	633.65	671.15	584.62	14.61	624.52
658.65	686.54	728.85	632.69	15.54	676.68
711.54	740.39	787.50	681.73	16.54	730.29
767.31	800.00	851.92	735.58	17.54	788.70
824.04	859.62	919.23	790.39	18.60	848.32
884.62	924.04	990.39	848.08	19.60	911.78
945.19	988.46	1064.42	904.81	20.54	975.72
1004.81	1050.96	1136.54	959.62	21.35	1037.98
1077.88	1128.85	1229.81	1025.96	22.28	1115.63
1160.58	1221.15	1341.35	1102.88	23.35	1206.49
1251.92	1322.12	1465.38	1185.58	24.34	1306.25
1348.08	1434.62	1606.73	1270.19	25.28	1414.91
1477.88	1600.00	1835.58	1382.69	26.28	1574.04
1611.54	1794.23	2155.77	1489.42	27.22	1762.74
743.27	1438.46		629.81	5.56	937.18